

NANOSCALE HEAT TRANSFER EFFECTS IN THE COMBUSTION OF NANOENERGETIC MATERIALS

A Dissertation
Presented to
The Academic Faculty

by

Murali Gopal Muraleedharan

In Partial Fulfillment
of the Requirements for the Degree
Doctor of Philosophy in the
School of Aerospace Engineering

Georgia Institute of Technology
December 2018

COPYRIGHT © 2018 BY MURALI GOPAL MURALEEDHARAN

NANOSCALE HEAT TRANSFER EFFECTS IN THE COMBUSTION OF NANOENERGETIC MATERIALS

Approved by:

Dr. Vigor Yang, Advisor
School of Aerospace Engineering
Georgia Institute of Technology

Dr. Asegun Henry
Department of Mechanical Engineering
Massachusetts Institute of Technology

Dr. G. P. Peterson
George W. Woodruff School of
Mechanical Engineering
Georgia Institute of Technology

Dr. Jerry M. Seitzman
School of Aerospace Engineering
Georgia Institute of Technology

Dr. Julian Rimoli
School of Aerospace Engineering
Georgia Institute of Technology

Date Approved: [October 2, 2018]

To my parents

ACKNOWLEDGEMENTS

“In an era of instant gratification, we settle for short trees, but patience has its reward.”

- *Rahul Dravid, former Indian cricket team captain*

I thank God Almighty for giving me the strength to find opportunities in adversities.

This has been a long, arduous, and intellectually stimulating journey for me, and it would not have been possible without the guidance and support of many people. First and foremost, I thank my advisers Prof. Vigor Yang and Prof. Asegun Henry. It has been a privilege working with them. I thank Prof. Yang for accepting me to his group in 2013, for his constant support and guidance, and for teaching me the importance of humility and work ethic in achieving success. I cannot find words to express my gratitude to Prof. Henry. His immense knowledge, vision, and charisma have been instrumental in crafting a holistic outlook to research, and life in general. I express my gratitude to Sharath Nagaraja and Aravindh Rajan for showing me the path to Prof. Yang’s and Prof. Henry’s groups respectively. I also thank Prof. G. P. Peterson, Prof. Jerry Seitzman, and Prof. Julian Rimoli for serving in my thesis committee. I also give thanks to Air Force Office of Scientific Research (AFOSR) for the sponsorship of this program under Contract No. FA9550-13-1-0004. The support and encouragement provided by Dr. Mitat Birkan is greatly appreciated.

I am grateful to Kiarash Gordiz, Kiran Sasikumar, Andrew Rohskopf, Freddy DeAngelis, and Shenghong Ju for the technical support and discussion. I am deeply indebted to Suo Yang and Chris Lioi for teaming up with me in preparing for the Ph.D. qualifying exam; I am humbled by their knowledge and inquisitiveness. No words can

express my gratitude to the selfless service of Prof. Jeff Jagoda and Oksana Gomas in graduate studies administration. Graduate studies at Georgia Tech would not have been the same without their service.

I wish to extend my gratitude to my lab mates: Umesh, Xingjian, Yixing, Dilip, Prashant, Liwei, Shiang, Yu-Hung, Tim, and Yanxing for tolerating me and being my friend throughout my stay at Georgia Tech. Thanks to all my close buddies in Atlanta, especially those who belong to the WhatsApp group: *Gangs of Atlanta'pur* for their unwavering moral support.

Last but not the least, I thank my parents, sister, brother, and nephew for their endless love, care, and support, which have been a constant driving force throughout my life. I dedicate this Ph.D. thesis to them.

TABLE OF CONTENTS

ACKNOWLEDGEMENTS	iv
LIST OF TABLES	ix
LIST OF FIGURES	x
LIST OF SYMBOLS AND ABBREVIATIONS	xiii
SUMMARY	xvii
CHAPTER 1. Introduction	1
1.1 Nanoenergetic materials	1
1.2 Mechanism of ignition and combustion of nano-aluminum: Phenomenological understanding	4
1.3 Flame propagation in nAl mixtures: Experimental studies and theoretical modeling	9
1.4 Thermal conductivity of nano-suspensions	15
1.4.1 Size-dependent thermal conductivity of nanoparticles and the oxide layer	17
1.4.2 Thermal interfacial conductance and resistance (TIC, TIR)	19
1.4.3 Dynamic heat conduction mechanisms	22
1.5 Research objectives	25
1.6 Dissertation outline	26
CHAPTER 2. Theoretical formulation	28
2.1 Introduction	28
2.2 Density functional theory	31
2.2.1 Wavefunctions and Schroedinger's equation	31
2.3 Molecular dynamics (MD)	35
2.3.1 Potential functions	36
2.3.2 Time integration	42
2.3.3 Fluctuation dissipation theorem: Green-Kubo relations	44
2.4 Lattice Dynamics (LD)	46
2.4.1 Calculation of interatomic force constants and phonon properties	48
2.4.2 Group velocity of phonons	50
2.4.3 Phonon density of states (DOS)	51
2.4.4 Phonon thermal conductivity	52
2.5 Interfacial Conductance Modal Analysis (ICMA)	55
2.5.1 Total conductance	55
2.5.2 Modal decomposition	57
2.6 Effective thermal conductivity model of heterogeneous propellant	59
2.7 1-Dimensional flame propagation model	61
2.7.1 Physical system	61
2.8 Conclusions	64

CHAPTER 3. Phonon transport in aluminum and aluminum oxide	65
3.1 Introduction	65
3.2 Methodology	67
3.3 Results	68
3.3.1 Phonon dispersion relations	68
3.3.2 Phonon density of states	69
3.3.3 Phonon thermal conductivity	70
3.3.4 Phonon thermal conductivity accumulation function	72
3.3.5 Spectral thermal conductivity distribution	74
3.3.6 Phonon mean free paths and lifetimes	75
3.4 Conclusions	76
CHAPTER 4. Thermal conductance of aluminum-aluminum oxide interface	78
4.1 Introduction	78
4.2 Simulation details	85
4.2.1 Interfacial Conductance Modal Analysis (ICMA)	85
4.2.2 Atomistic Green Function (AGF)	87
4.3 Results	87
4.3.1 Total conductance, G	87
4.3.2 Modal Analysis	90
4.4 Conclusions	94
CHAPTER 5. Interfacial nanolayer and brownian motion: the issue of artificial correlations	96
5.1 Introduction	96
5.2 Methodology	99
5.3 Results and Discussion	101
5.3.1 Thermal conductivity of water	101
5.3.2 Thermal conductivity of nano-suspensions	102
5.3.3 Artificial correlations	105
5.4 Conclusions	110
CHAPTER 6. Numerical modeling of flame propagation in nano-aluminum-water mixtures	112
6.1 Introduction	113
6.2 One-dimensional flame model and numerical framework	116
6.2.1 Energy balance for liquid water- solid aluminum (Zone A)	118
6.2.2 Energy balance for water vapor- solid aluminum (Zone B)	120
6.2.3 Energy balance for water vapor- molten aluminum (Zone C)	121
6.2.4 Energy balance for reaction zone (Zone D)	122
6.3 Results	124
6.3.1 Thermal transport	124
6.3.2 Flame propagation	128
6.4 Conclusions	132
CHAPTER 7. Conclusions and future directions	134
7.1 Conclusions	134

7.2	Recommendations for future work	138
	Appendix A. Free parameters of empirical potential functions	140
	Appendix B. Comparison of phonon properties calculated from LD calculation using Streitz-Mintmire (SM) potential and DFT	142
	References	144

LIST OF TABLES

Table 4.1	Contribution of different types of modes to partial DOS and G, and the percentage relative contribution of G to DOS	93
Table 6.1	Some prospective Al oxidation chemistries and equilibrium products	113
Table 6.2	Constants in eq. 6.16	123
Table 6.3	Summary of results obtained from a numerical solution of flame structure and burning properties for the baseline case ($P = 1$ bar; $D_p = 38$ nm), compared with experimental results and a prior theoretical model	129
Table A.1	Interatomic potential parameters for Vashishta potential for Al_2O_3	132
Table A.2	Interatomic potential parameters for Streitz-Mintmire potential for Al and Al_2O_3	133

LIST OF FIGURES

Figure 1.1	Comparison of volumetric and gravimetric enthalpy of oxidation (energy content) of metals and widely used monomolecular energetic materials	2
Figure 1.2	Burning time of Al particles as a function of mean particle diameter obtained from experimental results	5
Figure 1.3	Particle size regimes where kinetic and diffusion controlled combustion are observed in experimental studies	6
Figure 1.4	Energy balance where the control volume represents an aluminum nanoparticle suspended in an oxidizer medium	6
Figure 1.5	(a) Linear burning rate of Al composite as a function of specific surface area (SSA) and (b) Flame speed in Al-air mixture as a function of particle diameter	8
Figure 1.6	Comparison of nAl burning times predicted by Eq. 6.1 and experimental burning times for a range of temperatures representative of the reaction zone of a flame	11
Figure 1.7	Comparison of linear burning rates predicted by the model with experimental values as a function of chamber pressure for a) 38 nm, b) 80 nm, and c) 138 nm particle suspensions	12
Figure 1.8	Comparison of linear burning rates as a function of nanoparticle volume fraction predicted by using different effective thermal conductivity models with experimental data	13
Figure 1.9	Schematic diagram showing nAl particles coated by an oxide layer dispersed in water. Temperature profile shows initial (T_i) and final (T_f) temperatures. Nanoparticles move around within the system in random directions, as shown by the arrows.	15
Figure 1.10	Dependence of thermal conductivity on the particle size and carrier mean free path as described by Chen et al. showing ballistic, quasi-diffusive, and diffusive regimes of heat conduction	18
Figure 1.11	Series circuit framework for evaluating thermal conductivity of nanoparticle	19
Figure 1.12	Thermal conductivity enhancement of a nanoparticle suspension as a function of particle size for various interfacial conductance values	21
Figure 2.1	(a) Vertically downward flame propagation in a mixture of nAl and water showing the temperature profile within the system, and (b) Schematic of constant-pressure strand burner	29
Figure 2.2	One-dimensional bead-spring chain representing atomic arrangement in a crystal	47
Figure 2.3	Schematic diagram of the core-shell particle model for evaluating the effective thermal conductivity of a nanoparticle	59
Figure 2.4	Physical model and multi-zone theoretical framework	62

Figure 3.1	Phonon dispersion relations of a) Al and b) Al ₂ O ₃ evaluated via DFT-LD method compared with experimental results suggesting that the phonons are captured reasonably well by the DFT-LD framework	68
Figure 3.2	Phonon density of states (DOS) of a) Al and b) Al ₂ O ₃ evaluated via DFT-LD method compared with experimental results giving further validation to the fact that the phonons are captured reasonably well by the DFT-LD framework	70
Figure 3.3	Phonon thermal conductivity (TC) of a) Al and b) Al ₂ O ₃ evaluated via DFT-LD method compared with prior DFT calculations and experimental results	71
Figure 3.4	Phonon thermal conductivity accumulation plots of a) Al and b) Al ₂ O ₃	73
Figure 3.5	Spectral distribution of phonon TC of a) Al and b) Al ₂ O ₃	74
Figure 3.6	Spectral distribution of phonon lifetime and mean free paths of a) aluminum and b) aluminum oxide	75
Figure 4.1	Comparison of theoretical predictions of thermal interfacial conductance, G across different interfaces with corresponding experimentally measured values.	81
Figure 4.2	a) Thermal interfacial conductance predicted by ICMA and AGF methods compared with experimental results and diffused-mismatch model (DMM) prediction, and b) thermal interfacial conductance predicted by ICMA from $T = 300$ - 1800 K	83
Figure 4.3	a) Partial DOS showing different types of modes, b) TIC accumulation (In this system, >90% of the total conductance is contributed by partially extended modes on Al and Al ₂ O ₃ , and the extended modes below 12 THz, and c) mode-mode correlation map at $T = 300$ K showing three distinguishable regions	88
Figure 5.1	Thermal conductivity of water as a function of temperature evaluated by MD simulations using different potential functions, compared with experimental results	102
Figure 5.2	(a). Cross-section of single nanoparticle simulation system, and (b) radial density profile for 1 nm particle suspension at $\phi \sim 1\%$	103
Figure 5.3	Enhancement in effective thermal conductivity (TC) as a function of particle volume fraction compared with various thermal conductivity models	104
Figure 5.4	Enhancement in effective thermal conductivity (TC) calculated from single particle simulations as a function of particle thermal conductivity for various volume fractions	105
Figure 5.5	Thermal conductivity of alumina nanoparticle as a function of particle size	106
Figure 5.6	Comparison of the vibrational spectra of water and alumina	107
Figure 5.7	Time decay of heat current autocorrelation function 1 nm particle, $\phi = 10\%$; <i>Inset</i> : multi-particle simulation system	108

Figure 5.8	Enhancement in effective thermal conductivity (TC) calculated from multi-particle simulations as a function of particle volume fraction compared with (a) Maxwell model with bulk thermal conductivity of alumina and experimental results[1, 2] (b) Maxwell model with thermal conductivity of alumina particles from Fig. 5.5	109
Figure 6.1	Theoretical multizone framework used to represent reaction and preheat zones. Zone A-C represent preheat zones and zone D represents the reaction zone	116
Figure 6.2	(a) Thermal resistance of Al, Al ₂ O ₃ , and interface (b) Percentage contribution by each resistance component to the total thermal resistance of the nanoparticle	125
Figure 6.3.	(a) Thermal conductivity of nanoparticles of diameters $D_p = 38$ nm, 80 nm, and 138 nm, and (b) Effective thermal conductivity of nAl-H ₂ O mixture for different particle sizes, as a function of temperature	127
Figure 6.4	Detailed flame structure obtained via numerical solution of the 1D flame propagation problem clearly showing the different zones and their thicknesses	129
Figure 6.5	Linear burning rate as a function of particle diameter, illustrating how increasing levels of complexity in modeling particle thermal conductivity give better prediction of particle size dependent burning rates	130
Figure 6.6	Sensitivity of linear burning rate to changes in thermal conductivity of a) Al and b) Al ₂ O ₃ , and c) thermal interfacial conductance, G for three different particle sizes	131
Figure B.1	Comparison of phonon DOS evaluated using SM potential and DFT for a) Al and b) Al ₂ O ₃	142
Figure B.2	Comparison of dispersion relations evaluated using SM potential and DFT for a) Al and b) Al ₂ O ₃	143
Figure B.3	Comparison of phonon thermal conductivity evaluated using SM potential and DFT for a) Al and b) Al ₂ O ₃	143

LIST OF SYMBOLS AND ABBREVIATIONS

a	Acceleration
A	Area
d	Particle diameter
C_p	Specific heat at constant pressure
C_v	Specific heat at constant volume
D	Particle diameter
$D(\mathbf{k})$	Dynamic matrix
$\mathbf{e}_{n,i}$	Eigen vector
exp	Exponential
E	Energy
f	Probability density function, force on atom
F	Force
G	Thermal interfacial conductance
h	Planck's constant
H	Hamiltonian
\hat{H}	Hamiltonian operator
i	Imaginary unit
k	Thermal conductivity
k_B	Boltzmann constant
K	Spring constant in bead-spring model
L	Characteristic dimension, length

m	Mass
N_a	Avogadro number
p	Momentum
q	Heat, charges when used with subscripts
Q	Heat flux
$Q_{A \rightarrow B}$	Heat flux from A to B
Q_n	Modal heat flux
\dot{Q}	Heat flux per unit time
r	Spatial coordinate, position vector
r_b	Burning rate
S	Heat current in Green-Kubo relations
t_b	Burning time
t	Time
T	Temperature, kinetic energy when used with subscripts
U	Potential energy
u_n	Atomic displacement in bead-spring model
v	velocity
V	Potential energy function
\mathbf{x}_i	Displacement vector
$\dot{\mathbf{x}}_i$	Velocity vector
X_n	Normal mode decomposition of displacement vector
\dot{X}_n	Normal mode decomposition of velocity vector

Z Charges

Greek symbols

Γ Phonon line width

δ Zone thickness

Λ Mean free path

ε Depth of potential energy well

θ Correction term in three-body interactions

ϕ Particle volume fraction

Φ Correction term in three-body interactions

ρ Electron density

σ Atomic diameter

τ Reaction timescale

τ_b Mean particle burning timescale

Ψ Wave function

ω Angular frequency

Subscripts

$A-D$ Zones A to D in flame model

$conv$ Convectioal

eff Effective

f Fluid

i, j Atom id's

<i>ign</i>	Ignition
<i>in</i>	Inwards
<i>int</i>	Interface
<i>LJ</i>	Lennard-Jones
<i>loss</i>	Loss
<i>m</i>	Mixture
<i>out</i>	Outwards
<i>p</i>	Particle
<i>ph</i>	Phonon
<i>rad</i>	<i>Radiative</i>
<i>rxn</i>	Reaction
<i>xc</i>	Exchange-Correlation
-	Towards left-side
+	Towards righ-side

Superscripts

<i>acc</i>	Accumulation
<i>anh</i>	Anharmonic
<i>DFT</i>	Density Functional Theory
<i>LD</i>	Lattice Dynamics
<i>LDA</i>	Local Density Approximation
<i>iso</i>	Isotropic

SUMMARY

Metal-based composite energetic materials have substantially higher volumetric energy density when compared with monomolecular compounds such as trinitrotoluene (TNT). Micron-sized metal particles have been routinely used for energetic applications since the 1950's. They, however, suffer from several drawbacks such as high ignition temperatures, agglomeration, and low reaction rates, resulting in low energy release rates. Nanoparticles exhibit beneficial physicochemical properties compared to their micron-scale counterparts for combustion applications. Due to the large specific surface area (SSA), they also offer tailorable surface properties that have the potential to allow precision control of thermal transport and chemical kinetics. Hence, during the mid-1990's, widespread replacement of microparticles with nanoparticles created a new class of energetic materials called nanoenergetic materials.

Among the different candidate metals, aluminum is desired because of its abundance, high oxidation enthalpy, low cost of extraction, and for its relatively safe combustion products. This study provides a perspective to combustion wave propagation in nano-energetic materials that accounts for nanoscale heat conduction effects. Here we use the nano-aluminum – water system as an example system. A fundamental treatment of heat transport in nanoparticles and interfaces is carried out. Firstly, *ab initio* and atomistic scale simulations were performed to investigate the nanoscopic nature of heat transport in bulk and nanosized aluminum and aluminum oxide, as well as at the interface of these materials. Atomistically informed macroscale modeling techniques were then employed to

treat heat transport in mixtures of nanoparticles in liquid oxidizer to study combustion wave propagation. The key findings of this research are summarized herein.

Before delving into investigating the nuances, a simple analysis was performed on the factors contributing towards thermal conductivity. The analysis showed that size effects could be important and also that the thermal interfacial resistance (TIR) could be the limiting resistance. Therefore, as the first step, a detailed analysis of phonon transport properties in aluminum (Al) and aluminum oxide (Al_2O_3) has been performed via lattice dynamics (LD) using input from density functional theory (DFT) calculations. DFT-LD methods reproduce the transverse and longitudinal phonon branches in Al and Al_2O_3 along the edges of Brillouin zone accurately. Furthermore, temperature dependent phonon thermal conductivity (TC) of Al and Al_2O_3 are also evaluated by solving the Boltzmann transport equation (BTE) under the relaxation time approximation (RTA), and the thermal conductivity accumulation functions were also evaluated. This analysis gave insights on what phonon mean free paths were affected by the system size. Spectral distribution of TC was also analyzed to assess the possibility of engineering phonon transport properties. These studies provide a fundamental understanding of phonon frequencies and their contribution in pristine bulk Al and Al_2O_3 crystals.

Building on the understanding of thermal transport in bulk Al and Al_2O_3 , the study was extended to understand heat transport across Al/ Al_2O_3 interfaces. The thermal interfacial conductance (G) of the aluminum (Al)-aluminum oxide ($\alpha\text{-Al}_2\text{O}_3$) interface along the crystal directions (111) Al || (0001) Al_2O_3 was accurately predicted. Two fundamentally different formalisms were used to make these predictions in the temperature range 50-1800 K: interfacial conductance modal analysis (ICMA) and the atomistic green

function (AGF) method. ICMA formalism is based on the fluctuation-dissipation theorem whereas AGF is based on phonon gas model (PGM). The study reveals the right description of the interfacial heat flux, and the shortcomings of PGM in including full anharmonicity of vibrational modes.

Subsequently, we question the traditional nanofluid theory that substantiates the presence of nanolayers and Brownian motion (otherwise termed as ‘dynamic’ modes of thermal conductivity) in enhancing thermal conductivity of nanoparticle suspensions. To assess the role of dynamic mechanisms, a rigorous study based on equilibrium molecular dynamics (MD) simulations was conducted. We identify that the abnormally high thermal conductivity reported in prior studies is due to an error source originating from the artificial correlations of periodic images of atoms in the simulation system. We also devise a method to alleviate these artificial correlations and calculate thermal conductivity accurately. Hence, an alternative explanation to the unusually high thermal conductivity of nano-suspensions obtained using Green-Kubo relations is provided.

Finally, building on the knowledge of how the transport properties are affected by the nanometer length scales involved, a detailed numerical analysis of flame propagation in nano-aluminum (nAl) - water (H₂O) mixtures was performed. Considering a multi-zone framework, the nonlinear energy equation is solved iteratively using the Gauss-Seidel method. Thermal conductivity of nanoparticles is modeled using thermal conductivities of aluminum and oxide layer, as well as interfacial conductance. The effective thermal conductivity of the mixture is modeled using the Maxwell-Eucken-Bruggeman model as a function of temperature, spatial coordinate, and local mixture composition. Sensitivity of linear burning rate, r_b to changes in thermal conductivities of aluminum (k_{Al}) and aluminum

oxide ($k_{Al_2O_3}$), and interface conductance (G) is also studied for various particle sizes in the nanometer range. This study illustrates how the nanoscale effects on the transport properties ultimately impact the combustion wave propagation in nanoenergetic materials, providing a solid foundation to their bottom-up rational design.

CHAPTER 1. INTRODUCTION

This chapter introduces the concept of nanoenergetic materials. The significance of metal-based nanoenergetic materials in this century, as well as prior works reporting experimental and the theoretical study of combustion of nanoenergetic materials, are reviewed. The unique mechanism of ignition of nanomaterials is also discussed. Furthermore, the role of heat conduction in nanoparticle suspensions is reviewed, and the major mechanisms that govern heat conduction are described. The rate of heat conduction is found to be a crucial factor that governs burning rate in nanoenergetic materials. Despite its significance, however, the conduction rate has not received much attention in the past. Therefore, the motivation of research drawn from the survey of literature is to fundamentally understand heat transport in nanoparticle suspensions. Finally, the research methodology and dissertation outline are presented.

1.1 Nanoenergetic materials

Energetic materials are typically defined as substances with large amounts of stored chemical energy and high rates of energy release. They can be classified based on composition as either monomolecular or composite. In monomolecular energetic materials, such as TNT, fuel and oxidizer groups are present in the same molecule [3] whereas in composite energetic materials, fuel and oxidizer are separate phases [4]. They are predominantly used in space and underwater propulsion, explosives, pyrotechnics, and energy generation applications [5]. Figure 1.1 compares the volumetric and gravimetric

energy densities of some commonly used energetic materials. As can be seen from the figure, metal-based energetic materials have higher volumetric energy densities than their hydrocarbon counterparts [6]. For example, the volumetric energy density of aluminum (Al) is 83.8 MJ/L, which is substantially greater than that of some common explosives (TNT ~10.8 MJ/L) and fuels (liquid hydrogen compressed at 900 bar ~ 9.17 MJ/L and jet fuel JP-8 ~ 42.8 MJ/L). High energy density metals include boron (B), beryllium (Be), Al, silicon (Si), and titanium (Ti). Among the metals, B has the highest energy density, followed by Be. However, B experiences delayed ignition, due to the formation of B_2O_3 , which significantly inhibits further oxidation. Be is extremely scarce and forms toxic gas products. Al, on the other hand, is one of the most abundant metals in the earth's crust and has a low cost of extraction, making it the most popular ingredient in energetic material compositions.

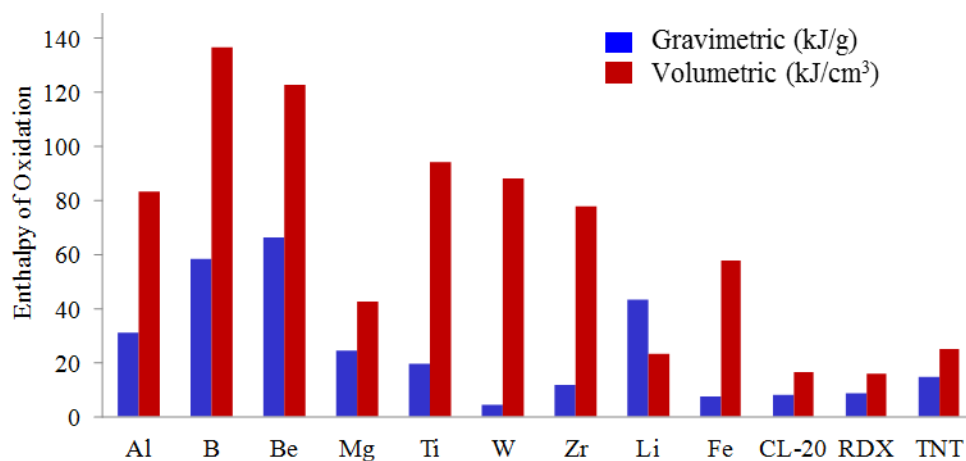


Figure 1.1 - Comparison of volumetric and gravimetric enthalpy of oxidation (energy content) of metals and widely used monomolecular energetic materials [6]

Macro and micron-sized Al particles have been routinely used in combination with various oxidizers and binding agents to create solid propellants since the 1950's. The most

widely used oxidizer in solid propellants is ammonium perchlorate (AP), which is structurally integrated with Al using polymeric binders like hydroxyl-terminated polybutadiene (HTPB) [7] and polybutadiene acrylonitrile (PBAN) [8]. The resulting composite material offers high thrust, simplicity, and reliability, and low-to-medium specific impulses (depending on the composition and operating pressure) of 180–260 s. They are used in early stage propulsion in rockets (solid rocket boosters), hypersonic propulsion, and descent stage retrorockets for e.g. NASA Mars rovers. Al has also been used as an additive for liquid propellants [9] and conventional fuels [10] to improve their energy density. In addition to space and underwater propulsion, Al energetics can also be used for applications in interceptors, missiles, etc., where high thrust to overall weight of the motor is crucial, and for military applications like explosives and pyrotechnics, where large amounts of energy need to be stored in small volumes.

Micron-sized Al particles nonetheless suffer from several drawbacks such as high ignition temperatures, agglomeration, and low reaction rates, resulting in low energy release rates.[4, 11, 12] The advent of nanotechnology and concurrent developments in synthesis and characterization techniques have offered new opportunities to realize different properties with nanomaterials and the possibility of using them as additives in energetic compositions. Nanomaterials are substances with characteristic dimensions <100 nm. They exhibit substantially different physicochemical properties compared with their micron-scale counterparts. They have lower melting and boiling temperatures [13], lower ignition time and temperatures, lower activation energy of oxidation [14] and enhanced chemical activity due to higher specific surface area (SSA) and surface energy [15]. Higher surface energy originates from the fact that nanoparticles have a higher percentage of

surface to bulk atoms in comparison with micron-sized particles. These surface atoms are non-bonded/partially bonded compared with the bulk atoms, resulting in an enhanced chemical reactivity. Likewise, specific surface area (or the surface area per unit volume of nanoparticle) also increases as the nanoparticle size reduces, resulting in enhanced fuel-oxidizer intimacy leading to higher reaction rates. In addition, due to the large SSA, nanoparticles also offer tailorable surface properties that have the potential to allow precision control of thermal transport and chemical kinetics [16, 17]. Hence, during the mid-1990's, widespread replacement of microparticles with nanoparticles created a new class of energetic materials called nanoenergetic materials.

Among the various physical forms of nanoenergetic materials, nanoparticle-laden fluids, or 'nano-suspensions', have received considerable attention, owing to their ease of manufacture and relative structural stability.[12] Nanosuspensions are suspensions of solid fuel nanoparticles in an oxidizer medium. The oxidizer can be in solid, liquid, or gaseous state, giving rise to a solid-sol, gel, or aerosol respectively. Irrespective of the surrounding oxidizer, nano-aluminum (nAl) particles possess a unique ignition mechanism in comparison with micro Al particles. The following section summarizes the ignition and combustion mechanism of nAl.

1.2 Mechanism of ignition and combustion of nano-aluminum: Phenomenological understanding

Ignition and combustion of micron-sized aluminum particles has been a topic of experimental and theoretical studies for several decades.[4, 11, 12, 16, 18-22] Although combustion follows ignition, it is better to observe and optimize combustion behavior first,

as it paves way towards a logical explanation of the ignition mechanism. A characteristic property that can be used to represent combustion behavior is the particle burning time. Figure 1.2 summarizes the experimental results of particle burn time as a function of particle size. As can be seen from Figure 1.2, for particles of size $> \sim 20\mu\text{m}$, mass-diffusion is the rate limiting mechanism, and therefore combustion becomes diffusion-limited. At these length scales, the burning time, t_b follows the d^2 law, i.e., it is proportional to the square of particle diameter ($t_b \propto d^2$).

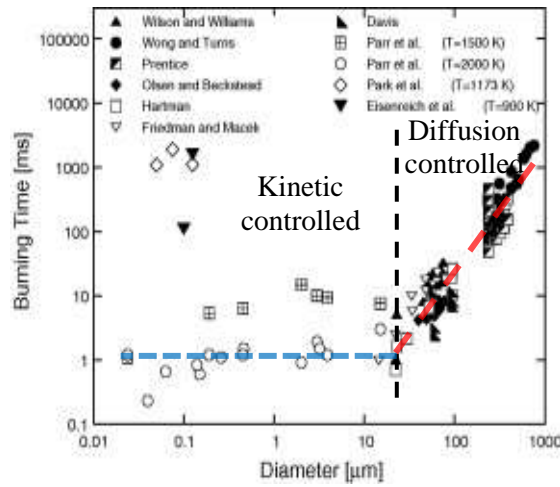


Figure 1.2 Burning time of Al particles as a function of mean particle diameter obtained from experimental results. [12]

At smaller length scales, quadratic dependence of t_b on particle diameter breaks down, as shown in Figure 1.2. The equation becomes $t_b \propto d^n$ where $n \sim 1.1-1.2$. In a recent review article, Sundaram *et al.* [23] point out that the combustion of nAl in various oxidizer environments deviates from d^2 law, as shown in Figure 1.3. Based on a phenomenological understanding, they demarcate the two particle size regimes: where the d^2 scaling is valid, and where it fails. Their observations indicate a kinetically controlled combustion occurs

for particle sizes $< 100 \mu\text{m}$; in other words, the combustion wave resembles a premixed flame.

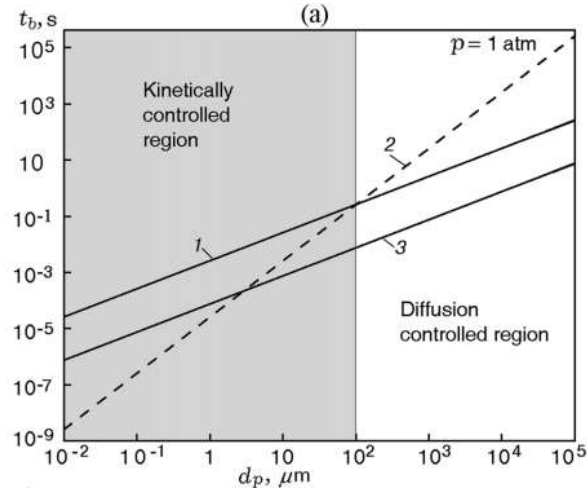


Figure 1.3 Particle size regimes where kinetic and diffusion controlled combustion are observed in experimental studies [23]

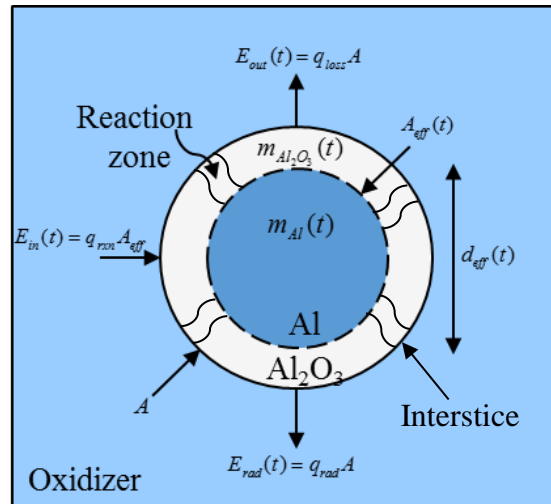


Figure 1.4 Energy balance where the control volume represents an aluminum nanoparticle suspended in an oxidizer medium

Since we have established that the combustion in nano aluminum suspensions is likely to be kinetically controlled, let us take a step further to understand the mechanism of combustion at the particle level. Figure 1.4 shows the control volume of system with a gaseous oxidizer encapsulated by nanoparticle in the reaction zone. The nascent fuel (Al) nanoparticle remains passivated during the gas phase synthesis process by a thin layer of aluminum oxide (Al_2O_3), unless a coating material with better affinity is provided during the process of synthesis. Experimental measurements have shown an ignition temperature of ~ 1360 K [12, 18, 22, 24]. The melting point of Al is 933 K and that of Al_2O_3 is 2345 K. At this temperature, therefore, Al exists in molten state and Al_2O_3 remains in solid state.

Ignition of nAl is preceded by an important phase change phenomenon: melting of the Al core to form liquid aluminum, which in turns escalates the pressure inside the nanoparticle and cracks the oxide layer [23]. Al atoms diffuse out through the cracks in the oxide layer while mixing with oxidizer molecules that diffuse inwards. The exact location of the reaction zone is not completely understood, but it is convenient to assume that it lies somewhere within the interstices of the oxide shell. This assumption also leads one to assume the production of new oxide molecules which adds to the shell thickness. Other products diffuse away from oxide shell. A part of the heat generated from the reactions, E_{in} gets conducted into the nanoparticle, and a part of it conducts upstream towards the unreacted mixture, which in turn preheats it. A portion of the energy at the reaction surface, E_{rad} , gets radiated upstream to preheat the unburnt mixture. It has been shown in prior studies that more than 99% of preheating occurs due to conduction, and the contribution from radiation is less than 1% [25]. There is also a heat loss, E_{out} from the particle to surroundings via radiation and conduction.

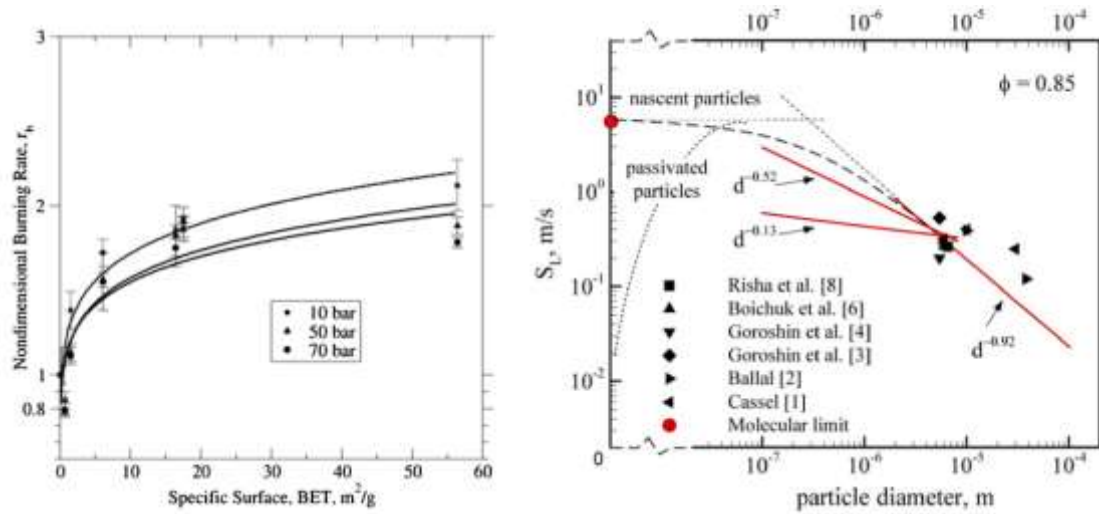


Figure 1.5 (a) Linear burning rate of Al composite as a function of specific surface area (SSA) and (b) Flame speed in Al-air mixture as a function of particle diameter [20]

As seen in Figure 1.4, as the reaction proceeds, the thickness of aluminum oxide layer on the nanoparticle increases. This decrease reduces the molecular-level interactions between fuel and oxidizer. Hence, one may expect that, as particle size reduces further, the net reaction rate saturates. A corroborating observation can be made from Figure 1.5. Figure 1.5(a) represents the burning rate of a solid-sol propellant as a function of specific surface area (SSA). Note that increase in SSA represents a decrease in nanoparticle size. Figure 1.5(b), shows a reduction in flame speeds at much smaller length scales when compared to gas-phase combustion reactions. Therefore, in the kinetically controlled regime, as the size reduces beyond a certain small value, relative oxide layer content becomes sufficiently high that reaction rates become significantly lower than gas phase reactions. In this regime of saturated chemistry, there is no appreciable burning rate enhancement, despite the ostensible increased reaction rates owing to high SSA of nanoparticles. In this regime, therefore, one may think of various measures to improve

reaction rates: catalysis, surface functionalization, forced cracking of oxide layer, etc. Nonetheless, as an open question remains: by improving reaction rates, can we expect significant enhancements in linear burning rates?

1.3 Flame propagation in nAl mixtures: Experimental studies and theoretical modeling

There have been numerous experimental studies conducted to understand the burning properties of nAl in various oxidizers. Tyagi *et al.* [26] measured the ignition probability of diesel droplets laden with aluminum nanoparticles. The diameter of particles used was 50 nm. The droplets were allowed to fall from a height of 25 mm onto a 75 mm diameter stainless steel hot plate whose temperature varied in the range of 668-768 °C. The ignition probability increased by more than 100% due to the addition of nanoparticles. This increase was attributed to the increased reaction rates of nAl particles, resulting in faster and lower temperature ignition. In addition, the burning characteristics of liquid propellants such as nitromethane have been found to be enhanced by the addition of nanoparticles [17]. For example, the addition of ~1.3 wt. % of aluminum oxide nano-particles increased the burning rate of nitromethane by > 100%. This increase was attributed to the catalytic properties of the nanoparticle when dispersed in nitromethane. Apart from being used as additives in conventional propellants and fuels, novel energetic materials created by dispersing nanometallic particles in liquid oxidizers have also been studied. Risha *et al.* [22] considered a green energetic material consisting of nano-aluminum particles dispersed in water and studied the effects of pressure and particle size on the burning characteristics. The burning rate was inversely proportional to the particle diameter, and the pressure

exponent was in the range of 0.27-0.47, depending on the particle size. While the overall burning rate was significantly higher than micron Al particle suspensions, the underlying physics were not discussed.

Despite the enormous potential of nAl combustion in propulsion applications, there have been very limited theoretical studies reported in the literature that describe flame propagation in these systems. Sundaram *et al.* [18] performed a companion theoretical analysis for the experiments of Risha *et al.* [22] to investigate the effects of particle size and pressure on the linear burning rate, r_b of nAl-H₂O mixtures. Particle sizes ranging from 38-130 nm were considered for chamber pressures in the range 1-10 MPa. They used a mean particle burning time, τ_b , as a surrogate to the particle burning rate, given by[27]:

$$\tau_b = \frac{c[a_1 \exp(b_1 T) + a_2 \exp(b_2 T)]d_p^2}{p^m} \quad (1.1)$$

$$m = a_3 \exp(b_3 T) + a_4 \exp(b_4 T)$$

where the free parameters $c, a_1, a_2, a_3, a_4, b_1, b_2, b_3, b_4$ are free parameters that are optimized to experimentally measured burning times. Exact values of the free parameters and further discussion are given in Table 6.2 and Section 6.2.4 respectively of this thesis.

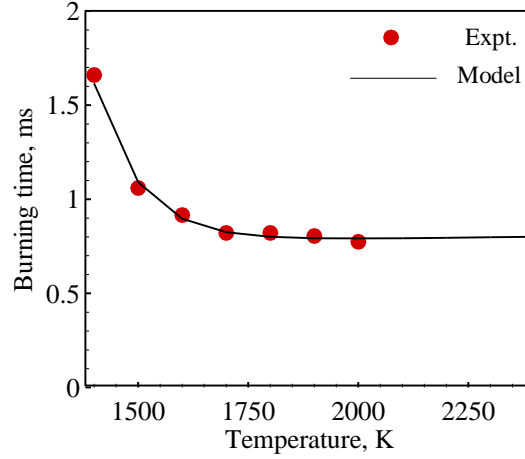


Figure 1.6 Comparison of nAl burning times predicted by Eq. 6.1 and experimental burning times [27] for a range of temperatures representative of the reaction zone of a flame

Figure 1.6 demonstrates the fidelity of the burning time model for a wide range of temperatures in the reaction zone of a nAl – water combustion system at 1 bar pressure, when compared with the experimentally obtained burning time values.[27] The burning time value at the ignition temperature (~ 1380 K) is > 1.5 ms, which reduces as we go to higher temperature due to the enhanced reaction rates. From Figure 1.6, it is quite clear that the mass burning time model captures the reaction kinetics explicity well.

Sundaram *et al.* [18] combined this independently benchmarked burning time model with an effective thermal conductivity model to model flame propagation in nAl- H_2O mixtures. The thermal conductivity of Al and water were assumed to be constant throughout preheat and combustion zones. An effective thermal conductivity was calculated using an effective medium theory approach, which was originally developed for micron Al particles without accounting for the size and random distribution of particles. Results of their studies are summarized in Figure 1.7. These methods overpredict r_b for particle sizes 80 and 130 nm for all pressures when compared with experimental results.

The mean error in r_b for 130 nm particle is ~25%, whereas for the 80 nm particles, the error increases to 31%. For 38 nm particles, the predicted quantitative and qualitative trends differ substantially from the experimental results. In addition, the mean error is more than 50%, with a peak error in r_b of 104% at 3.5 MPa. Risha *et al.* attributed this error to the adsorption of water molecules to the nanoparticle surface, which prevents diffusion towards Al atoms within the core.

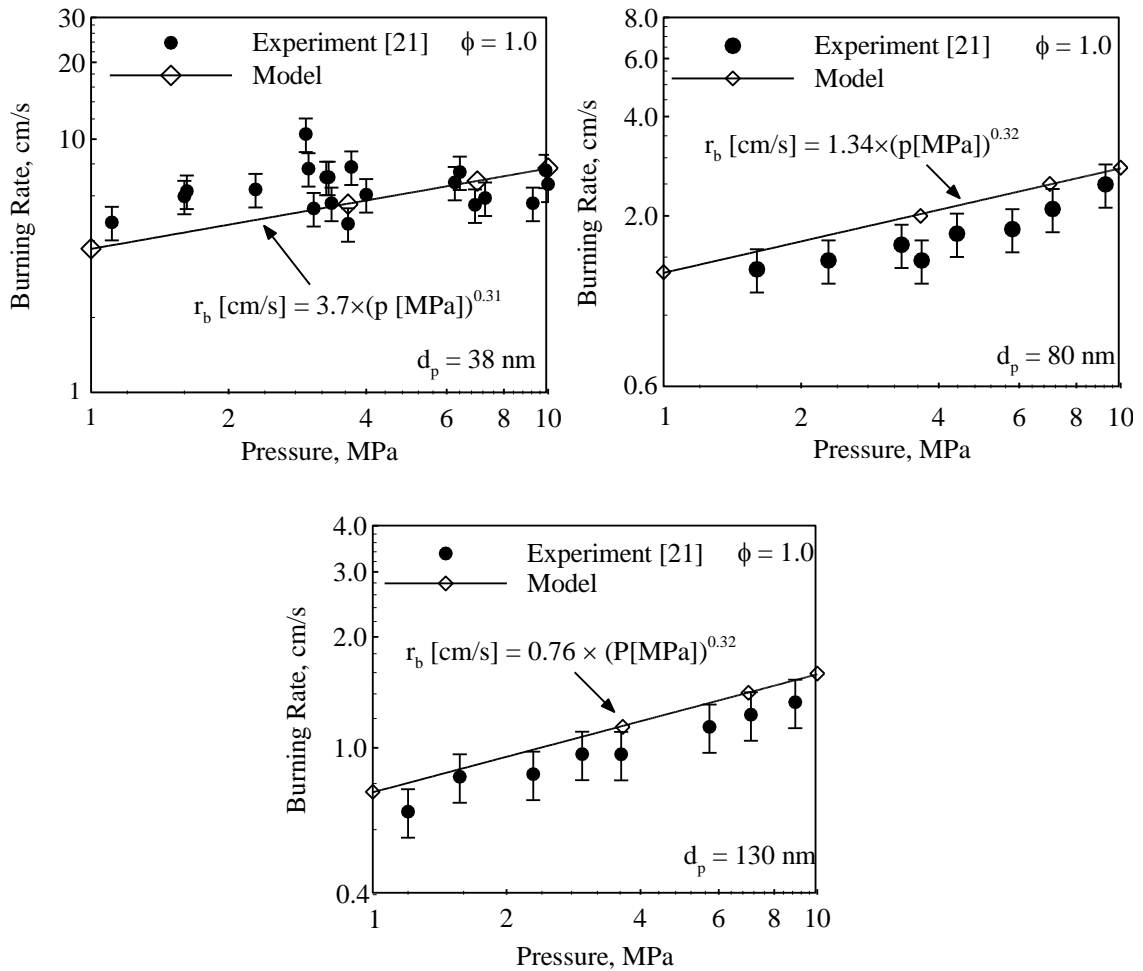


Figure 1.7 Comparison of linear burning rates predicted by the model[18] with experimental values as a function of chamber pressure for a) 38 nm, b) 80 nm, and c) 138 nm particle suspensions

Recently, an attempt has been made to determine a suitable thermal conductivity model for heterogeneous metal-based energetic materials by investigating the effect of particle volume fraction on the burning rate of nickel-clad aluminum pellets in an argon environment [24].

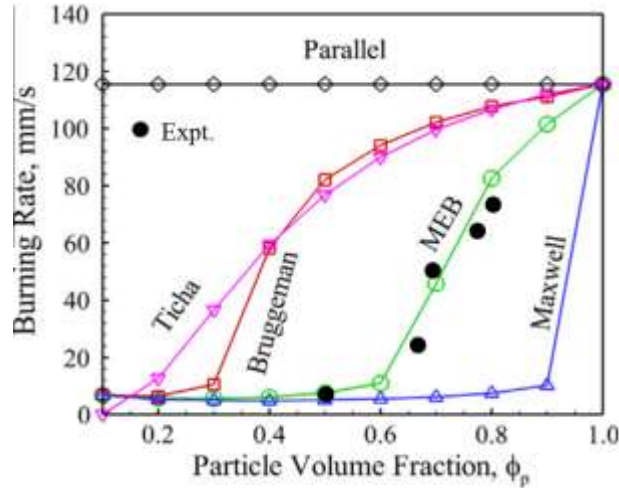


Figure 1.8 Comparison of linear burning rates as a function of nanoparticle volume fraction predicted by using different effective thermal conductivity models with experimental data [24]

The volume fraction was varied in the range of 10-100% of theoretical maximum packing density. Four different classical effective thermal conductivity models were considered and their predictions are shown in Figure 1.8. In addition, Maxwell-Eucken [28, 29] and Bruggeman [30] theories were unified. The resulting Maxwell-Eucken-Bruggeman model offered the most accurate predictions of the burning rate for all loading densities. However, the mean error in predicted burning rates were still $> 10\%$, and the large errors were attributed to nanoparticle agglomeration. While these works ascribe the large errors in burning rate prediction to various possible physicochemical phenomena,

there is sufficient grounds to hypothesize that this error is due to an oversimplification of nanoscale heat conduction physics and inadequate modeling of thermal conductivity.

Note that for kinetically controlled combustion, heat conduction rates from the reaction zone to the unburnt reactants is crucial in sustaining a flame. If heat conduction rates are low, the thin reaction zone (flame) can get quenched before the reactants get preheated to the ignition temperature, or if it does not, the resulting flame will be slow-propagating. If the conduction rates are very fast, heat is conducted out to the system walls, subsequently quenching the flame. Hence, it is certain that heat conduction is as important as chemical kinetics. Heat conduction rates can be characterized by the thermal conductivity of the system. Until now, thermal conductivity has not been given the attention it perhaps deserves, and has been approximated using somewhat *ad hoc* modeling approaches.

In summary, there is a significant disparity between predicted burning properties and experimental results [18]. Since chemical reaction rates are accurately captured by the burning time model, it is reasonable to assume that the inadequate modeling of thermal conductivity could be a reason for this disparity. To ensure a high-fidelity combustion model, it is imperative that an *atomistically* informed heat conduction model be incorporated. An atomistically informed model should ideally account for how thermal conductivity changes at the nanoscale. Similar to reaction kinetics, another open question is: can higher burning rates be achieved by improving the heat conduction properties of the system? To answer such a question, it is important that we first understand the physics of heat conduction in a nano-suspension.

1.4 Thermal conductivity of nano-suspensions

Thermal conductivity, k , is the constant of proportionality in Fourier's law of heat conduction that relates a heat flux density (Q) to the local temperature gradient (∇T), given by,

$$Q = -k\nabla T. \quad (1.2)$$

Thermal conductivity in solids is a property that consists of cumulative contributions from different types of heat carriers, namely electrons and phonons. A nano-suspension is a dispersion of nanoparticles in a fluid medium. To model effective thermal conductivity of nAl-H₂O mixtures, a fundamental understanding of the physics of heat conduction in nano-suspensions is required. The various components of the system are oxide coated nAl particles (Al core and Al₂O₃ shell) dispersed in a fluid as shown in Fig. 1.9.

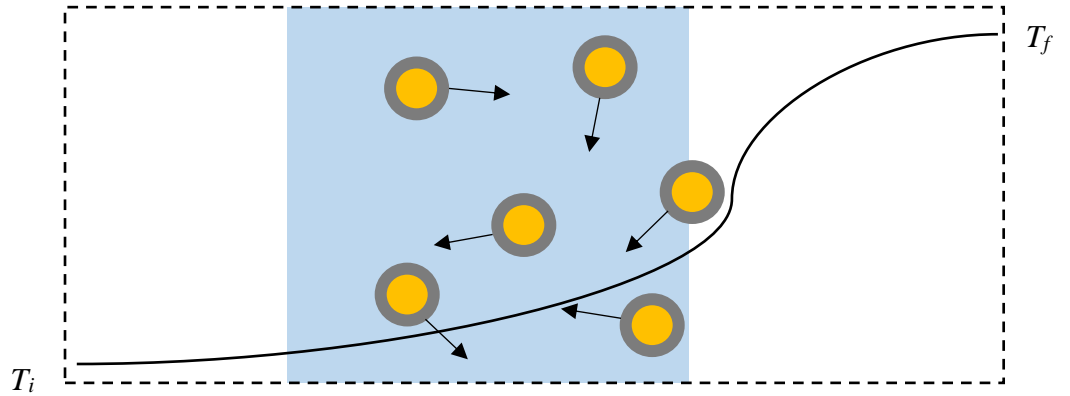


Figure 1.9 Schematic diagram showing nAl particles coated by an oxide layer dispersed in water. Temperature profile shows initial (T_i) and final (T_f) temperatures. Nanoparticles move around within the system in random directions, as shown by the arrows.

As can be seen from Figure 1.9, at any given instance, the particles undergo Brownian motion (random motion due to the collision of fluid molecules on the surface resulting in a net unbalanced force) with velocities indicated by the arrows. In theory, the effective thermal conductivity of the system has the following components: i) thermal conductivity of the core-shell nanoparticle, ii) thermal conductivity of the fluid, and iii) contributions to thermal conductivity due the *dynamic* modes of heat conduction. Thermal conductivity of the core-shell particle has contributions from thermal conductivity of the Al core, the Al₂O₃ shell, and the Al/Al₂O₃ thermal interfacial conductance (TIC). Temperature dependent thermal conductivities of bulk Al and Al₂O₃ have been experimentally studied and documented [31-33]. Availability of thermal interfacial conductance data is very limited (only in the temperature ranges: 50-480 K) and the temperature dependence of conductance is unknown beyond 480 K [34, 35]. The thermal conductivity of different oxidizers has also been characterized and documented. The term *dynamic* mode is quite misleading. It was first introduced to explain the enhanced thermal conductivity in nanofluids. Nanofluids are a class of heat transfer fluids which are dilute (<1% volume fraction) suspensions of nanoparticles in a fluid medium. The dynamic modes of heat conduction in a nanofluid are associated with Brownian motion and nanolayering [36]. Brownian motion is the random thermal motion of suspended particle within the system. Nanolayering is the phenomenon by which the fluid forms a high-density crystalline layer on the surface of the nanoparticle due to its adhesive properties. The existence of these dynamic modes is highly disputed [37-41]. There are numerous works in the literature [37, 38, 40] suggesting the presence of these dynamic modes, that

also propose theories to support it, though lately, these theories have been called into question [42-44]. In the following sections, we will look at these effects in detail.

1.4.1 Size-dependent thermal conductivity of nanoparticles and the oxide layer

The thermal conductivity of nanoparticles can be several orders of magnitudes lower than that of bulk material. There is a vast amount of literature available on size dependent thermal conductivity of materials [45, 46]. As particle size decreases, the percentage of surface atoms increases, and boundary scattering of heat carriers become increasingly significant. Due to the small size of the system, large mean free path (MFP) carriers undergo higher rates of scattering which limits their ability to contribute to heat transport. Chen *et al.* [47, 48] studied the effect of particle size on the thermal conductivity of a nanoparticle. Figure 1.10 shows the ratio of size affected thermal conductivity to bulk thermal conductivity as a function of particle size to carrier MFP (L/Λ). Three distinct heat conduction regimes can be identified: ballistic, quasi-diffusive, and diffusive regimes. In the ballistic regime, heat carriers undergo negligible collisions and heat is transported between the two ends of a material maintained at different temperatures by the direct motion of heat carriers between them, i.e., ballistic motion. In the diffusive regime, carriers undergo significant scattering, and energy diffuses across the material. The quasi-diffusive regime is a hybrid of the ballistic and diffusive regimes where a portion of heat carriers contribute ballistically while the remaining ones experience scattering.

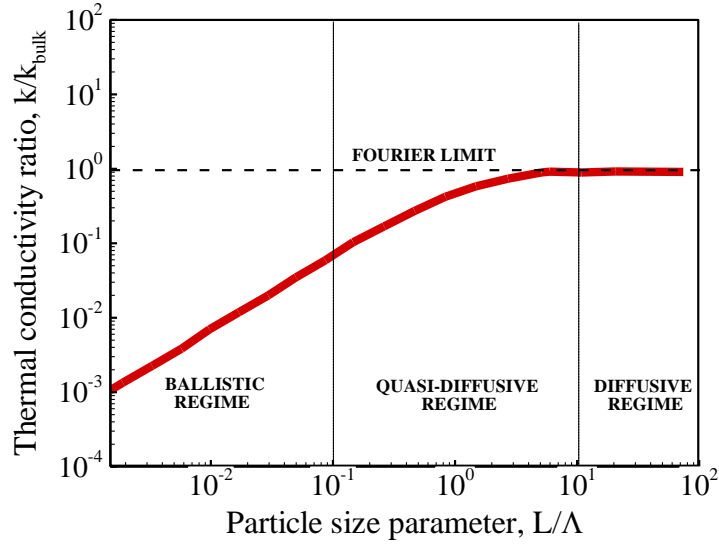


Figure 1.10 Dependence of thermal conductivity on the particle size and carrier mean free path as described by Chen et al. [48] showing ballistic, quasi-diffusive, and diffusive regimes of heat conduction

Hence, thermal conductivity in the nanoscale regime, as opposed to micro and macroscale regimes, is no longer simply a material property, but rather is dependent on the ratio of carrier MFP to system size. The heat carriers in solids are phonons and electrons. A phonon is a collective excitation of atoms in molecules or solids. A phonon is a quasi-particle that represents a quanta of energy associated with a given normal mode of vibration. Phonons are the major carriers of heat in insulators and semiconductors. Electrons, especially free electrons, are a major heat transport mechanism in metals. The MFP of electrons is on the order of a few nanometers [49], and that of phonons can range from 10^0 - 10^4 nanometers [49, 50]. As the size of the system becomes comparable to or lower than the MFP of the heat carrier, the heat conduction mechanism ceases to be completely diffusive and begins to take on a quasi-diffusive or ballistic nature. Both an Al

nanoparticle and its oxide layer coating can be affected by size effects, warranting further investigation.

1.4.2 Thermal interfacial conductance and resistance (TIC, TIR)

Interfacial heat transport can be characterized by thermal interfacial conductance (TIC), G , which is the inverse of thermal interfacial resistance (TIR), R . G is the constant of proportionality in the equation that relates heat flow, Q , at the interface of two materials to the temperature drop/discontinuity, ΔT , at the interface ($Q = G\Delta T$). TIC becomes increasingly important as particle size reduces because of the relatively large ratio of interfacial area to particle volume. It occurs due to the difference in vibrational properties of the two materials in contact. The importance of TIC in heat conduction can be understood via a simple analysis following the series resistance circuit analogy. Let us first consider a series circuit model representing the interface of Al and Al_2O_3 as shown in Figure 1.11.

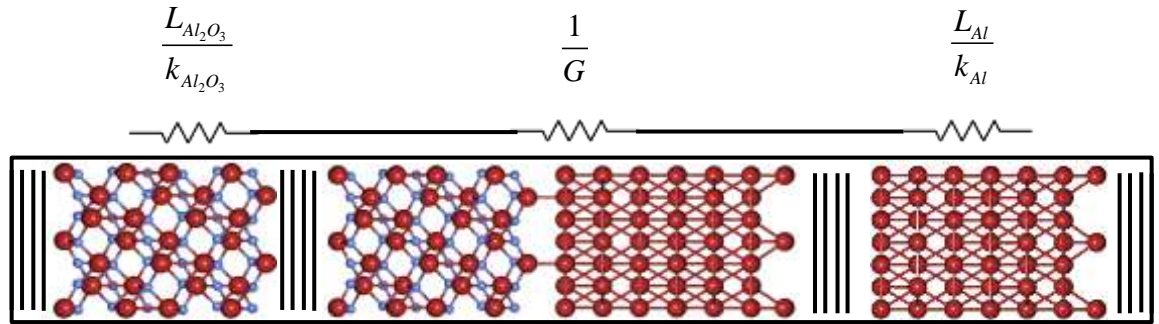


Figure 1.11 Series circuit framework for evaluating thermal conductivity of nanoparticle

This circuit is a partial representation of the nano-aluminum particle with oxide coating. It consists of three main components: bulk Al whose thermal conductivity is

denoted by k_{Al} , bulk Al_2O_3 whose thermal conductivity is denoted by $k_{Al_2O_3}$, and the interface whose conductance is denoted by G . The thermal resistance of Al_2O_3 , Al, and the interface are given as $\frac{L_{Al_2O_3}}{k_{Al_2O_3}}$, $\frac{L_{Al}}{k_{Al}}$, and $\frac{1}{G}$ respectively. L denotes the length of each material. The effective conductivity of the entire system including the interface, k_{int} can be obtained from the net resistance from adding the component resistors in series:

$$k_{int} = \frac{L}{\left(\frac{L_{Al_2O_3}}{k_{Al_2O_3}} + \frac{L_{Al}}{k_{Al}} + \frac{1}{G} \right)} \quad (1.3)$$

This concept can be extended to estimate the thermal conductivity of a passivated nAl particle of total diameter D_p , and can be given as:

$$k_p = \frac{D_p}{\left(2 \frac{L_{Al_2O_3}}{k_{Al_2O_3}} + \frac{D_p}{k_{Al}} + \frac{2}{G} \right)}. \quad (1.4)$$

Using Eq. (1.4), it can be found that if $G \sim 1 \times 10^6$ W/m²K, then the interface comprises 90% of the total resistance. On the other hand, if $G \sim 1 \times 10^9$ W/m²K, less than 10% of resistance to heat flow originates from the interface. Therefore, depending on the magnitude of G , it is clear that it could be of the most crucial parameters in determining the net resistance of the medium to heat conduction. Furthermore, using different values of TIC and particle sizes, the effective thermal conductivity enhancement, k_{eff}/k_f of a suspension of Al nanoparticles can be evaluated using the Maxwell model of effective thermal conductivity:

$$\frac{k_{eff}}{k_f} = \left[\frac{k_p + 2k_f + 2(k_p - k_f)\phi}{k_p + 2k_f - (k_p - k_f)\phi} \right], \quad (1.5)$$

where ϕ is the volume fraction, k_p and k_f are the thermal conductivities of particle and fluid respectively. Results of solutions of Eq. 1.5 for various hypothetical values of G and particle sizes are presented in Figure 1.12.

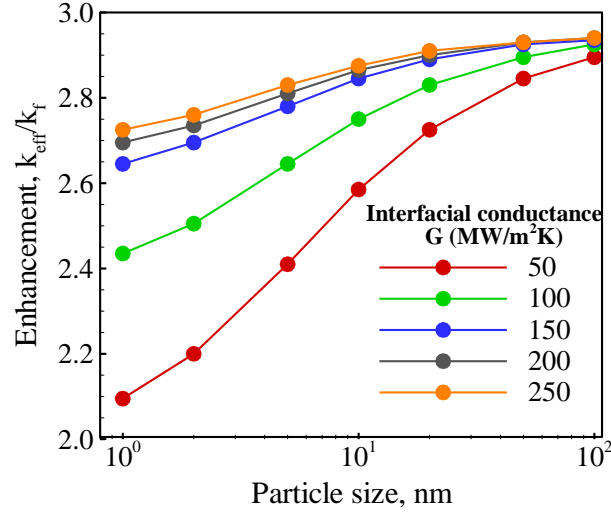


Figure 1.12 Thermal conductivity enhancement of a nanoparticle suspension as a function of particle size for various interfacial conductance values

These results show that for smaller particle size, thermal conductivity enhancement changes noticeably from 2.1 to 2.8 when G is varied from 50 to 250 MW/m²K. As the particle size increases, the sensitivity of thermal conductivity enhancements to changes in TIC is negligible. The TIC of Al/Al₂O₃ has not been widely studied, as there are only three Time-domain Thermoreflectance (TDTR) experimental data sets available in the literature [34, 35, 51]. G is available only for temperatures ranging from 50-480 K, in which case the value ranges from 10 MW/m²K to 300 MW/m²K. Experimental methods can get challenging and expensive especially from a standpoint of making clean and defect-free interfaces by epitaxial growth, and achieving high temperatures and/or pressures. For

instance, beyond 480 K, experimental measurement is challenging because Al atoms deposited on the Al_2O_3 surface tend to evaporate at higher temperatures. Realistically, a combustion system will have regions with temperatures far in excess of 480 K and for $T > 933$ K, Al will be in molten state. Once Al melts, it loses its crystallinity and therefore its ability to conduct by an organized vibration of the lattice. Hence, it is safe to assume that beyond the melting point of Al, TIC of Al/ Al_2O_3 interface could be significantly lower than that of the solid interface due to the loss of crystallinity of the Al lattice. Depending up on the magnitude of the drop in TIC value, the molten Al/ Al_2O_3 could potentially act as the most significant resistance in the combustion system, which can be evaluated from Eq. 1.4.

Nevertheless, the numerical values of TIC of Al/ Al_2O_3 at higher temperatures are totally unknown at this point. Since experimentation is challenging, an alternative is to use theoretical/computational methods. Most of the existing methods are based on the phonon gas model (PGM), but none of the PGM-based methods have been able to achieve experimental validation, because the PGM does not correctly account for interfacial physics. Hence, a more fundamental approach to computing TIC is essential.

1.4.3 Dynamic heat conduction mechanisms

When compared with the thermal conductivity of dispersed solid particles, thermal conductivity of the surrounding fluid is two orders of magnitude lower. For example, consider a suspension of Al_2O_3 particles ~ 100 nm in diameter dispersed in water. The thermal conductivity of Al_2O_3 is $\sim 30 \text{ W m}^{-1} \text{ K}^{-1}$ whereas that of water is 0.6 W/m-K . Therefore, the resistance offered by fluids to heat conduction is intrinsically quite large. In

such cases, one may naturally try exploring other possible features in nano-suspensions that can be exploited to reduce the thermal resistance of fluids. Towards this end, two important phenomena that prior researchers have investigated are Brownian motion and nanolayering [36]. Numerous attempts have been made to assess the contribution of different mechanisms to thermal conductivity enhancement and gain in-depth understanding of underlying processes and mechanisms.

The interfacial layer formed at the particle surface due to the adsorption of base-fluid molecules possesses higher density and some order/crystallinity compared to the bulk fluid. It is hypothesized that such a layer acts as a thermal bridge, effecting heat transfer between the solid and fluid media, enhancing the transport. There is, however, little experimental data to corroborate this hypothesis. Over the last decade, there have been several attempts to include nanolayering in classical thermal conductivity models.[52, 53] Yu and Choi [52] developed a modified Maxwell model, by treating a particle-nanolayer core-shell complex dispersed in the base-fluid. By judiciously choosing a constant nanolayer thickness of $\sim 2\text{-}3$ nm and nanolayer thermal conductivity of $10\text{-}100 k_f$, reasonable agreement with experimental data was achieved. The core-shell complex particle assumption was also used by several other researchers to develop effective thermal conductivity models [54, 55]. These models yield only qualitative descriptions of the variations of effective thermal conductivity with particle volume fraction and particle size. Molecular dynamics (MD) simulations [56] also support the notion of a dynamic interfacial layer in promoting heat transport rates of suspensions. Eapen *et al.* [56] conducted equilibrium MD (EMD) simulations to calculate thermal conductivity of platinum-xenon (Pt-Xe) nanofluids. Dilute suspensions of volume fractions $< 1\%$ were considered, and a

Lennard-Jones (LJ) potential was employed to model atomic interactions. Thermal conductivity was calculated using Green-Kubo relations. It was found that the potential energy correlation between particles and the fluid contributes to the enhanced thermal conductivity. The work suggests that the dynamic interfacial layer at the particle surface plays a significant role in enhancing heat transport properties of nanofluids. A correlation between thermal conductivity enhancement and nanolayer properties was, however, not reported. Non-equilibrium MD (NEMD) studies have also been conducted to evaluate the thickness and thermal conductivity of the nanolayer [57, 58]. Based on the radial distribution function and density profiles, the thickness of the nanolayer was estimated to be about 1 nm [58], and the in-plane thermal conductivity of the nanolayer was ~ 2.5 times the thermal conductivity of the base-fluid. Note, however, that these works suggest that nanolayer thermal conductivity does not substantially affect heat transport rates in suspensions. It should also be noted that in most of the MD studies, atomic interactions were modeled using the Lennard-Jones (LJ) potential, which does not always offer accurate descriptions of atomic interactions for many practical materials of concern.

It is well known that particles suspended in a base-fluid undergo Brownian motion [59]. This motion can further induce convection of fluid molecules in the vicinity of the moving particle [36, 60]. The role of Brownian motion in enhancing the thermal conductivity of nanofluids has also been studied extensively [41, 61]. Das *et al.* [41] measured the thermal conductivities of Al_2O_3 and CuO nanofluids for different temperatures and particle sizes. The temperature was in the range of 21-51 °C, and the particle size was 38.4 nm for Al_2O_3 and 28.6 nm for CuO . It was hypothesized that Brownian motion is significant only below a critical particle size and beyond a critical

temperature, both of which are particular to the suspended material. Brownian dynamics [61] and MD simulations [42, 62] have also been performed to study the role of micro-convection. Sarkar et al. [62] conducted EMD simulations to calculate the effective thermal conductivity of an argon fluid dispersed with copper nanoparticles. The particle volume fraction varied between 0.4 and 8.0 %. The temperature was maintained constant at 85 K using a Nose-Hoover thermostat. The LJ potential was used to model interatomic interactions. The calculated thermal conductivities were marginally greater than the predictions of the Hamilton-Crosser model. Furthermore, at low particle volume fractions, the self-diffusion coefficient of base-fluid molecules steadily increased with increasing particle volume fraction, suggesting that it is possible that the Brownian motion-induced-micro-convection can result in a thermal conductivity enhancement. However, results from the EMD simulations of Babaei *et al.* [42], when incorporated with an order of magnitude analysis [63], suggest that the contribution of Brownian motion (and micro-convection) towards thermal conductivity enhancement is negligible. With the lack of consensus on the existence of these mechanisms, it is difficult to assess their quantitative contribution towards thermal conductivity enhancement in nAl-H₂O mixtures.

1.5 Research objectives

Based on the preliminary assessment, there is a significant gap in the understanding of thermal conductivity of nanosuspensions. *Prima facie*, interfacial conductance and size effects could be the crucial components of the effective thermal conductivity of the system. There is very limited experimental data on the TIC of Al/Al₂O₃ interface, of which none of the experiments have gone beyond 480 K. All the existing theoretical models to predict

TIC are based on the phonon gas model (PGM), which, to our knowledge, have not been able to predict TIC consistently accurately. In addition, size effects on thermal conductivity has also not been studied in detail or quantified yet for Al and Al_2O_3 . The debate over the existence of dynamic modes of heat conduction also remains unresolved. Surprisingly, all existing combustion models appear to have negated their explicit inclusion. This could be the major reason that the models yield spurious results for the burning properties. In light of these issues, the specific questions to be answered in this thesis are:

- 1) How to investigate size effects on thermal conductivity and how to quantify size effects on Al and Al_2O_3 ?
- 2) How to predict thermal interface conductance (TIC) of Al/ Al_2O_3 interface accurately? How does TIC vary beyond the melting point of aluminum? What are the vibrational modal contributions to interfacial conductance?
- 3) Do Brownian motion and nanolayer actually contribute towards thermal conductivity enhancement in nanosuspensions?
- 4) How to model flame propagation in realistic nanosuspensions by explicitly modeling particle thermal conductivity (with size effects and interfacial conductance)? What are the nanoscale heat transfer effects on combustion performance of nanoenergetic materials?

1.6 Dissertation outline

This dissertation is organized into seven chapters. Chapter 2 deals with the theoretical framework required to understand and evaluate thermal conductivity in bulk crystals, interfaces, and nano-suspensions. It also outlines the one-dimensional flame-

propagation framework used to study flame properties of a nanoenergetic material. Chapters 3 discusses the phonon transport properties in bulk aluminum and aluminum oxide via lattice dynamics and Boltzmann transport equation (BTE) calculations. This provides a foundation for understanding interfacial heat transport in the succeeding chapter. Chapter 4 presents a study of interfacial heat conduction in an Al/Al₂O₃ system and the underlying physics via the interfacial conductance modal analysis (ICMA) technique. Chapter 5 assesses the significance of dynamic effects, namely nanolayering and Brownian motion, on thermal conductivity enhancement in nanoparticle suspensions. Chapter 6 presents a numerical solution of a nonlinear energy equation and uses it to understand flame propagation in an energetic suspension of aluminum nanoparticles in water. The conclusions of the thesis are then summarized and suggestions for future work are presented in Chapter 7.

CHAPTER 2. THEORETICAL FORMULATION

In this chapter, the theoretical and numerical formulation of the computational approach used to solve the heat conduction problem and subsequent treatment of flame propagation in nanosuspensions is summarized. Firstly, the theoretical/computational methods used to investigate and model thermal conductivity of nanosuspensions are reviewed. Here, the formulation of density functional theory (DFT), molecular dynamics (MD), and lattice dynamics (LD) are reviewed and their application in solving the heat conduction problem is discussed. Then, the theoretical formulation of a one-dimensional flame propagation problem in a composite propellant is presented.

2.1 Introduction

Flame propagation in nanosuspensions is a multiscale problem. Figure 2.1(a) shows a schematic diagram of vertically downward flame propagation in a mixture of nAl-H₂O suspension clearly showing the temperature profile within the system. This is representative of the experimental setup of a constant pressure strand burner used to measure linear burning rates in propellants. [22] In this thesis, we will be attempting to study the nanoscale heat transfer effects on flame propagation from the standpoint of this particular system.

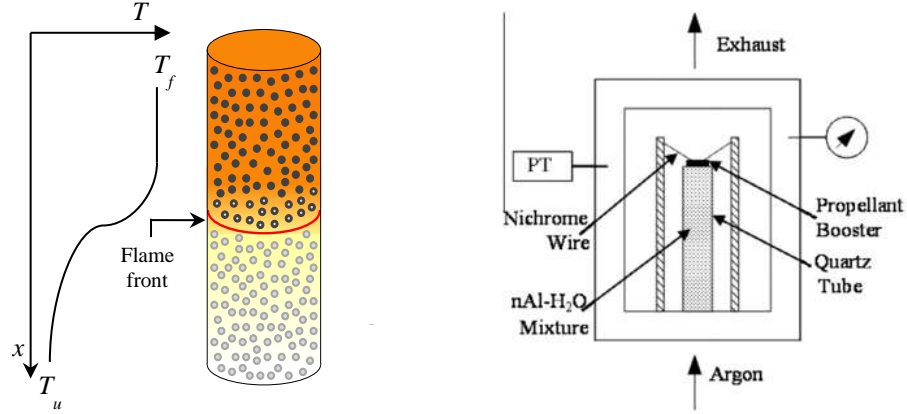


Figure 2.1 (a) Vertically downward flame propagation in a mixture of nAl and water showing the temperature profile within the system, and (b) Schematic of constant-pressure strand burner

To solve this flame propagation problem, we devise an atomistically informed mesoscale simulation strategy. Herein, the heat transport properties at the small scales are precisely evaluated and mathematically modeled as a function of various parameters (particle size, temperature, etc.), which are later used as inputs in a mesoscale numerical framework to solve the flame propagation problem. From Chapter 1, it is quite clear that in order to adequately model the effective thermal conductivity of nanosuspensions, we need to evaluate size-effects on the phonon thermal conductivity of Al and Al₂O₃, the TIC of Al/Al₂O₃ interface, and the role of Brownian motion and nanolayering, thereby respectively addressing the first three thesis questions. Insights from these studies would help in building a macroscale effective thermal conductivity model for nanosuspensions. Using this effective thermal conductivity model in conjunction with an independently benchmarked chemical kinetics model, a steady state solution to the flame propagation problem can be obtained.

Firstly, the phonon thermal conductivity of Al and Al₂O₃ can be evaluated by solving the phonon Boltzmann transport equation (BTE) under the relaxation time approximation (RTA). Inputs to this solution framework can be obtained from DFT-LD (or first principles LD) calculations. Likewise, TIC of Al/Al₂O₃ also needs to be evaluated from first principles. Conventionally, TIC of material interfaces are evaluated with the help of Lennard-Jones (LJ) potential in an MD framework due to lack of better options. However, in the Al/Al₂O₃ system, there is chemical bonding at the interface, and it may be wrong to assume that there are only van der Waals forces (as modeled by the LJ potential). Therefore, this interface needs to be modeled using a charge transfer interatomic potential obtained from the first principles.[64] An open question in TIC evaluation is on the role of electrons. The role of electrons in heat conduction across a metal/metal-oxide interface has not been conclusively proven but there is sufficient grounds to believe that it could be negligible for Al/Al₂O₃ interface due to the unavailability of free electrons on the Al₂O₃ side. Therefore, if the experimental values of TIC can be obtained computationally from merely including phonon contributions, then it can offer some evidence to the argument that the role of electrons is negligible.

First principle calculation methods like DFT attempt to find an approximate solution of Schrödinger wave equation [65]. Properties obtained from DFT calculations can be used as inputs in lattice dynamics (LD) [66] and molecular dynamics (MD) calculations [67]. LD can be used to study phonon properties in solids. Outputs (interatomic force constants) from LD calculations can be used to evaluate phonon properties like dispersion relations, density of states (DOS), and thermal conductivity. Size effects on thermal conductivity can also be quantified by evaluating the thermal conductivity

accumulation as a function of phonon mean free path (MFP). Similarly, MD is a promising tool for evaluating material processes and properties (Example: TIC) characterized by length scales ranging over tens of nanometers and timescales of over tens of nanoseconds. In MD, inputs from DFT calculations in the form of interatomic potentials (or force-fields) are used to evaluate the forces on atoms and thereby observe the time evolution of a system of interacting atoms by integrating these forces.[68] Once a quantitative and qualitative understanding of all the nanoscale properties are gained, they can be incorporated in macroscale thermal conductivity models of heterogeneous materials and used in flame solvers. Flame solvers are meso/macroscale solutions to problems wherein the energy equation is solved by finite difference methods (FDM), finite element methods (FEM), etc. In this chapter, a step-by-step account of theoretical formulation from nano to macro scales is given.

2.2 Density functional theory

2.2.1 Wavefunctions and Schrodinger's equation

To model atomic interactions from first principles, and to describe the behavior and bonding associated with valence electrons, quantum mechanics is necessary. In quantum mechanics, electrons are described by their wavefunction governed by the Schrödinger wave equation. The energy of a system can then be computed from the time-independent, non-relativistic form of the Schrödinger equation given as:

$$\hat{H}\psi_i(\vec{r}_1, \vec{r}_2, \dots, \vec{r}_N) = E_i\psi_i(\vec{r}_1, \vec{r}_2, \dots, \vec{r}_N) \quad (2.1)$$

where i is the imaginary number, h is the Planck constant, Ψ is the wavefunction, \hat{H} is the Hamiltonian operator, and r is the position vector. With the Born-Oppenheimer (BO) approximation [65], the motion of atomic nuclei and electrons in a molecule can be separated. It allows the wavefunction of the molecule to be broken into its electronic and nuclear components, expressed as:

$$\Psi_{total} = \Psi_e \otimes \Psi_n \quad (2.2)$$

where subscripts e and n denotes electronic and nuclear components respectively. The BO approximation makes it possible to compute the wavefunction in two less complicated consecutive steps compared with an otherwise complex partial differential eigenvalue problem in 162 variables (the spatial coordinates of the electron and the nuclei).[69] Under the BO approximation, the energy of electrons can be given as:

$$\hat{H}_{elec} \Psi_{elec} = E_{elec} \Psi_{elec} \quad (2.3)$$

$$\hat{H} \Psi(x_1, x_2, \dots, x_N; R_1, \dots, R_{N_n}) = E \Psi(x_1, x_2, \dots, x_N; R_1, \dots, R_{N_n}), \quad (2.4)$$

where x_1, x_2, \dots, x_N represent the spin and Cartesian coordinates of the electrons in the molecule, and R_1, \dots, R_{N_n} are the nuclear coordinates of the N_n nuclei in the molecule. The Hamiltonian operator is given by,

$$H = T_e + T_n + V_{en} + V_{ee} + V_{nn}, \quad (2.5)$$

where T represents kinetic energy and V represents potential energy. Subscripts e and n represent electronic and nuclear respectively. In order to compute the total energy, we need not know the complex $3N$ dimensional wavefunction. Evaluating the full wavefunction is computationally expensive. Hence a useful quantity called the electron probability function

can be utilized to approximate the energy of the system. This serves as the basis of DFT wherein the energy of the system is a functional of the electron density. Electron density can be given as:

$$\rho(\vec{r}) = N \int \dots \int |\psi(\vec{x}_1, \vec{x}_2, \dots, \vec{x}_N)|^2 ds_1 d\vec{x}_2 \dots d\vec{x}_N \quad (2.6)$$

And the energy of the system is given by:

$$E[\rho] = T[\rho] + E_{ext}[\rho] + E_{ee}[\rho] \quad (2.7)$$

Where E_{ext} is the energy due to interaction with external field, and E_{ee} is the electron-electron interaction energy. Among these, E_{ext} is straightforward, and can be calculated from the applied external field:

$$E_{ext}[\rho] = \int \hat{E}_{ext} \rho(\vec{r}) d\vec{r} \quad (2.8)$$

The electron-electron interaction energy can be computed from Coulomb interaction (electrostatic energy), J , and the total energy can be re-written as:

$$E[\rho] = T_s[\rho] + J[\rho] + E_{xc}[\rho] + E_{ext}[\rho]. \quad (2.9)$$

Here T_s is the non-interacting kinetic energy, and E_{xc} is the exchange-correlation energy, which represents the sum of error made in assuming classical nature to non-interacting kinetic energy and electron-electron interaction energy.

T_s and ρ can be evaluated by the Kohn-Sham approach. The Kohn-Sham approach relies on a fictitious reference system of non-interacting electrons introduced to have the same electron density as the system of interest [70]. These electrons move in a potential that takes into account the actual forms of electron correlation and the difference between the kinetic energy functional of the reference system and the real system. The kinetic and

electron-electron functionals can be approximated via Kohn-Sham approach, in which the density of electrons are given as a function of their orbitals, ϕ_i as:

$$T_s[\rho] = -\frac{1}{2} \sum_i^N \langle \phi_i | \nabla^2 | \phi_i \rangle \quad (2.10)$$

$$\rho(\vec{r}) = \sum_i^N |\phi_i|^2 \quad (2.11)$$

The Kohn-Sham approach lays the foundation for DFT calculations. In DFT, material properties are evaluated from the total energy. Therefore, the primary interest is to approximate E_{xc} with high levels of accuracy. There are several approximations such as local density approximation (LDA), generalized gradient approximation (GGA), hybrid exchange functional, etc. In this research, LDA is used for all DFT calculations because LDA is sufficiently accurate to study phonon properties of Al and Al₂O₃ at a much lower computational expense[71]. LDA may be mathematically represented as:

$$E_{xc}^{LDA}[\rho] = \int \rho(\vec{r}) \varepsilon_{xc}(\rho(\vec{r})) d\vec{r}, \quad (2.12)$$

$$\varepsilon_{xc}(\rho(\vec{r})) = \varepsilon_x(\rho(\vec{r})) + \varepsilon_c(\rho(\vec{r})), \quad (2.13)$$

where the $\varepsilon_x(\rho(\vec{r})) = -\frac{3}{4} \left(\frac{3\rho(\vec{r})}{\pi} \right)^{1/3}$ is the Dirac/Slater exchange energy of the gas.

There are several ways to implement DFT calculations. Throughout this dissertation, a self-consistent field (SCF) method is used to obtain the energy surface of the given crystal. SCF is an iterative method that involves selecting an approximate density function, and solving the Kohn-Sham equation until the convergence criteria are met. Only

the energies of the outer shell electrons are evaluated and the norm conserving Perdew-Zunger scalar relativistic pseudopotential was used to describe the core electrons.[72] The basis set chosen is projector-augmented wave formalism.

In this thesis, DFT calculations are used for two different purposes. 1) To generate large datasets of material properties that are used as inputs in LD and MD calculations, and 2) validate the accuracy of the empirical interatomic potential in predicting phonon properties. Firstly, to actualize a DFT-LD calculation of phonon properties of materials, we need to supplement the LD framework with large number of randomly perturbed geometries of crystal structures and the corresponding forces acting on atoms. This can be achieved via DFT calculations wherein high-throughput SCF calculations are performed following the random perturbation of atoms from their equilibrium positions. SCF calculations can be performed to find the resulting forces acting on the atoms. The displacement and force datasets can be collected and provided as input to the LD framework. Secondly, TIC of Al/Al₂O₃ interface needs to be calculated using MD simulations, which require interatomic potentials as input. Hence, before performing large scale MD simulations, it is important to benchmark the potential against the DFT data. The following sections describe how DFT results can be used in conjunction with other MD and LD to investigate heat conduction properties.

2.3 Molecular dynamics (MD)

Molecular dynamics (MD) is a computer simulation technique where the time evolution of a set of interacting particles (atoms, molecules, coarse-grained structures, etc.)

is obtained by numerically integrating their equations of motion [67]. In classical molecular dynamics, the equation of motion is Newton's law:

$$F_i = m_i a_i, \text{ and } a_i = \frac{d^2 r_i}{dt^2} \quad (2.14)$$

where F is the force, m is the mass, and a is the acceleration on particle i . Typical MD simulations can be performed on thousands of atoms for several picoseconds to nanoseconds. With the rapid progresses in parallel computing, it is now possible to simulate multimillion atom processes for several thousand nanoseconds in a matter of certain weeks [73]. The following sub-sections on potential functions and time integration gives an elaborated introduction to practical MD, and the sub-section on fluctuation-dissipation theorem presents the formalism for post-processing heat current data, and obtain thermal conductivity values.

2.3.1 Potential functions

In Eqn. 2.14, force is calculated as the negative gradient of the potential energy, V of the system:

$$F_i = -\nabla_{r_i} V(r_i, \dots, r_N) \quad (2.15)$$

$$V(r_i, \dots, r_N) = \sum_i \sum_{j>i} \phi(r_i, \dots, r_N) \quad (2.16)$$

Here, ϕ is the interaction potential. Choosing an appropriate potential is the crux of a MD simulation; the fidelity of the results is wholly dictated by the potential used. Eq. 2.17 represents an example potential function that only includes pairwise interactions. There are more complex 3, 4, and many-body potentials as well, but one simple 2-body potential is the LJ 12-6 potential, given by:

$$\phi_{LJ}(r) = 4\varepsilon \left[\left(\frac{\sigma}{r} \right)^{12} - \left(\frac{\sigma}{r} \right)^6 \right], \quad (2.17)$$

where, $1/r^{12}$ term represents the repulsion that dominates at small distances, while $1/r^6$ models a van der Waals attraction, ε denotes the depth of potential well and σ , the hard sphere diameter. The LJ potential is one of the simplest potential functions used to model van der Waals interactions.

A complete review on all the existing potentials is beyond the scope of this dissertation. As a general rule, one should choose potentials based on what properties are optimized. If calculating phonon thermal conductivity is of interest, one may resort to using the phonon-optimized potentials developed by Rohskopf *et al.*[74] by optimizing the free parameters of a potential functional form to phonon properties obtained from the first principles. They suggest that if the phonon density of states (DOS), dispersion relations, and thermal conductivity can be accurately predicted by a potential, then it is optimized for phonons, and can be used in large-scale MD simulations aimed at evaluating more computationally challenging properties (like TIC for example) that involve phonon interaction and transport. When considered more carefully, their work also provides a routine to benchmark other existing interatomic potentials against the phonon properties obtained from the first-principles. Hence, this work provides us means to assess the capability of any potential function to reproduce the phonon properties before they can be used in massive MD simulations. Below is an abbreviated summary of all the potential functions used in the current research in the increasing order of complexity. Additional information on each, including free parameters, can be found in Appendix A.1.

2.3.1.1 Extended simple point charge (SPC/E) potential

The extended simple point charge (SPC/E) is the most widely used potential for predicting thermal properties of water [75]. As the name suggests, a point charge is given to hydrogen and oxygen ions of the water molecule held together by a bond length and bond angle restriction. The potential energy is given as:

$$V = 4\epsilon \left[\left(\frac{\sigma}{r} \right)^{12} - \left(\frac{\sigma}{r} \right)^6 \right] + C \frac{q_i q_j}{r} \quad (2.18)$$

where q represents charges on atoms and C is a fitting parameter. SPC/E potential is used in this research to model atomic interactions in water, which is one of the components of the nanosuspension used in combustion applications. In Chapter 5, we have compared the results of the thermal conductivity values predicted by the SPC/E potential with experimental results and prior computational works. After making sure that the predictions of SPC/E potential are reasonably accurate for a wide range of temperatures, MD simulations are carried out for a system of Al_2O_3 nanoparticle suspended in water. In this system, Vashishta potential[76] is used to model atomic interactions in Al_2O_3 , as described in the next section.

2.3.1.2 Vashishta potential

The Vashishta *et al.* potential is used to simulate atomic interactions in the Al_2O_3 system [76]. As the material involves more interactions from electrostatic forces, dipoles, steric effects, etc., LJ potential ceases to give accurate results. In response to this, advanced N-body force-fields were developed to model the forces. In the present study we use Vashishta *et al.* potential for alumina, given by:

$$V_{net} = \sum_{i < j} V_{ij}^{(2)}(r_{ij}) + \sum_{i, j < k} V_{ijk}^{(3)}(r_{ij}, r_{ik}). \quad (2.19)$$

The two-body interaction term can be expressed as:

$$V_{ij}^{(2, shifted)}(r) = \begin{cases} \frac{H_{ij}}{r^{\eta_{ij}}} + \frac{Z_i Z_j}{r} e^{-\frac{r}{\lambda}} - \frac{D_{ij}}{2r^4} e^{-\frac{r}{\xi}} - \frac{W_{ij}}{r^6}, & r \leq r_c, \\ 0, & r > r_c. \end{cases} \quad (2.20)$$

The two-body term includes steric-size effects, coulomb interactions, charge-induced dipole, and van der Waals interactions. The three-body term includes the product of spatial dependent factor dependent factor and angular dependent factor to describe bond-bending and bond-stretching characteristics.

$$V_{ijk}^{(3)}(r_{ij}, r_{ik}) = R^{(3)}(r_{ij}, r_{ik}) P^{(3)}(\theta_{jik}) \quad (2.21)$$

$$R^{(3)}(r_{ij}, r_{ik}) = B_{jik} \exp\left(\frac{\gamma}{r_{ij} - r_0} + \frac{\gamma}{r_{ik} - r_0}\right) \Theta(r_0 - r_{ij}) \Theta(r_0 - r_{ik}), \quad (2.22)$$

$$P^{(3)}(\theta_{jik}) = \frac{(\cos \theta_{jik} - \cos \bar{\theta}_{jik})^2}{1 + C_{jik} (\cos \theta_{jik} - \cos \bar{\theta}_{jik})^2}. \quad (2.23)$$

Here B_{jik} is the strength of three-body interaction, θ_{jik} the angle formed by r_{ij} and r_{ik} , and $\Theta(r_0 - r_{ij})$ the step function. As mentioned in section 2.3.1.1, the Vashishta *et al.* potential is only used to model atomic interactions in Al_2O_3 nanoparticle suspended in water system. The following two sections describe the potential functions used for modeling Al and the Al/ Al_2O_3 interfaces respectively.

2.3.1.3 Embedded atom method (EAM) potential

For transition metals and metal-alloys, the embedded atom model (EAM) is a very common many-body potential used for its ability to electron cloud around nuclei [77]. The EAM potential takes the form:

$$V_i = F_\alpha \left(\sum_{j \neq i} \rho_\beta(r_{ij}) \right) + \frac{1}{2} \sum_{j \neq i} \phi_{\alpha\beta}(r_{ij}), \quad (2.24)$$

where ϕ is the pairwise potential energy, ρ_β is the contribution to the electronic charge density from atom j of type β at the location of atom i , and F is an embedding function that represents the energy required to place atom i of type α into the electron cloud. For a typical Al/Al₂O₃ interface structure used in Chapter 4, atomic interactions on the Al side need to be modeled by explicit inclusion of the effects of the electron cloud. Hence, EAM potential is used for this purpose. However, in order to model the interface, we also need to include the bonding characteristics, which is accomplished by using a charge-transfer interatomic potential such as the Streitz-Mintmire potential,[78] as described in the following section.

2.3.1.4 Streitz-Mintmire potential

To model material interfaces that involve charges, it is more convenient to employ a dynamic charge transfer interatomic potential. The Streitz-Mintmire (SM) potential is a more complicated variable charge interatomic potential designed specifically for Al/Al₂O₃ interface, which explicitly includes charge transfer between anions and cations in the material [78] during the formation of an interface. The SM potential has been used to

adequately describe the elastic properties, surface energies, and surface properties of sapphire in prior works [78]. We have also confirmed the suitability of using SM potential in predicting phonon properties by comparing with DFT-LD results for Al and Al₂O₃ crystals independently (shown in Appendix B). Therefore, SM potential is suitable for modeling interfacial phonon mediated heat transport. It involves an EAM potential coupled with a pairwise interaction. Characteristics of this potential are long range electrostatics and variable charges:

$$E_{es} = \sum_i E_i(q) + \frac{1}{2} \sum_{i \neq j} V_{ij}(r_{ij}, q_i, q_j). \quad (2.25)$$

Here, E_{es} represents the electrostatic energy of a set of interacting atoms with atomic charges q_i , which is given as the sum of atomic energies, E_i , and the electrostatic interaction energies between all pairs of atoms, V_{ij} . Expanding these terms, we get:

$$E_i(q) = E_i(0) + \chi_i q_i + \frac{1}{2} \eta_i q_i^2 \quad (2.26a)$$

$$V_{ij}(r_{ij}, q_i, q_j) = \int d^3 r_i \int d^3 r_j \cdot \rho_i(r_i, q_i) \cdot \rho_j(r_j, q_j) / r_{ij}, \quad (2.27b)$$

$$\rho_i(r_i, q_i) = Z_i \delta(r - r_i) + (q_i - Z_i) f_i(r - r_i)$$

where, λ is the electronegativity, Z is effective-core charge, and f describes the radial distribution of the valence charge in space.

Since we have discussed all the interatomic potential functions used in MD simulations, let us review the major time integration algorithms and the rationale behind choosing the right algorithm for the different MD simulations used in this research.

2.3.2 Time integration

Time integration is the engine of an MD simulation. Acceleration on each atom can be obtained from the forces, which may be integrated to get velocities of atoms, which when integrated give their new positions. New spatial positions give rise to a new set of atomic forces, and the iteration continues, so that one can track the time dependent positions and velocities of all the atoms, which is referred to as the trajectory. The sampling of the continuous trajectory in time continues until enough data is accumulated to calculate desired properties.

MD time integration algorithms are usually based on finite difference methods, where time is discretized on a finite grid. In these approaches, the distance between consecutive points on the grid is the time-step size, Δt and the time evolution of the system can be followed for long times by integrating over time steps. Two popular integration methods for MD calculations are the Verlet algorithm and predictor-corrector algorithms [79]. The Verlet algorithm has a truncation error $\sim O(\Delta t^4)$ for each integration time step, while the round-off errors decrease more slowly with decreasing Δt , and dominate in the small Δt limit. Therefore, it is important to choose the right time step size for MD simulations to ensure that these errors are sufficiently suppressed.

In this research, the Verlet algorithm is used, which involves the addition of two Taylor expansions in time, for the position of an individual atom $r(t)$. One expansion is forward in time, while the other is backwards in time. The scheme can be written as:

$$\begin{aligned} r(t + \Delta t) &= r(t) + v(t)\Delta t + (1/2)a(t)\Delta t^2 + (1/6)b(t)\Delta t^3 + O(\Delta t^4) \\ r(t - \Delta t) &= r(t) - v(t)\Delta t + (1/2)a(t)\Delta t^2 - (1/6)b(t)\Delta t^3 + O(\Delta t^4) \end{aligned} \quad (2.28)$$

Here r is the position vector, a is the acceleration, and b is the third derivatives of r with respect to t . Adding these two expressions result in,

$$r(t + \Delta t) = 2r(t) - r(t - \Delta t) + a(t)\Delta t^2 + O(\Delta t^4) \quad (2.29)$$

This is the basic form of Verlet algorithm. From this, the acceleration of an atom at time t can be calculated as:

$$a(t) = -(1/m)\nabla\phi(r(t)) \quad (2.30)$$

The velocities of atoms at time t can then be calculate from the expression:

$$v(t) = \frac{r(t + \Delta t) - r(t - \Delta t)}{2\Delta t} \quad (2.31)$$

Verlet algorithm was chosen over other time integration algorithms is because of its relatively high numerical stability in terms of largest allowable time step, which is especially useful when the processes in the system has an ample separation of time scales. In addition, Verlet algorithm also allows one to obtain at time $t + \Delta t$ rather than $t + \Delta t/2$ in other time integration schemes.

Now that we have discussed all the essential features required to get a typical MD simulation running and produce data, let us look at theoretical formulations that can be used to evaluate thermal transport properties in materials. The following section summarizes fluctuation-dissipation theorem and the Green-Kubo relations for thermal conductivity.

2.3.3 *Fluctuation dissipation theorem: Green-Kubo relations*

Equilibrium MD (EMD) and non-equilibrium MD (NEMD) are the two commonly used techniques to predict thermal conductivity. In NEMD, thermal conductivity is determined using Fourier's law of heat conduction [7], wherein a heat flux is imposed on the system and the resulting temperature gradient is calculated; the reverse can also be done, by calculating a heat flux from an imposed temperature gradient. In either case, when small nanometer size supercells are used or temperature differences greater than ~ 10 K are observed/imposed, the result is extremely high heat fluxes that often exceed what is observed terrestrially and/or non-linear temperature profiles. Size effects may also be present, as the system must be large enough, in the case of solids, to contain long wavelength and long mean-free-path (MFP) phonons [8]. This is because the artificially imposed boundary conditions used to impart the heat flux tend to perturb the atom's natural motions, and consequently they artificially "scatter" phonons.

In EMD, the system is in equilibrium throughout the simulation. EMD is sometimes preferred over NEMD, owing to its lesser size-dependency for solids. The system size should be large enough to include all the necessary wavelengths, but not necessarily the MFPs [7, 9, 10], as periodic boundary conditions (PBC) allow phonons to propagate past the boundaries and re-enter through the opposite face without being scattered. EMD can be combined with the fluctuation-dissipation theorem to calculate thermal conductivity [80]. Here, the linear response of the system to a small thermal perturbation is determined from the time history of the equilibrium fluctuations of the volume averaged heat flux. The thermal conductivity, k , is given by the Green-Kubo (GK) relation as,

$$k = \frac{1}{k_B T^2} \int_0^\infty \langle \vec{S}(t) \cdot \vec{S}(0) \rangle dt, \quad (2.32)$$

where the heat current vector S was derived by Hardy [81] as:

$$S = \frac{1}{V} \left\{ \sum_i \frac{\vec{p}_i}{m_i} \left(\frac{p_i^2}{2m_i} + \phi_i \right) + \sum_i \sum_j \left(\frac{\partial \phi_{ij}}{\partial r_i} \cdot \vec{v}_i \right) \vec{r}_{ij} \right\}, \quad (2.33)$$

where V is the volume of the system, T the equilibrium temperature, k_B the Boltzmann constant, p the momentum, v the velocity, and r the position, m the mass, ϕ the potential energy, and summation is over atoms denoted by i . The term in angular brackets represents the heat current autocorrelation function (HCACF). In Eq. 2.33, the first term is the convective term and the second is the virial term. In the GK formulation, thermal conductivity depends on the time taken for fluctuations to lose correlation with their original values. Studies have shown that fluctuations in crystalline materials are correlated for a longer time, resulting in higher thermal conductivity [82, 83]. Conversely, fluctuations lose correlation quickly in amorphous materials and liquids [84].

For homogeneous systems, Eq. 2.33 is sufficient to represent the heat current. However, for multicomponent systems, self-diffusion of species is possible. In order to account for it, the convective term may be corrected with the partial enthalpy, [56] h_e of each species a :

$$S_{conv} = \frac{1}{V} \left[\sum_{i=1}^N \frac{\vec{p}_i}{m_i} \left(\frac{p_i^2}{2m_i} + U_i \right) - \sum_{a=1}^n h_{e,a} \sum_{i=1}^{N_a} \vec{v}_{a,i} \right]. \quad (2.34)$$

From thermodynamics, enthalpy $H = E + PV$. This can be expressed statistically as:

$$h_{e,a} = \frac{\sum_{i=1}^{N_a} \left[K_i + V_i + \frac{1}{3} \left(m_i \vec{v}_i^2 + \frac{1}{2} \sum_{j=1}^N \vec{r}_{ij} \cdot \vec{F}_{ij} \right) \right]}{N_a} \quad (2.35)$$

where the sum of the first two terms corresponds to the total energy E , which is the sum of time-averaged kinetic energy, K_i and potential energy, V_i of particles of species, a . The terms in the brackets represent the PV term, which includes the kinetic and virial terms. It was shown by Babaei et al. [43] that the properties of multicomponent systems are sensitive to a non-zero h_e , which if not subtracted from convective heat flux can reflect in HCACF, which when integrated, results in anomalous thermal conductivity values.

In summary, GK relations when used in conjunction with EMD can help us gain a quantitative and qualitative understanding of the thermal conductivity of various materials. Now let us review a similar treatment for TIC based on the fluctuation-dissipation theorem. MD, when combined with the vibrational modal information has the potential to gain mode-level information on the TIC. Modal information can be gained from lattice dynamics (LD) calculations.[74, 85-88] Therefore, before getting into the nuances of such formulations, it is important to have some fundamental understanding on the LD formulation.

2.4 Lattice Dynamics (LD)

In addition to using MD, LD is also used in this research to determine the vibrational properties of the lattice. Specifically, LD can be used to evaluate the phonon thermal conductivity, phonon DOS, and polarization vectors of crystal structures. LD is a

generalized formulation that can provide a clearer picture into the spectral characteristics of phonons. To describe the formulation, a simple one-dimensional chain is considered as an example and then we move to a more general formulation involving the solution of an eigenvalue problem.

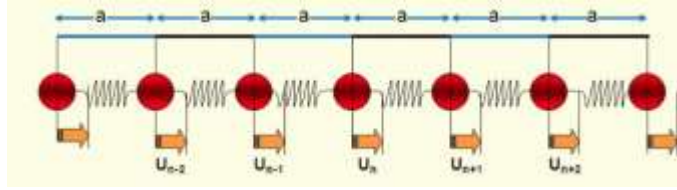


Figure 2.2. One-dimensional bead-spring chain representing atomic arrangement in a crystal

Consider the one-dimensional chain of atoms in Figure 2.2. This is a bead-spring model where every atom is connected with a spring to two neighboring atoms on either side. Hence, the equation of motion for the n^{th} atom in the chain is a discretized version of the wave equation:

$$m_n \cdot \frac{d^2 u_n}{dt^2} = K(u_{n+1} - u_n) - K(u_n - u_{n-1}) \Rightarrow m_n \cdot \frac{\partial^2 u_n}{\partial t^2} = K a^2 \frac{\partial^2 u_n}{\partial x^2}, \quad (2.36)$$

where u_k is the displacement from equilibrium, the subscript n denotes its position in the

chain, K is the spring constant, $\frac{\partial^2 u_n}{\partial t^2}$ is the acceleration and m is the mass of the atom.

Assuming infinite length for the chain and taking the continuum limit, solution to u_n can be denoted by a series of plane waves as:

$$u_n = A \cdot \exp(-i \cdot (\omega \cdot t - k \cdot n \cdot a)), \quad (2.37)$$

where k is a wavevector equal to $\frac{2\pi}{\lambda}$, where λ is a wavelength corresponding to the wave's spatial periodicity and ω is the vibrational frequency. Plugging the solution back into Eq. 2.37, we get the mode frequencies as a function of wave vector, or dispersion relation, as:

$$\omega = 2\sqrt{\frac{K}{m}} \left| \sin\left(\frac{k.a}{2}\right) \right|. \quad (2.38)$$

This can be generalized to three dimensions. Rewriting 2.38 in matrix form for a single term in the infinite series plane wave solution, we get:

$$\omega^2(\mathbf{k}, \nu) \mathbf{e}(\mathbf{k}, \nu) = \mathbf{D}(\mathbf{k}) \mathbf{e}(\mathbf{k}, \nu), \quad (2.39)$$

where $\mathbf{e}(\mathbf{k}, \nu)$ is a complex vector representing the polarization direction for the mode and $\mathbf{D}(\mathbf{k})$ is the dynamical matrix containing the mass and stiffness information related to a particular propagation direction. The elements of the dynamical matrix are generalized for more than one basis atom.

2.4.1 Calculation of interatomic force constants and phonon properties

We start by evaluating the interatomic force constants (IFC) by LD calculations, which can be used to analyze phonon properties. The potential energy of interacting atoms must be approximated via Taylor expansion as a function of atomic displacement with respect to equilibrium potential energy as:

$$\begin{aligned}
U - U_0 &= \sum_{n=1}^N U_n = U_1 + U_2 + U_3 + \dots, \\
U_n &= \frac{1}{n!} \sum_{\substack{\ell_1 \kappa_1, \dots, \ell_n \kappa_n \\ \mu_1, \dots, \mu_n}} \Phi_{\mu_1 \dots \mu_n}(\ell_1 \kappa_1; \dots; \ell_n \kappa_n) u_{\mu_1}(\ell_1 \kappa_1) \dots u_{\mu_n}(\ell_n \kappa_n).
\end{aligned} \tag{2.40}$$

Here, $u_{\mu}(\ell \kappa)$ is the atomic displacement of the κ^{th} atom in the l^{th} unit cell along the μ^{th} direction, and $\Phi_{\mu_1 \dots \mu_n}(\ell_1 \kappa_1; \dots; \ell_n \kappa_n)$ is the n^{th} order IFC. Therefore, a ‘model’ force $F_{i,t}^{LD}$ can be obtained as a linear function of IFC’s by differentiating U with respect to u_i , where $i = (\ell, \kappa, \mu)$ is the coordinate triplet. The objective is to find the right set of IFC’s so that the $F_{i,t}^{LD}$ is the best approximation of $F_{i,t}^{DFT}$ i.e. forces obtained from first principles calculations. This can be performed by a least-squares fitting strategy:

$$\text{minimize } \chi^2 = \sum_t^m \sum_i \| F_{i,t}^{DFT} - F_{i,t}^{LD} \|^2. \tag{2.41}$$

Here, χ^2 is the squared error in forces or the residual of fit summed over m distinct atomic configurations. The fit can be evaluated by σ defined as:

$$\sigma = \sqrt{\frac{\chi^2}{\sum_t^m \sum_i (F_{i,t}^{DFT})^2}} \tag{2.42}$$

The interatomic force constants can be then used to calculate the phonon dynamical matrix given by:

$$D_{\mu\nu}(\kappa\kappa'; \mathbf{q}) = \frac{1}{\sqrt{M_{\kappa} M_{\kappa'}}} \sum_{\ell'} \Phi_{\mu\nu}(\ell\kappa; \ell'\kappa') \exp[i\mathbf{q} \cdot (\mathbf{r}(\ell') - \mathbf{r}(\ell))], \tag{2.43}$$

where M_κ is the atomic mass of atom κ , and \mathbf{q} represents the coordinate vector in reciprocal space. For example, the reciprocal space can be discretized by $q \times q \times q$ wave vector grids. Numerical value of q determines the coarseness/fineness of the grid space i.e. if the numerical value of q is low, the grid is coarse whereas a large value of q corresponds to a fine grid. Number of q points have to be chosen based on a tradeoff between computational costs and accuracy requirements for the properties to be calculated.

By diagonalizing the dynamical matrix, the eigenvalues $\omega_{\mathbf{q}j}^2$ ($j = 1, 2, \dots, m$) and corresponding eigenvectors $\mathbf{e}_{\mathbf{q}j}$ for each \mathbf{q} point can be obtained, where $\mathbf{e}_{\mathbf{q}j}$ is a column vector consisting of atomic polarization $e_\mu(\kappa; \mathbf{q}j)$. Most importantly, note that the number of eigenvectors, $m = 3N_\kappa$. Now, eigenvalues can be written as:

$$\omega_{\mathbf{q}j}^2 = (\mathbf{e}_{\mathbf{q}j}^*)^T D(\mathbf{q}) \mathbf{e}_{\mathbf{q}j}. \quad (2.44)$$

From the information available, several properties of phonons can be extracted. The following sections review the various phonon properties and how to formulate them mathematically.

2.4.2 Group velocity of phonons

The first important property to be evaluated is the phonon group velocity. It is the speed of propagation of an acoustic phonon, which is also the speed of sound in the lattice. The group velocity of the phonon mode $\mathbf{q}j$ can be given as:

$$\mathbf{v}_{\mathbf{q}j} = \frac{\partial \omega_{\mathbf{q}j}}{\partial \mathbf{q}}. \quad (2.45)$$

Numerically, this can be evaluated using a central difference scheme in the \mathbf{q} -point space, as:

$$\mathbf{v}_{\mathbf{q}j} \approx \frac{\omega_{\mathbf{q}+\Delta\mathbf{q}j} - \omega_{\mathbf{q}-\Delta\mathbf{q}j}}{2\Delta\mathbf{q}}. \quad (2.46)$$

2.4.3 Phonon density of states (DOS)

Phonon density of states (DOS) is another important property that can be studied using LD calculations. DOS represents the number of phonons per interval of energy (or frequency) available to be occupied. The one-phonon DOS is given by:

$$\text{DOS}(\omega) = \frac{1}{N_q} \sum_{\mathbf{q}, j} \delta(\omega - \omega_{\mathbf{q}j}). \quad (2.47)$$

The two-phonon DOS is given by:

$$\text{DOS2}(\omega; \mathbf{q}; \pm) = \frac{1}{N_q} \sum_{\mathbf{q}_1, \mathbf{q}_2, j_1, j_2} \delta(\omega \pm \omega_{\mathbf{q}_1 j_1} - \omega_{\mathbf{q}_2 j_2}) \delta_{\mathbf{q} \pm \mathbf{q}_1, \mathbf{q}_2 + \mathbf{G}}, \quad (2.48)$$

where \mathbf{G} is a reciprocal lattice vector. The sign \pm represents absorption and emission processes respectively, and δ represents the delta function. Phonon DOS can be usually evaluated fairly accurately from a coarse phonon wave vector grid. [50] For instance, prior

calculations[50] based on a q-point convergence test show that a relatively coarse 4x4x4 grid space can give a reasonably accurate prediction of DOS.

2.4.4 Phonon thermal conductivity

Finally, the most important property: phonon thermal conductivity can be evaluated by solving the phonon Boltzmann transport equation (BTE) given by:

$$\frac{\partial f}{\partial t} + \mathbf{v} \cdot \vec{\nabla}_{\mathbf{q}} f + \frac{\mathbf{F}}{m} \cdot \vec{\nabla}_{\mathbf{v}} f = \frac{f - f_0(E, T)}{\tau(\mathbf{q}, \mathbf{k})}, \quad (2.49)$$

where \mathbf{v} is velocity, \mathbf{F} is external force acting on the phonons, and $\frac{\mathbf{F}}{m}$ is the acceleration

and the symbols $\vec{\nabla}_{\mathbf{q}}$ and $\vec{\nabla}_{\mathbf{v}}$ denote gradients with respect to position and velocity

respectively. The phonon thermal conductivity, $k_{\text{ph}}^{\mu\nu}(T)$ can be calculated by solving the phonon BTE under relaxation time approximation (RTA) giving the following expression:

$$k_{\text{ph}}^{\mu\nu}(T) = \frac{1}{\Omega N_q} \sum_{\mathbf{q}, j} c_{\mathbf{q}j}(T) v_{\mathbf{q}j}^{\mu} v_{\mathbf{q}j}^{\nu} \tau_{\mathbf{q}j}(T), \quad (2.50)$$

where $c_{\mathbf{q}j} = \hbar \omega_{\mathbf{q}j} \partial n_{\mathbf{q}j} / \partial T$ and $\tau_{\mathbf{q}j}(T)$ is the phonon lifetime. The phonon lifetime can be approximated by the Mattheissen's rule as:

$$\tau_{\mathbf{q}j}^{-1}(T) = 2(\Gamma_{\mathbf{q}j}^{\text{anh}}(T) + \Gamma_{\mathbf{q}j}^{\text{iso}}). \quad (2.51)$$

where Γ is the phonon line-width. The superscripts *anh* and *iso* denote anharmonic and isotopic respectively. $\Gamma_{\mathbf{q}j}^{\text{anh}}$ can be calculated as:

$$\begin{aligned} \Gamma_{\mathbf{q}j}^{\text{anh}}(\omega) = & \frac{\pi}{2\hbar^2} \sum_{\mathbf{q}_1, \mathbf{q}_2} \sum_{j_1, j_2} |V_{-\mathbf{q}, \mathbf{q}_1 j_1, \mathbf{q}_2 j_2}^{(3)}|^2 \times \\ & \left[-(n_1 + n_2 + 1)\delta(\omega + \omega_1 + \omega_2) + (n_1 + n_2 + 1)\delta(\omega - \omega_1 - \omega_2) \right. \\ & \left. -(n_1 - n_2)\delta(\omega - \omega_1 + \omega_2) + (n_1 - n_2)\delta(\omega + \omega_1 - \omega_2) \right]. \end{aligned} \quad (2.52)$$

where, $n(\omega) = \frac{1}{e^{\hbar\omega/k_B T} - 1}$ is the Bose-Einstein distribution for phonons, and V is the matrix

element of the cubic Hamiltonian between the different eigen states.[89].

$\Gamma_{\mathbf{q}j}^{\text{iso}}$ can be calculated as:

$$\Gamma_{\mathbf{q}j}^{\text{iso}}(\omega) = \frac{\pi}{4N_q} \omega_{\mathbf{q}j}^2 \sum_{\mathbf{q}_1, j_1} \delta(\omega - \omega_{\mathbf{q}_1 j_1}) \sum_{\kappa} g_2(\kappa) |\mathbf{e}^*(\kappa; \mathbf{q}_1 \mathbf{j}_1) \cdot \mathbf{e}(\kappa; \mathbf{q} \mathbf{j})|^2, \quad (2.53)$$

where g_2 is a dimensionless factor given by $g_2(\kappa) = \sum_i f_i(\kappa) \left(1 - \frac{m_i(\kappa)}{M_\kappa}\right)^2$, f_i is the fraction of the i^{th} isotope of an element having mass m_i , and M_κ is the average mass of the system.

Phonon wave vector grid requirements for evaluating thermal conductivity is higher than that of DOS. Prior studies have shown that a fine 28x28x28 grid space is required to obtain a converged value of phonon thermal conductivity of metals and semiconductors.[50] Furthermore, the phonon thermal conductivity spectra $k_{\text{ph}}^{\mu\mu}(\omega)$ can also be calculated as:

$$k_{\text{ph}}^{\mu\mu}(\omega) = \frac{1}{\Omega N_q} \sum_{\mathbf{q},j} c_{\mathbf{q}j} v_{\mathbf{q}j}^{\mu} v_{\mathbf{q}j}^{\mu} \tau_{\mathbf{q}j} \delta(\omega - \omega_{\mathbf{q}j}). \quad (2.54)$$

When spectral thermal conductivity is integrated over the phonon frequency, we get the

total phonon thermal conductivity: $k_{\text{ph}}^{\mu\mu} = \int_0^{\infty} \kappa_{\text{ph}}^{\mu\mu}(\omega) d\omega$, where

$$k_{\text{ph}}^{\mu\mu}(\omega) = \frac{1}{\Omega N_q} \sum_{\mathbf{q},j} c_{\mathbf{q}j} v_{\mathbf{q}j}^{\mu} v_{\mathbf{q}j}^{\mu} \tau_{\mathbf{q}j} \delta(\omega - \omega_{\mathbf{q}j}). \quad (2.55)$$

Thermal conductivity accumulation is an important property that can be studied using LD calculations. This can be given as:

$$k_{\text{ph,acc}}^{\mu\mu}(L) = \frac{1}{\Omega N_q} \sum_{\mathbf{q},j} c_{\mathbf{q}j} v_{\mathbf{q}j}^{\mu} v_{\mathbf{q}j}^{\mu} \tau_{\mathbf{q}j} \Theta(L - |\mathbf{v}_{\mathbf{q}j}| \tau_{\mathbf{q}j}), \quad (2.56)$$

where $\Theta(x)$ is the step function, and $|\mathbf{v}_{\mathbf{q}j}| \tau_{\mathbf{q}j}$ represents the phonon MFP. Now that we have discussed the necessary equations and solution methods to investigate phonon properties of pure crystal, let us look at a method to investigate interfacial conductance that is based on MD and LD.

We are now in a position to combine LD with MD to perform modal analysis of TIC. By solving the eigenvalue problem shown in Eq. 2.44, we can obtain the complete eigenvector basis set of the vibrational modes in an interface structure. This eigenvector basis set can be supplemented with an MD simulation to decompose interfacial heat transport properties across the eigen modes. The following section reviews a mathematical formulation for TIC. Firstly, a mathematical formulation for total TIC value based on

fluctuation-dissipation theorem is discussed. Following that, formulation for the modal decomposition is also reviewed.

2.5 Interfacial Conductance Modal Analysis (ICMA)

2.5.1 Total conductance

Interfacial conductance modal analysis (ICMA) is a hybrid of LD and MD. It combines an eigenmode decomposition method by McGaughey and Kaviani [90] with equilibrium molecular dynamics (EMD) conductance expression derived by Barrat et al. [91] and Domingues et al. [92]. As the name suggests, it gives eigenmode level details on interfacial conductance, and can be used to study the effects of anaharmonic effects and the effect of stress, defects, functionalization, etc. on interfacial conductance.

Consider a system of two materials A and B consisting of N_A and N_B atoms respectively where these atoms vibrate about their equilibrium positions. When these two materials are brought together to form an interface, within the harmonic limit, $3(N_A + N_B)$ eigen solutions can be obtained from lattice dynamics calculations. The atomic displacements and velocities can be expressed in terms of these eigen modes as:

$$\mathbf{x}_i = \sum_n \frac{1}{(Nm_i)^{1/2}} \mathbf{e}_{n,i} X_n \quad (2.57)$$

$$\dot{\mathbf{x}}_i = \sum_n \frac{1}{(Nm_i)^{1/2}} \mathbf{e}_{n,i} \dot{X}_n . \quad (2.58)$$

Here the summations are made over the n eigenmodes, and \mathbf{x}_i , $\dot{\mathbf{x}}_i$, m_i are the displacement from equilibrium, velocity, and mass of atom i respectively. The symbol $\mathbf{e}_{n,i}$ is the eigenvector with atom i . The normal mode coordinates for position and velocity of the n th mode are given respectively by X_n and \dot{X}_n . By inverting eqns. 2.57 and 2.58, we obtain

$$X_n = \sum_i \frac{m_i^{1/2}}{N^{1/2}} \mathbf{x}_i \cdot \mathbf{e}_{n,i}^* \quad (2.59)$$

$$\dot{X}_n = \sum_i \frac{m_i^{1/2}}{N^{1/2}} \dot{\mathbf{x}}_i \cdot \mathbf{e}_{n,i}^* \quad (2.60)$$

Now the summation is over atoms i , and the $*$ denotes complex conjugate of eigenvector.

Following the approach of Barrat et al. [91] and Domingues et al. [92], the instantaneous heat flow across the interface can be given as follows. In a microcanonical ensemble, the rate at which energy transmitted across the boundaries of material A is equal to the rate of change of energy in material B , at any instant. Hence from statistical mechanics, the Hamiltonian of such a system is:

$$H = \sum_i^N \frac{\mathbf{p}_i^2}{2m_i} + \Phi(\mathbf{r}_1, \mathbf{r}_2, \dots, \mathbf{r}_n). \quad (2.61)$$

Consequently, the Hamiltonian of an individual atom is:

$$H_i = \frac{\mathbf{p}_i^2}{2m_i} + \Phi_i(\mathbf{r}_1, \mathbf{r}_2, \dots, \mathbf{r}_n). \quad (2.62)$$

From Eqn. 2.61 and 2.62, the instantaneous energy transfer across the interface of A and B can be expressed as

$$Q_{A \rightarrow B} = - \sum_{i \in A} \sum_{j \in B} \left\{ \frac{p_{i,\alpha}}{m_i} \left(\frac{-\partial H_j}{\partial \mathbf{r}_i} \right) + \frac{p_{j,\alpha}}{m_j} \left(\frac{\partial H_i}{\partial \mathbf{r}_j} \right) \right\} \quad (2.63)$$

For a system with only pairwise interactions, this reduces to

$$Q_{A \rightarrow B} = -\frac{1}{2} \sum_{i \in A} \sum_{j \in B} \mathbf{f}_{ij} \cdot (\dot{\mathbf{x}}_i + \dot{\mathbf{x}}_j) \quad (2.64)$$

From this relation, using the fluctuation-dissipation theorem, the conductance can be calculated via correlation in the equilibrium fluctuations of the heat flow as:

$$Q_{A \rightarrow B} = -\frac{1}{2} \sum_{i \in A} \sum_{j \in B} \mathbf{f}_{ij} \cdot (\dot{\mathbf{x}}_i + \dot{\mathbf{x}}_j) \quad (2.65)$$

Eq. 2.65 gives the total thermal conductance of the interface.

2.5.2 Modal decomposition

The total heat flow across the interface can be given as the sum of modal heat flow:

$$Q = \sum_n Q_n . \quad (2.66)$$

Therefore, G can be rewritten as:

$$G = \frac{1}{Ak_B T^2} \int \left\langle \sum_n Q_n(t) \cdot Q(0) \right\rangle dt = \sum_n \frac{1}{Ak_B T^2} \int \langle Q_n(t) \cdot Q(0) \rangle dt . \quad (2.67)$$

This gives the contribution from each mode as:

$$G_n = \frac{1}{Ak_B T^2} \int \langle Q_n(t) \cdot Q(0) \rangle dt , \quad (2.68)$$

resulting in:

$$G = \sum_n G_n \quad (2.69)$$

The total G can be again written from mode-mode correlation of heat current as:

$$G = \frac{1}{Ak_B T^2} \int \left\langle \sum_n \mathcal{Q}_n(t) \cdot \sum_{n'} \mathcal{Q}_{n'}(t) \right\rangle dt = \sum_n \sum_{n'} \frac{1}{Ak_B T^2} \int \langle \mathcal{Q}_n(t) \cdot \mathcal{Q}_{n'}(0) \rangle dt \quad (2.70)$$

with individual contributions from correlations between pairs of modes equal to

$$G_{n,n'} = \frac{1}{Ak_B T^2} \int \langle \mathcal{Q}_n(t) \cdot \mathcal{Q}_{n'}(0) \rangle dt. \quad (2.71)$$

In Eq. 2.71, by replacing the velocity of each atom with the sum of modal contributions, we can obtain the modal heat \mathcal{Q}_n as:

$$\mathcal{Q} = \sum_{i \in A} \sum_{j \in B} \left\{ \left(\sum_n \frac{1}{(Nm_i)^{1/2}} \mathbf{e}_{n,i} \dot{X}_n \right) \left(\frac{\partial H_j}{\partial \mathbf{r}_i} \right) - \left(\sum_n \frac{1}{(Nm_j)^{1/2}} \mathbf{e}_{n,j} \dot{X}_n \right) \left(\frac{\partial H_i}{\partial \mathbf{r}_j} \right) \right\} \quad (2.72)$$

$$\mathcal{Q}_n = \frac{1}{N^{1/2}} \sum_{i \in A} \sum_{j \in B} \left\{ \left(\frac{1}{(m_i)^{1/2}} \mathbf{e}_{n,i} \dot{X}_n \right) \left(\frac{\partial H_j}{\partial \mathbf{r}_i} \right) + \left(\frac{1}{(m_j)^{1/2}} \mathbf{e}_{n,j} \dot{X}_n \right) \left(\frac{-\partial H_i}{\partial \mathbf{r}_j} \right) \right\} \quad (2.73)$$

For pairwise interactions, this simplifies to:

$$\mathcal{Q}_n = \sum_{i \in A} \sum_{j \in B} \frac{-\mathbf{f}_{ij}}{2} \cdot \left(\frac{1}{(Nm_i)^{1/2}} \mathbf{e}_{n,i} \dot{X}_n + \frac{1}{(Nm_j)^{1/2}} \mathbf{e}_{n,j} \dot{X}_n \right) \quad (2.74)$$

The aim of this research is to choose an appropriate MD framework to simulate the interface, and in combination with a complete eigenvector basis set, use it in ICMA framework to obtain modal conductance contribution. Further analysis can be performed on mode-mode correlations to analyze its contribution to net conductance.

Now that we have discussed methods to quantify size-affected and temperature dependent thermal conductivity of Al and Al₂O₃ crystals, as well as the temperature dependent TIC values of the Al/Al₂O₃ interface, we will discuss methods to model nanoparticle thermal conductivity and the effective thermal conductivity of nanosuspensions.

2.6 Effective thermal conductivity model of heterogeneous propellant

The inputs of an effective thermal conductivity model for a mixture of solid and fluid are the particle thermal conductivity (k_p), fluid thermal conductivity (k_f), and the particle volume fraction, ϕ . In order to evaluate k_p , let us first consider a series circuit model representing the interface of Al and Al_2O_3 as shown in Figure 1.11 and the following treatment may be used.

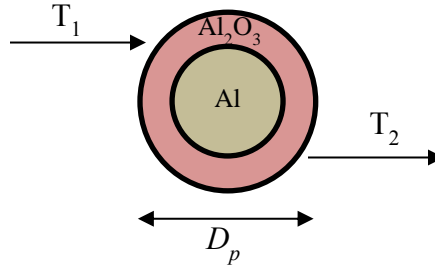


Figure 2.3 Schematic diagram of the core-shell particle model for evaluating the effective thermal conductivity of a nanoparticle

The thermal conductivity of a passivated nAl particle of total diameter D_p represented by a core-shell particle model as illustrated in Figure 2.3 was obtained as:

$$k_p = \frac{D_p}{\left(2 \cdot \frac{L_{\text{Al}_2\text{O}_3}}{k_{\text{Al}_2\text{O}_3}} + \frac{L_{\text{Al}}}{k_{\text{Al}}} + \frac{2}{G} \right)}. \quad (2.75)$$

Now that we obtained k_p , the next step is to model the effective thermal conductivity of the mixture, k_m . There are several effective thermal conductivity models for nanoparticle suspensions [52, 93, 94]. Some of them are based on *dynamic* heat conduction mechanisms [36] in nanofluids, namely base-fluid nanolayering and Brownian motion. In a recent study on thermal conductivity of nano-suspensions, Muraleedharan et al. [95] conducted MD

simulations in combination with fluctuation-dissipation theorem to rigorously show that nanolayering and Brownian motion have negligible contribution on the effective thermal conductivity of a mixture. Therefore, in this work, we have neglected these effects. Two other important factors to be considered in modeling k_m of a dense suspension are the random particle distribution and the viscous interaction between nanoparticles. Maxwell-Eucken [28, 29, 96] effective medium theory properly accounts for the random distribution of particles, and provides the following expression for the mixture thermal conductivity:

$$k_m = \frac{\phi_f k_f + \phi_p k_p \left(\frac{3k_f}{2k_f + k_p} \right)}{\phi_f + \phi_p \left(\frac{3k_f}{2k_f + k_p} \right)}. \quad (2.76)$$

Here ϕ is the volume fraction, subscripts f and p denote fluid and particle respectively. Interaction between particles is also important in capturing the viscous effects in the system, and can be addressed by using the Bruggeman effective medium theory, [30] which gives:

$$\phi_p \left(\frac{k_p - k_m}{k_p + 2k_m} \right) + \phi_f \left(\frac{k_f - k_m}{k_f + 2k_m} \right) = 0 \quad (2.77)$$

Therefore, in order to include both these effects, it is desirable to unify the Maxwell-Eucken and Bruggeman theories yielding effective thermal conductivity of the mixture, k_m as:

$$k_m = \frac{D + \sqrt{D^2 + 2k_p k_f}}{2}, \quad (2.78)$$

where,

$$D = (2k_p - k_f)\Phi_p(1 - \alpha_p) + (2k_f - k_p)\Phi_f \left(\frac{2\Phi_f + 2\Phi_p\alpha_p - 1}{2\Phi_f} \right). \quad (2.79)$$

Here α_p is the volume fraction of particle in a mixture with a Maxwell-Eucken structure.[29] The value of α_p is chosen to be 0.5 so as to conform to the condition that for

$$\Phi_p \rightarrow 1, k_m \rightarrow k_p$$

Now that we have discussed a mathematical modeling strategy for the effective thermal conductivity of nanosuspensions, we can use this model in conjunction with an independent chemical kinetics model to study flame propagation in a real combustion system. The following section introduces the mesoscale one-dimensional flame propagation model that can be used to study the flame properties. Detailed description of the numerical methods are given in Chapter 6 of the dissertation.

2.7 1-Dimensional flame propagation model

2.7.1 Physical system

For simplicity, a steady, one-dimensional, isobaric downward propagating flame in a chemically reacting system of fuel nanoparticles dispersed in liquid oxidizer is considered. This system ensures that the effect of thermal conduction can be studied without compromising on other phenomena that can occur in a real physical combustion system. Availability of experimental data ensures validation of results. Flame propagation

is modeled as a propagation of a thermal conduction wave, accompanied by a variety of physical and chemical processes, including vaporization of oxidizer, chemical reactions, and mass, momentum and energy exchanges between the fluid and particle phases. The system is approximated to be pseudo-homogenous. This contrasts with a completely heterogeneous system but ensures that the particles are in local thermal equilibrium with the surrounding fluid.

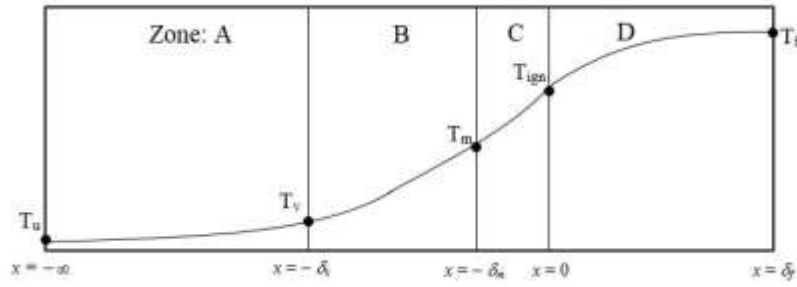


Figure 2.4. Physical model and multi-zone theoretical framework.

Figure 2.4 represents the physical model and the multizone flame structure used in the present study. Initially, the system is at an ambient temperature of 298 K. Liquid oxidizer undergoes a thermodynamic phase transition at the vaporization front which may for simplicity be treated as an infinitesimal plane at $x = -\delta_v$ at temperature T_v . At $x = -\delta_m$, Al core undergoes melting. Region encompassing $x = -\delta_v$ to $x = 0$ has higher temperature gradient, and marks the zone for an overall ignition of the suspension when an ignition temperature, T_{ign} , is attained. Chemical reactions are negligible in the preheat zones. In the gas-phase reaction zone, the temperature of products continues to increase up to the flame temperature of T_f . The flame continues propagating into the unburned suspension by conduction of heat and radicals.

The temperature profile and zone thicknesses can be obtained by solving the energy equation in each zone and matching the physical conditions at the boundaries. The general equation of energy balance can be given as:

$$\frac{\partial}{\partial t}(\rho C_p T) = \frac{\partial}{\partial x} \left(k \frac{\partial T}{\partial x} \right) + \dot{Q} \quad (2.80)$$

Where, ρ is the density, C_p is the specific heat, T is the temperature, k is the effective thermal conductivity, \dot{Q} is the heat release rate (source term) which is inversely proportional to mean particle burning time, τ_b . τ_b has to be independently evaluated and input using particle burning time models that are benchmarked with experimental measurements or first principle calculations. In the constant linear burning rate assumption, the partial time derivative, $\frac{\partial}{\partial t}$ can be written as $r_b \frac{d}{dx}$ under the assumption that the steady state burning rate is constant, and equation 2.88 can be rewritten as:

$$r_b \frac{d}{dx}(\rho C_p T) = \frac{\partial}{\partial x} \left(k \frac{\partial T}{\partial x} \right) + \dot{Q} \quad (2.81)$$

Note that the physical properties ρ and C_p are function of temperature only. Thermal conductivity k , on the other hand, is a function of temperature as well as local mixture composition.

The linear burning rate (or flame speed) r_b is to be evaluated by the shooting method. The first step is to assume r_b . Disregarding the source term and expanding the RHS of the Eq. 2.89, we have

$$r_b \frac{d}{dx}(\rho C_p T) = \frac{dk}{dx} \left(\frac{\partial T}{\partial x} \right) + k \frac{d^2 T}{dx^2} \quad (2.82)$$

Eq. 2.82 can be discretized by one-dimensional finite difference method

$$r_b \frac{(\rho C_p T)_{i+1} - (\rho C_p T)_{i-1}}{2\Delta x} = \frac{k_{i+1} - k_{i-1}}{2\Delta x} \cdot \frac{T_{i+1} - T_{i-1}}{2\Delta x} + k_i \frac{T_{i+1} - 2T_i + T_{i-1}}{(\Delta x)^2} \quad (2.83)$$

and solved using Gauss-Seidel iteration:

$$T_i^{n+1} = \frac{(\Delta x)^2}{2k_i} \left[\frac{k_{i+1}^n - k_{i-1}^n}{2\Delta x} \cdot \frac{T_{i+1}^n - T_{i-1}^n}{2\Delta x} + k_i \frac{T_{i+1}^n + T_{i-1}^n}{(\Delta x)^2} - r_b \frac{(\rho C_p T)_{i+1}^n - (\rho C_p T)_{i-1}^n}{2\Delta x} \right] \quad (2.84)$$

where i is the grid point in the one-dimensional stencil consisting of r grid points, and n denotes the number of iteration. Note that the number of grid points should be chosen so as to include at the minimum, a full nanoparticle and the surrounding fluid medium so that it is representative of the mean mixture properties of the zone. If the grid size is smaller, then the effective thermal conductivity model fails for the control volume leading to the failure of iterative solution.

2.8 Conclusions

This chapter provided a high level introduction to the formulation of the computational approach used to understand the nanoscale heat transfer effects in the combustion of a nanoparticle suspension. Tools discussed in this chapter will be judiciously chosen and elaborated further to answer the different thesis questions in the following chapters one by one.

CHAPTER 3. PHONON TRANSPORT IN ALUMINUM AND ALUMINUM OXIDE

In this chapter, we try to answer the first thesis question: *How to investigate size effects on phonon thermal conductivity of Al and Al₂O₃ and how to quantify size effects?*

To answer this, we begin with the hypothesis that phonon transport properties can be investigated via first principle lattice dynamics (DFT-LD) calculations. It utilizes input from DFT calculations, and the output of LD is the set of IFC's, which can be used to analyze phonon properties. Firstly, the temperature dependent phonon thermal conductivity obtained from the solution of phonon BTE is presented, and the contribution from phonons with different mean free paths and frequencies are also discussed. From these values, the effect of particle size on phonon thermal conductivity is deduced and modeled mathematically. Other properties of phonons, namely, mean free path and lifetime as a function of frequency are also analyzed to obtain a holistic view of phonon transport in Al and Al₂O₃.

3.1 Introduction

The major carriers of heat in solids are electrons and phonons. In metals, due to the large density of free electrons, the primary heat carriers are electrons and consequently, the phonon contributions are comparatively very low. Jain and McGaughey [50] calculated the phonon contributions to thermal conductivity of Al via solution of the phonon BTE under RTA using inputs from DFT-LD calculations, considering phonon-phonon (p-p) and

electron-phonon (e-p) interactions to obtain phonon thermal conductivity. Their results show that the phonon thermal conductivity of Al at 300 K is only 7 W/m-K, which is only a very small fraction (~3%) the total thermal conductivity of Al (237 W/m-K). Another DFT-LD calculation by Wang et al. [97] gives a phonon thermal conductivity of 4 W/m-K for Al at the same temperature. The differences in these results may be ascribed to the difference in pseudopotential used to perform the DFT calculations. Aluminum oxide, on the other hand, is an insulator. Due to the high band gap resulting in the unavailability of conduction band electrons, heat conduction in Al_2O_3 is phonon-dominated. Therefore, the dominant heat carriers in Al_2O_3 are phonons. To our knowledge, there has not been any work reported in the literature that reports the thermal conductivity of Al_2O_3 via DFT-LD calculations.

In this chapter, we try to understand the effect of particle size on phonon thermal conductivity in Al and Al_2O_3 . Here, we first employ a DFT-LD framework to study the temperature dependent phonon thermal conductivity of Al and Al_2O_3 and benchmark the framework with experimental results and/or prior theoretical studies. Secondly, the thermal conductivity accumulation as a function of phonon mean free path (MFP) is evaluated to assess the role of system sizes on thermal conductivity. Ideally, if the system size is larger than the smallest phonon MFP at which thermal conductivity accumulates, then phonons will not be affected by the system boundaries. Conversely, if system sizes are smaller, some of the large MFP phonons will have MFP restricted to the size of the system. These phonons are excessively scattering with the material's boundaries, thereby leading to a reduced thermal conductivity.

3.2 Methodology

Firstly, direct displacement of relaxed lattice structure was performed to create numerous perturbed structures, which was followed by DFT calculations on each of the structure. The DFT calculations were performed by employing LDA for the exchange-correlation functional, and the norm conserving Perdew-Zunger [98] scalar relativistic pseudopotential was used to describe the core electrons. The projector-augmented wave formalism was implemented in QUANTUM ESPRESSO (QE) [71] with a plane wave energy cutoff of 750 eV. The Brillouin zone was sampled using 4x4x4 uniform (Monkhorst-Pack) k-point grids. For the self-consistent field (SCF) calculations, the electron energy convergence threshold was set 1×10^{-7} eV, and for the initial structural optimization, the force/atom convergence threshold was set to 1×10^{-4} eV/Å. Forces on atoms obtained from DFT calculations as well as the displacement values were then used as input to LD calculations.

To perform lattice dynamics calculations, the open-source ALAMODE code [88] was used, which is useful for calculating the harmonic and anharmonic force constants from DFT data and also facilitates the calculation of dispersion relations and the phonon DOS. The phonon DOS was calculated using a 4x4x4 mesh resolution, and dispersion relations were extracted using a fine 150 one-dimensional grid points along each phonon branch. The phonon BTE was solved under a relaxation time approximation (RTA) using a 30x30x30 grid, which produced converged phonon thermal conductivity values that can be compared with our results and with experimental data.

3.3 Results

3.3.1 Phonon dispersion relations

The phonon dispersion relations were calculated from Eq. 2.38. They represent the phonon branches, and their frequencies as a function of wavevector, ω . The phonon group velocity, v_g can be calculated from the derivative of phonon frequency with respect to wave vector, as given in Eq. 2.45. Then v_g can be used in eq. 2.50 to calculate phonon TC from the solution of BTE. In addition, dispersion relations can also be compared with experimental data to ensure that harmonic force constants are evaluated accurately.

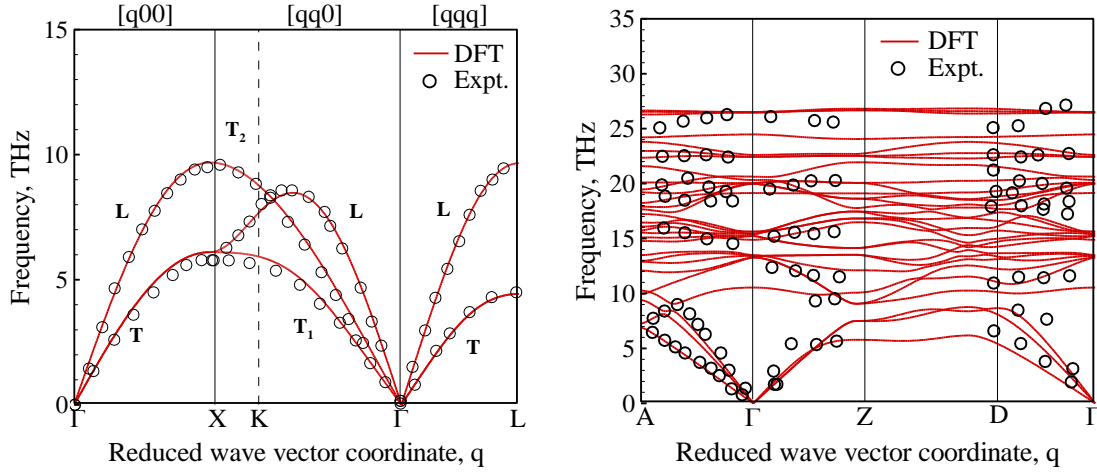


Figure 3.1 Phonon dispersion relations of a) Al and b) Al₂O₃ evaluated via DFT-LD method compared with experimental results [99, 100] suggesting that the phonons are captured reasonably well by the DFT-LD framework

Figure 3.1(a) and (b) show the dispersion relations of Al and Al₂O₃ respectively evaluated via LD calculations. The experimental results are also overlaid for comparison. Figure 3.1(a) compares the transverse (T) and longitudinal (L) branches of phonons along

the different crystal directions. Here, the relations are plotted in the Brillouin zone where the gamma point (center of the Brillouin zone), $\Gamma = 0$. The DFT-LD calculations are in accordance with the experimental results [99]. Figure 3.1(b) compares the phonon branches evaluated by DFT-LD calculations with the experimental results. Note that there is very limited experimental data available on Al_2O_3 phonon branches. Nevertheless, for Al_2O_3 , there is decent agreement between DFT-LD and experimental results. It is, therefore, clear from Figure 3.1 that phonon dispersion relations are reproduced with reasonable accuracy using DFT calculations; such accuracy suggests that the DFT calculations are correct and are useful for modeling the phonons in these materials.

3.3.2 *Phonon density of states*

In addition to the dispersion relations, the phonon DOS also gives important information about phonons present in a crystals. The DOS gives the density of phonons corresponding to different frequencies in a crystal structure. The total number of phonons (i.e. eigenmodes) is three times the number of atoms in the crystal geometry, corresponding to the three degrees of freedom available to every atom. Figure 3.2 shows the phonon DOS for Al and Al_2O_3 crystals obtained from DFT-LD calculations. The experimental data [99] are also overlaid in the figures.

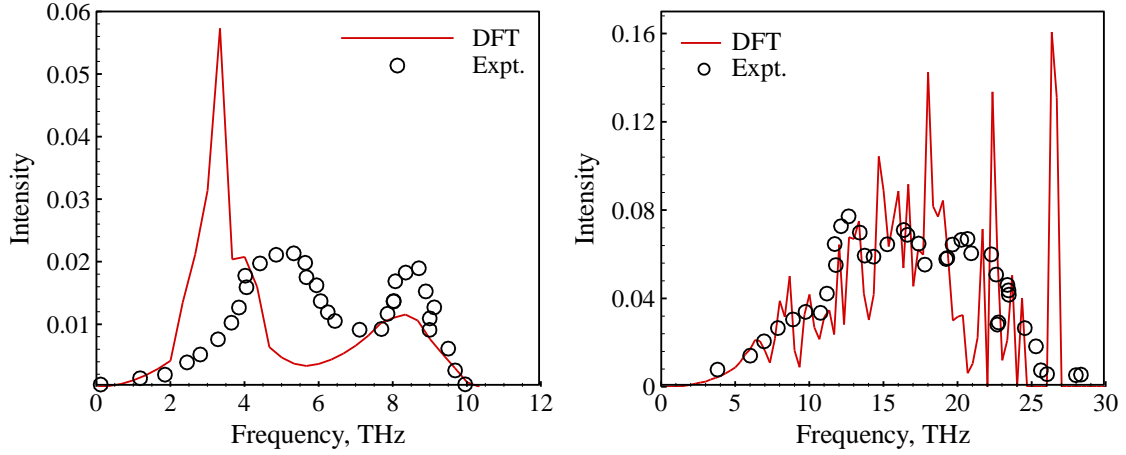


Figure 3.2 Phonon density of states (DOS) of a) Al and b) Al_2O_3 evaluated via DFT-LD method compared with experimental results [99, 100] giving further validation to the fact that the phonons are captured reasonably well by the DFT-LD framework

From Figure 3.2(a), it is evident that for Al, the first peak frequency predicted by DFT-LD calculations is ~ 2 THz lower than that of the experimental values, whereas the second peak frequency is correctly predicted. For Al_2O_3 as shown in Figure 3.2(b), the DFT predictions match well with experimental results. By reproducing the phonon DOS, DFT framework has been further validated, and may be expected to give reasonably good predictions of phonon thermal conductivity.

3.3.3 Phonon thermal conductivity

The temperature dependent phonon thermal conductivity of Al and Al_2O_3 as a function of only p-p interactions are plotted in Figure 3.3(a) and (b) respectively. The phonon thermal conductivity decreases with increase in temperature. The number of active

phonons in a system increases proportional to $k_B T$ where k_B is the Boltzmann constant. This increase in phonons leads in turn to an increase in p-p scattering, which results in a reduction in phonon TC.

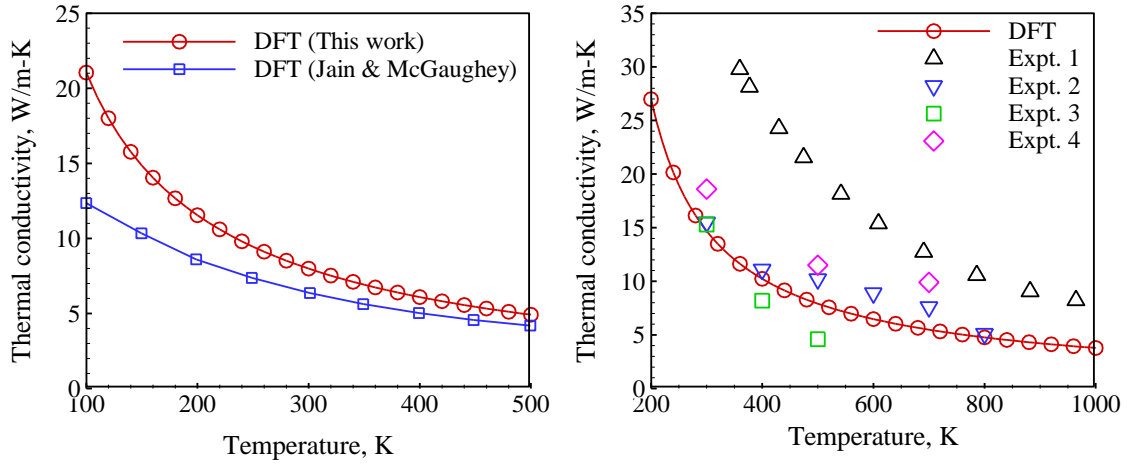


Figure 3.3 Phonon thermal conductivity (TC) of a) Al and b) Al₂O₃ evaluated via DFT-LD method compared with prior DFT calculations and experimental results

Experimental results for the phonon contributions to TC for Al are unavailable because no technique currently exists that can isolate the phonon thermal conductivity by itself. However, one can measure the electrical conductivity, which is intrinsically interrelated with the electronic component of the thermal conductivity. Using this approach, one can indirectly deduce the phonon contribution to the thermal conductivity by subtracting the electron contribution from the total thermal conductivity. However, this is not a very robust method, since it contains aggregated errors from the direct measurement and the subsequent deduction of the electronic thermal conductivity via the Wiedemann Franz law. Furthermore, the Wiedemann Franz law is not a rigorous law but instead a constitutive relation born out of a model for electron conduction and a relation to describe the energy carried by electrons along with their own charge. Nonetheless, deviations from

this law have been frequently observed and this consequently introduces a great deal of uncertainty into the notion that one can indirectly deduce the phonon contribution to thermal conductivity from this approach. As a result, the results of prior DFT-LD calculations by Jain and McGaughey [50] are overlaid for comparison in Figure 3.3(a); our predictions are comparable. To our knowledge, DFT prediction of phonon thermal conductivity of Al_2O_3 has not been reported in the literature. However, experimental results for Al_2O_3 [101-103] thermal conductivity from four different sources are overlaid in Figure 3.3(b). As seen in Figure 3.3(b), our calculations are in accordance with three out of four experimental results. This agreement suggests that the phonon thermal conductivity has been calculated accurately. Thus, the focus in the next section is on assessing the phonon MFP and size effects, which can become important at the nanometer length scales that involve in nAl combustion.

3.3.4 *Phonon thermal conductivity accumulation function*

The thermal conductivity accumulation plot as a function of phonon MFP calculated at $T=300$ K is shown in Figure 3.4. For Al, as can be seen in Figure 3.4(a), phonon thermal conductivity accumulates at a MFP of only ~ 34 nm, as the contributions to thermal conductivity from larger MFP phonons are negligible. This observation suggests that if the system size is below 34 nm, phonon TC can be reduced, as larger MFP phonons become affected by the boundaries. As clearly illustrated by Jain and McGaughey [50] from the study of electron thermal conductivity as a function of MFP of electrons, it is quite evident that TC is affected for system sizes lower than 20 nm.

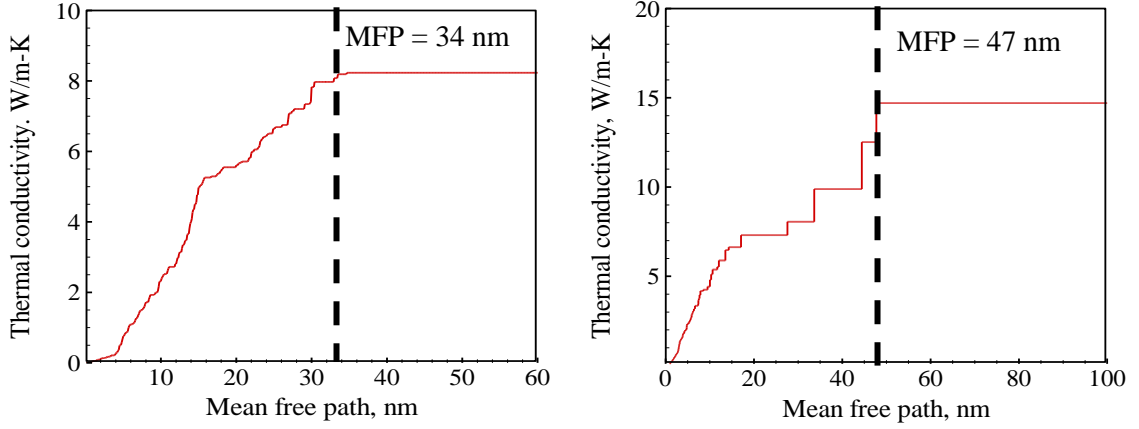


Figure 3.4 Phonon thermal conductivity accumulation plots of a) Al and b) Al₂O₃

For Al₂O₃, however, thermal conductivity saturates at MFP ~ 47 nm as shown in Figure 3.4(b). Hence Al₂O₃ is more strongly impacted by size effects. Nonetheless, neither material is strongly affected as compared to longer MFP materials such as crystalline silicon, where the average MFP is 100 nm but almost half of the bulk TC comes from phonons with MFPs longer than 1 micron.[104] As a result, while modeling the thermal conductivity of a nanoparticle, the effect of particle size (or more conveniently, particle diameter) should be factored in, but only becomes significant for particle diameters less than about 47 nm, and we can roughly approximate the thermal conductivity, k as:

$$k = k_{bulk} \text{ for } D \geq L \quad (3.1)$$

$$k = \left(\frac{D}{L} \right) k_{bulk} \text{ for } D < L,$$

where k_{bulk} is the bulk thermal conductivity, D is the system dimension, L is the peak mean free path at which $k \rightarrow k_{bulk}$.

3.3.5 Spectral thermal conductivity distribution

The phonon thermal conductivity contributions as a function of phonon frequency – termed the spectral thermal conductivity distribution – for Al and Al₂O₃ are given in Figure 3.5(a) and (b) respectively. As can be seen from Figure 3.5(a), for Al, a significant contribution to phonon TC is due to phonons with frequencies in the range 5-8 THz, whereas from Figure 3.5(b), for Al₂O₃, significant contribution is from phonons within frequencies 4-9 THz.

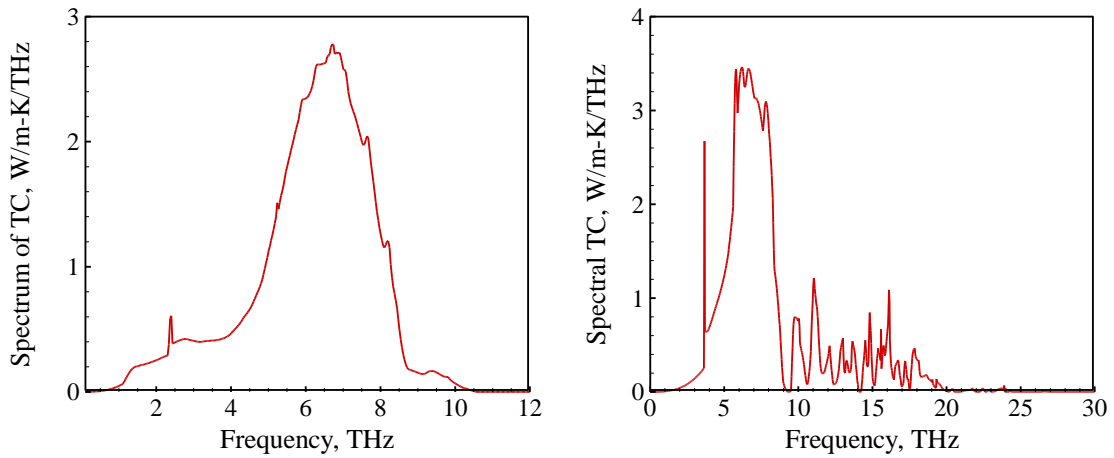


Figure 3.5 Spectral distribution of phonon TC of a) Al and b) Al₂O₃

Spectral thermal conductivity gives the relative importance of phonons at specific frequencies with respect to other phonons. It is assumed the relative importance of these phonon frequencies may be tied to their higher lifetimes and/or MFP's. The phonon lifetimes and mean free paths are analyzed in Section 3.4.6. Both phonon MFP and frequency dependent studies are very important in thinking about phonon engineered materials.

3.3.6 Phonon mean free paths and lifetimes

Continuing from the theoretical formulation of lattice dynamics given in Chapter 2, further information on phonons can be deduced by calculating phonon mean free paths and phonon lifetimes.

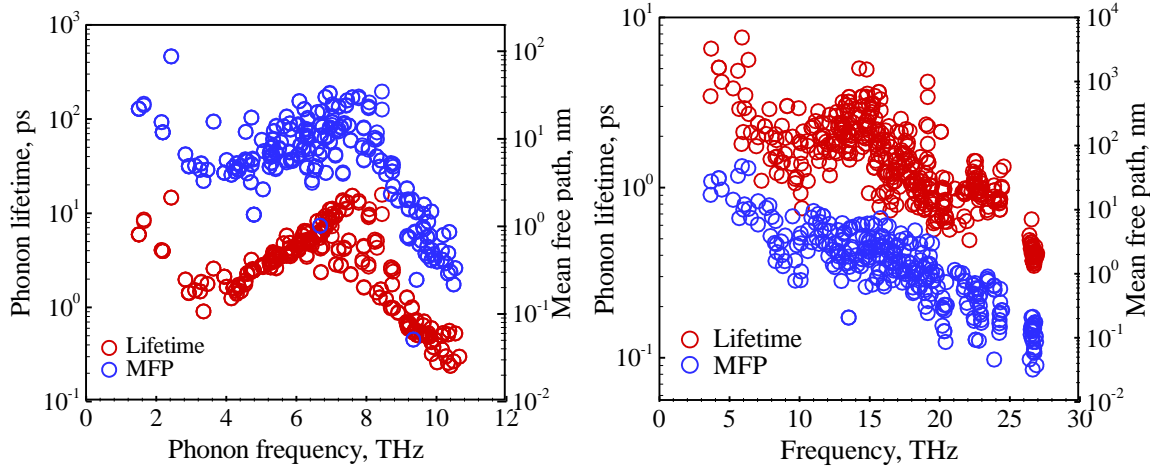


Figure 3.6 Spectral distribution of phonon lifetime and mean free paths of a) Al and b) Al₂O₃

Figure 3.6(a) and (b) shows the spectral MFP and lifetimes of phonons in Al and Al₂O₃ respectively. From Fig. 3.6 (a), it is quite evident that the highest phonon lifetimes are associated with frequencies 5-8 THz in Al. On the other hand, the largest MFP phonons lie within 4-8 THz range. From Figure 3.5(a), it is quite evident that MFP > 30 nm do not contribute significantly towards thermal conductivity. Hence, we focus our attention towards phonons with MFP < 30 nm. The peak phonon MFP as shown in Figure 3.6(a) is ~100 nm. The number of phonons with MFP > 30 nm is also much lower, which corroborates the data depicted in the TC accumulation plot (Figure 3.4). In the case of Al₂O₃, however, the trends are a bit different. The peak frequency and lifetimes correspond

to phonon frequencies 4-9 THz. From Figure 3.5(b), the TC accumulates ~ 50 nm MFP, and correspondingly, the peak MFP of phonons in $\text{Al}_2\text{O}_3 \sim 50$ nm.

3.4 Conclusions

In summary, a detailed analysis of phonon transport properties in Al and Al_2O_3 has been performed via LD calculations using input from density functional theory (DFT) calculations. Firstly, the phonon dispersion relations and phonon density of states (DOS) are evaluated and compared with experimental data. The DFT-LD method reproduces the transverse and longitudinal phonon branches in Al and Al_2O_3 along the edges of Brillouin zone. Substantial agreement is found between LD predictions and available experimental data. Predictions in phonon DOS via lattice dynamics are also accurate. Two peaks in phonon density are observed in Al at ~ 3 and ~ 8.5 THz respectively. When compared with neutron scattering experimental data, the lower frequency is off by ~ 1 THz whereas at higher frequencies, data is reproduced more accurately. This discrepancy is due to neglecting electron-phonon scattering in Al metal. For Al_2O_3 , the DFT-LD predictions of phonon DOS compare well with the neutron scattering data, confirming that the phonon properties are evaluated accurately. Furthermore, temperature dependent phonon thermal conductivity of Al and Al_2O_3 are also evaluated by solving the Boltzmann transport equation (BTE) under the relaxation time approximation (RTA). Calculated phonon TC of Al is very close to prior lattice dynamics calculations. Experimental data on phonon thermal conductivity of Al is unavailable; phonon thermal conductivity of Al_2O_3 evaluated by LD is close to three out of four experimental results reported in the literature.

Furthermore, the thermal conductivity accumulation function was evaluated. Our results suggest that for Al, phonon TC accumulates at mean free path (MFP) ~ 30 nm. This finding suggests that if the system size is below 30 nm, phonon TC can be reduced due to the fact that some of the larger MFP phonons become inaccessible. For Al_2O_3 , however, TC accumulates at a MFP of ~ 50 nm. Hence the system is more easily size affected than Al, but generally speaking the size effects are weaker than many other materials that have been analyzed [50]. Nonetheless, since particle diameters in the range of 10-50 nm are of interest for nAl combustion, the effect of particle size should be considered in modeling the combustion. Spectral distribution of TC was also analyzed to assess the possibility of engineering phonon transport properties. For Al, more than 80% of phonon thermal conductivity is due to phonons within frequencies between 5 and 8 THz. For Al_2O_3 , more than 92% of TC was contributed by phonons with frequencies between 4 and 9 THz. Finally, the phonon lifetimes and mean free paths as a function of phonon frequencies were studied. Complementing the results of spectral distribution, the highest phonon lifetimes and mean free paths in Al were observed for phonons in the 5-8 THz range; for Al_2O_3 , these phonons exist in the 4-8 THz regime. These studies give a fundamental understanding of phonon frequencies and their contribution in pristine bulk Al and Al_2O_3 crystals. The findings in this chapter provide a foundation to understand phonon transport across Al/ Al_2O_3 interfaces, which can now be addressed in the next chapter.

CHAPTER 4. THERMAL CONDUCTANCE OF ALUMINUM-ALUMINUM OXIDE INTERFACE

In this chapter we will try to answer the second thesis question on thermal interfacial conductance (TIC): *How to predict TIC of Al/Al₂O₃ interface accurately? How does TIC vary beyond the melting point of Al? What are the vibrational modal contributions to TIC?* Here, the TIC of Al- α -Al₂O₃ interface along crystal directions (111) Al || (0001) Al₂O₃ is calculated using interfacial conductance modal analysis (ICMA). Results corresponding to temperatures 50-500 K are compared with the available time-domain thermoreflectance (TDTR) experimental data. The benchmarked ICMA framework is then used to predict TIC for temperatures ranging from 500-1800 K. Moreover, modal analysis of interfacial conductance is also performed to understand how various vibrational modes interact and contribute towards thermal conductance.

4.1 Introduction

To understand and quantify thermal interface conductance, G , one may seek experimental measurements, theory-based predictive models, or a combination of both. The time-domain thermoreflectance (TDTR) method, an optical-pump probe technique, is the most widely used experimental method [34, 105-107]. A typical TDTR experiment measures the total conductance but neither resolves the modal contributions nor elucidates the governing mechanisms. Sometimes, merely due to the low thermal conductivity of the constituent sides of the interface, the measurement is incapable of measuring G because of

the low sensitivity to the interfacial resistance. In addition, experimental methods can be challenging and expensive especially from a standpoint of making clean and defect-free interfaces by epitaxial growth, and achieving high temperatures and/or pressures. Moreover, the results are sensitive to experimental conditions thus challenging reproducibility.

Theoretical approaches, in contrast to experiments, are less expensive, and can be performed over wide range of temperatures and pressures. Nevertheless, theoretical models should be thoroughly benchmarked with experimental results before being applied to any practical application. To model interfacial heat transfer, several formalisms/models exist: acoustic mismatch model (AMM) [108, 109], diffuse mismatch model (DMM) [110-112], AGF [113-115], wave packet method (WP) [116-119], harmonic LD based approach [120, 121], and frequency-domain perfectly matched (FD-PML) method [122, 123]. All of these models are based on the *phonon-gas model* (PGM).[124] In the PGM, phonons are treated as gas molecules that interact with other phonons, electrons, or other atoms/molecules and these interactions (or collisions) obey the classical law of conservation of energy and momentum. Within the PGM assumption, the Landauer formalism [125] can then be used to determine the G as:

$$G = \sum_{p_A} \left[\frac{1}{V_A} \sum_{k_{x,A}=-k_{\max}}^{k_{\max}} \sum_{k_{y,A}=-k_{\max}}^{k_{\max}} \sum_{k_{z,A}=0}^{k_{\max}} v_{z,A} \hbar \omega \tau_{AB} \frac{df(\omega, T)}{dT} \right], \quad (4.1)$$

where the summation is performed over different polarizations denoted by p_A and allowed wave vectors $k_{x,y,z}$ in material A; V_A is the volume of material A, $v_{z,A}$ is the phonon group velocity normal to the interface, $\hbar \omega$ denotes the phonon energy wherein \hbar is Planck's

constant divided by 2π and ω is the phonon frequency, τ is the phonon transmission probability, f is the phonon distribution function (Bose-Einstein distribution). The aforementioned methods differ based on how each method calculates the transmission probability. For calculating the thermal conductivity of different materials, PGM based formalisms have achieved excellent agreement with experimental measurements. When it comes to G , however, no general or consistent agreement between theory and experiment has ever been reported. Figure 4.1 compares the predictions of various theoretical formalisms (vertical axis) with the experimentally measured values (horizontal axis).

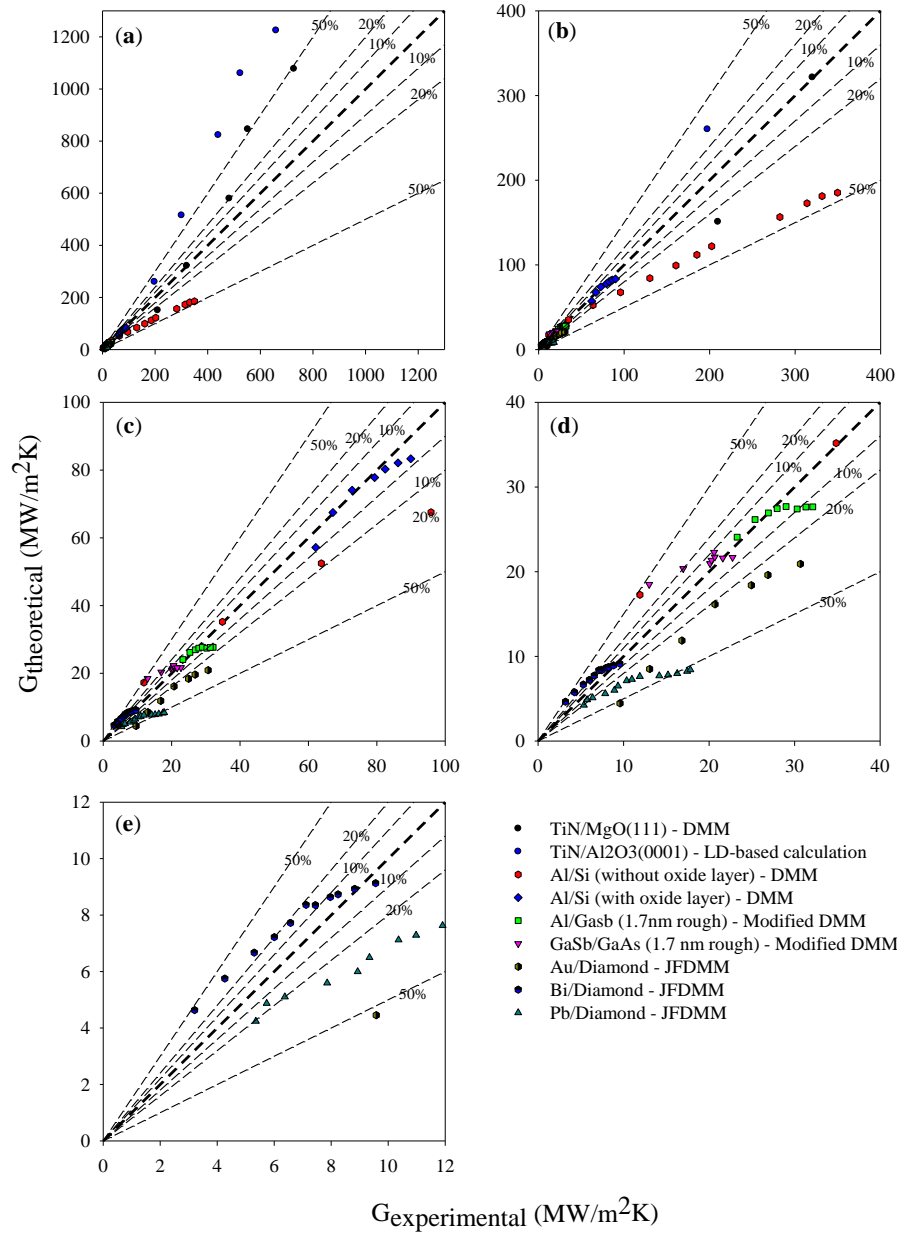


Figure 4.1 Comparison of theoretical predictions of thermal interfacial conductance, G across different interfaces with corresponding experimentally measured values.

In Figure 4.1, for each interface, each point represents a comparison between a calculation and a corresponding measurement, and the multiple points for a given material correspond to different temperatures. Each panel represents a different G range. The dashed lines represent the percent error associated with the theoretical predictions. The examined

interfaces have references as follows: TiN/MgO [126], TiN/Al₂O₃, [126] Al/Si with/without oxide layer [127], Al/GaSb [128] GaSb/GaAs [128], Au/Diamond [35], Bi/Diamond [106], and Pb/Diamond [106]. The modified DMM referenced in the legend was proposed as a variation of DMM to predict TIC across interfaces with severe chemical and structural changes around the interface [129, 130]. JFDMM is a variation of DMM, where the altered phonon frequencies in the interface region were also included in the calculations [131]. It is apparent from Fig.4.1 that all of the models suffer significant disagreement at some temperature. Note that in the Landauer formalism (Eq. 4.1), group velocity, v of all vibrational modes must be calculated to evaluate G . Therefore, rigorously, since the calculation of v is only possible for purely crystalline solids, this approach should only be applied to crystalline solids. When models based on the PGM are applied to calculate TIC, they implicitly assume the interface to be merely a break in symmetry of a crystal and adopts the same treatment used in perfect crystals.[132] Such an assumption in applying PGM to systems with break in symmetry such as interfaces and disordered materials like amorphous materials, alloys, and polymers is highly questionable, since a large population of the vibrational modes in these systems could be non-propagating and localized, for which a group velocity cannot be defined. [133-137]

In addition, many formalisms do not include the intrinsic anharmonicity, which is another important factor that affects heat conduction. Although Mingo [113] has shown that, in principle, anharmonicity can be included in the AGF, this has been neither widely adopted nor applied to any realistic interface. Finally, from Eq. (4.1), it is clear that PGM derives G by using the properties of only one of the two materials forming the interface and the transmission probability, τ . AMM and DMM methods calculate transmission

probability under the assumption of purely specular and purely diffuse scattering of phonons respectively at the interface, which are limiting cases. Although there have been many improvements made to these models from a standpoint of calculating transmission probability, none of them resolve the atomic level detail of interface quality like imperfections, defects, interatomic diffusion, etc.

In this respect, the AGF formalism is superior, since it is capable of including atomic level details and quantum effects. AGF utilizes the harmonic force constants (FC) calculated by means of atomic forces, which can be calculated through first principle methods like DFT or empirical interatomic potentials to determine the transmission function. In the AGF method, for contact area A , G is given by,

$$G = \frac{1}{2\pi A} \int \hbar \omega \frac{\partial f}{\partial T} \tau(\omega) d\omega, \quad (4.2)$$

where the phonon transmission τ at frequency ω is calculated as the trace over the Green's function of the interface and its coupling terms between the bulk material on either end. Although AGF, in theory, combines atomic-scale fidelity with an asymptotic treatment of the bulk material, to our knowledge, no good agreement with experimental measurements have been reported till date. Note also that AGF is intrinsically unable to achieve mode-level details of conduction. Although one may argue that mode-level details can be extracted from the interatomic force constants, since AGF calculates contributions only from the modes existing in the bulk material, it is uncertain whether they are the actual modes present in the interfacial system. The contributions from individual modes are particularly important in materials where all the eigenmodes may not be propagating. The non-propagating modes could be localized or diffusive in nature. Knowing the

contributions of specific eigenmodes facilitates rational design of materials by engineering certain features to target certain group of modes to either inhibit or enhance their role. Therefore irrespective of the underlying theory, emphasis should be given to describing the contributions from the actual modes that exist in the system.

Unequivocally, there is a major gap in the understanding of interfacial heat transport. Considering the inadequacies in PGM, we seek an alternative view of interfacial heat conduction based on the fluctuation dissipation theorem wherein the modal contributions to transport are assessed by the degree to which they are correlated, rather than the degree to which they are scattered. To serve the purpose, the recently reported interfacial conductance modal analysis (ICMA) formalism [138] based on the fluctuation-dissipation theorem and lattice dynamics has important features. In the ICMA formalism, the instantaneous energy transfer across an interface of material A and B can be given as:

$$\mathcal{Q}_{A \rightarrow B} = - \sum_{i \in A} \sum_{j \in B} \left\{ \frac{p_{i,\alpha}}{m_i} \left(\frac{-\partial H_j}{\partial \mathbf{r}_i} \right) + \frac{p_{j,\alpha}}{m_j} \left(\frac{\partial H_i}{\partial \mathbf{r}_j} \right) \right\}. \quad (4.3)$$

Here, $\mathcal{Q}_{A \rightarrow B}$ is the instantaneous energy transfer across the interface of material A and B; p , H , and m represent the momentum, Hamiltonian, and mass of atoms i and j respectively. From this relation, the conductance can be calculated by the time integration of correlation of autocorrelation of the equilibrium fluctuations of the heat flow as:

$$G = \frac{1}{Ak_b T^2} \int_0^\infty \langle \mathcal{Q}_{A \rightarrow B}(t) \cdot \mathcal{Q}_{A \rightarrow B}(0) \rangle dt. \quad (4.4)$$

Since ICMA is implemented in classical molecular dynamics (MD) framework, it is capable of full inclusion of anharmonic contributions to the interfacial heat transfer by all types of vibrational modes including the localized interfacial modes. Most importantly,

ICMA can resolve the modal heat flux Q_n (i.e. $Q = \sum_n Q_n$) yielding the modal contribution to conductance, G_n (i.e. $G = \sum_n G_n$) by utilizing the input eigenvector basis set given as input.

In this chapter, both ICMA and AGF techniques are implemented independently to predict thermal conductance of aluminum (Al)-aluminum oxide (α -Al₂O₃) interface for temperature ranging from 50-500 K. The results are compared with each other and with experiments. Results are also compared with DMM predictions to observe how results vary when purely diffuse scattering mechanism is assumed. Moreover, the mode-level details obtained from ICMA are also reported, which gives the nanoscale picture of the modal interactions and thereby explaining the mechanisms governing interfacial heat transport. After benchmarking the results for T = 50-500 K, ICMA method is extended to 1800 K to evaluate interfacial conductance.

4.2 Simulation details

4.2.1 Interfacial Conductance Modal Analysis (ICMA)

ICMA method is implemented in equilibrium molecular dynamics (EMD). A simulation cell size of ~19.2 nm in length having a cross sectional area of ~80 nm² with 1260 atoms containing an interface with crystal directions (111) Al || (0001) Al₂O₃ representing the primary orientation in FCC metal-metal oxide[64, 139] interfaces is used for the simulations. The system length was chosen based on an initial size-dependency

calculation, which suggested that a system size larger than ~ 18 nm yields a size independent G . To model atomic interactions, the Streitz-Mintmire (SM) potential is used.

Firstly, the system was relaxed in isobaric-isothermal (NPT) ensemble at zero pressure for 2 ns to relieve any internal stresses. After relaxation, the system was equilibrated in a canonical (NVT) ensemble at required temperature for another 2 ns. Following equilibration, the system was evolved in time under microcanonical ensemble (NVE) ensemble for 10 ns. Heat flux was recorded every 5 fs, which is found to be sufficiently low enough to resolve the heat current fluctuations in both the materials. In order to overcome the possible statistical uncertainty due to insufficient phase space averaging, 10 independent ensembles are considered for each temperature. All calculations were performed on Large-scale Atomic/Molecular Massively Parallel Simulator (LAMMPS) [73] package using a time step size of 1 fs. To include the modal decomposition routine, the original SM potential in LAMMPS was modified to accept eigenvector basis set obtained from lattice dynamics (LD) calculations and to output modal contributions to heat current at required intervals. For performing lattice dynamics (LD) calculations, following the NVT equilibration, the system was gradually cooled to 0 K in microcanonical ensemble using Langevin thermostat. The system was then allowed to undergo relaxation at 0 K in NPT ensemble. The relaxed crystal was used as the input for LD calculations performed on General Utility Lattice Program (GULP) [140] from which the eigenvectors of vibration for the structure were obtained. The auto- and cross-correlations between the total and modal heat fluxes from ICMA routine were calculated to obtain the total G and modal contributions, respectively.

4.2.2 Atomistic Green Function (AGF)

To ensure a fair comparison between AGF and ICMA, force constants used in AGF calculation were obtained from empirical LD calculations using the same Streitz-Mintmire potential used in ICMA calculations. In the AGF method, the system consists of two bulk regions of aluminum and sapphire respectively, and an interface region of these two materials. For FC calculation, we used structures composed 36 and 60 atoms respectively to represent bulk structures of aluminum and sapphire, and 96 atoms for interface structure. LD calculations were performed using ALAMODE code [87, 88]. Several initial geometries with atoms displaced from their equilibrium coordinates were input to ALAMODE. To obtain empirical FC, ALAMODE was coupled with LAMMPS, and the SM potential was invoked to obtain forces acting on atoms corresponding to the displaced geometries.

4.3 Results

4.3.1 Total conductance, G

The total G values as a function of temperature obtained from various sources are summarized in Figure 4.2. Results of our ICMA and AGF calculations are compared with the experimental results from three different sources[34, 35, 51] as well as the DMM predictions [34]. Experimental data from 50-300 K are obtained from Stoner and Maris [35], whereas the experimental results for 300-480 K are obtained from Hopkins et al. [51].

Another set of experimental data and DMM calculations reported by Hopkins et al. [34] are also overlaid for comparison. Experimental data above 480 K is not available.

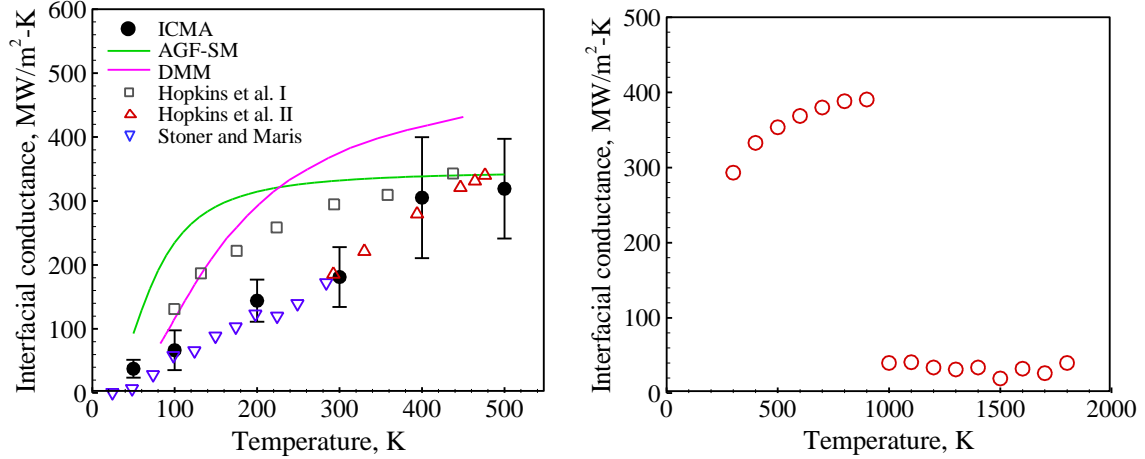


Figure 4.2 a) TIC predicted by ICMA and AGF methods compared with experimental results and diffused-mismatch model (DMM) prediction, and b) TIC predicted by ICMA from T = 300-1800 K

In all these experiments, the samples consisted of thin Al films evaporated onto Al_2O_3 substrates. Firstly, the (0001) plane in the direction parallel to $[2\bar{1}\bar{1}0]$ was obtained by cutting Al_2O_3 substrate followed by vapor deposition of Al atoms. The quality of the surface depends on the technique used to clean the interface, which in turn affects the accuracy of the TIC results. Thickness of Al layer may also affect measured TIC values.[106] Thickness of Al layer must be chosen to be sufficiently larger than the electron MFP in Al to minimize electron scattering at the boundary, to prevent from it acting as an error source for the TIC measurements. For the samples by Stoner and Maris[35], the Al_2O_3 surface was polished with Syton (colloidal SiO_2 in water), and the surfaces were confirmed virtually perfect from high-energy electron diffraction. Thickness of deposited Al layer, however, is not reported. Hopkins et al. I[34] and II[51] cleaned the surfaces by a chemical

rinse using acetone, methanol, and isopropyl alcohol in both of their studies. However, data represented as Hopkins et al. I used an Al layer of 90 nm and Hopkins et al. II deposited an Al layer of ~ 75 nm, which may be the reason for the discrepancies in TIC values. Nonetheless, two of the experimental results suggest a near-linearly increasing trend in G v/s T in the temperature range considered, that is captured quite well by ICMA. The mean quantitative error in ICMA calculations when compared with these experiments is under 5% and the qualitative trend is also in agreement with two of the data sets.

As seen in Figure 4.2(a), except for a slight proximity with Hopkins et al. experimental results below 150 K, DMM predictions are considerably above the experimental results. This is possibly because of the severely restrictive assumption on phonon scattering to be purely diffusive in nature. The green line represents the results of AGF calculations. It is quite evident that except for the coincidence with the experimental result of Hopkins et al. at $T = 450$ K, the AGF significantly over-predicts G from 50-450 K. The temperature trend of G predicted by AGF is also not in agreement with two of the experiments. AGF results steeply rise from 50-100 K and plateaus thereafter. At higher temperatures, G is nearly constant; no temperature dependence is observed.

We attribute the poor predictive power of AGF to two factors. Firstly, AGF does not take into account the intrinsic anharmonicity associated with the vibrational modes, which can play a vital role in heat conduction.[113] Secondly, the only mechanism that the AGF accounts for, in evaluating the temperature dependence is the quantum (Bose-Einstein) correction applied to the modal calculations. This is different from ICMA in which we calculate conductance using classical MD followed by quantum correction at every single temperature, thereby including anharmonicity and the quantum effect on

specific heat. To examine these ideas, a detailed analysis of modal anharmonic energy distribution and modal contribution to G is discussed in the following sections.

With this high level of accuracy in predictions, ICMA can be deemed to be thoroughly benchmarked with experiments, and can be extended to higher temperatures as well. Figure 4.2(b) shows the results of G calculated via ICMA for $T = 300\text{-}1800$ K, an ideal temperature regime of combustion of nano-suspensions. As can be seen from Figure 4.2(b), G increases monotonically with temperature until the melting temperature of Al = 933 K. At the melting temperature, there is a sharp fall in TIC, which remains nearly constant thereafter. This is due to the loss of crystallinity of core Al lattice as it melts. A perfect crystal has

4.3.2 *Modal Analysis*

Partial DOS of the interface structure, modal summation of TIC, and mode-mode correlations at 300 K is shown in Figure 4.3(a)-(c) respectively. Figure 4.3(a) shows the partial DOS calculated from the eigenvector basis set obtained by lattice dynamics calculations. From the partial DOS, we can identify four types of modes based on their participation ratio as: i) extended modes, ii) partially extended modes, iii) isolated modes, and iii) interfacial modes.[133, 134, 138] Extended modes are present at the interface, but the majority of them by contrast, are delocalized into both materials. Partially extended modes are also present at the interface, but majority of them are not present at the interface, and are localized on one side of the interface. Isolated modes exist far away from the interface while interfacial modes are localized vibrational modes which are mostly present

at the interface. Figure 4. 3(b) shows the dominance of partially extended modes in Al (< 9 THz) and Al₂O₃ (<12 THz) and the negligible presence of extended modes (< 0.6 THz). A small percentage of modes (> 9 THz) are interfacial in nature whereas the remaining modes seem to be isolated.

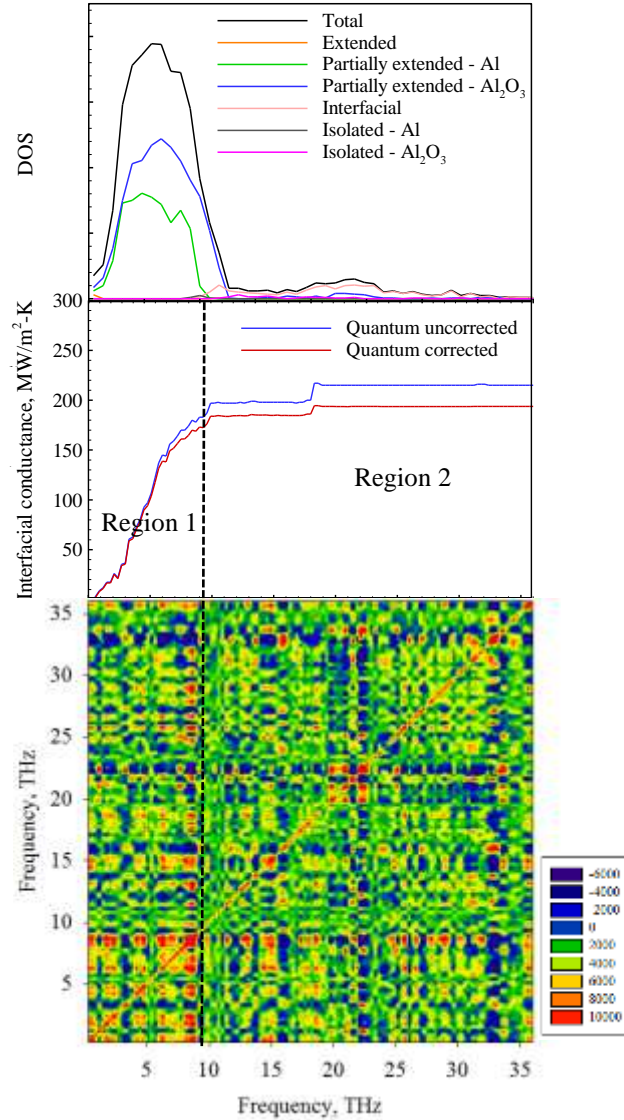


Figure 4.3 a) Partial DOS showing different types of modes, b) TIC accumulation (In this system, >90% of the total conductance is contributed by partially extended modes on Al and Al₂O₃, and the extended modes below 12 THz, c) mode-mode correlation map at T = 300 K showing three distinguishable regions.

In Figure 4.3(b) and (c), two distinguishable regions are marked as Region 1 and 2. Region 1 is below 9 THz marking the peak frequency in Al. Region 2 comprises all frequencies above 9 THz. In region 1, distinct regions of strong positive correlations are observed. Except below 0.6 THz where extended modes are present, this region is dominated by the cross-correlation (CC) of partially extended modes of Al with that of Al₂O₃ reflecting as red regions in the correlation map. Considering the large population of states of partially extended modes of Al and that of Al₂O₃, this region of high CC is the major reason for the initial high slope of TIC accumulation until ~ 9 THz. After that, within region 1, 9-12 THz marks a narrow region of interaction between interfacial and partially extended modes of Al₂O₃, which due to a combined effect of weak correlations and low density, only gives a very shallow slope in TIC accumulation.

From 12-15.5 THz, interfacial modes, and the isolated and partially extended modes of Al₂O₃ co-exist. This frequency ranges in region 2 also shows a strong correlation. However, the very low density of these modes is a clear evidence of the small increment of G in this region. In region 2, the modal characteristics shift drastically from strong positively to strong negatively correlated regions in effect canceling each other, maintaining a cumulative G constant until ~17.5 THz. From 17.5 THz to 22.5 THz, there are observable regions of strong correlation and a slight increase in the density of vibrational states. Especially around the diagonal, there is a strong observable positive correlation from the interaction between the interfacial modes. The combined effect is a jump in G accumulation in Figure 4.3(b) at around the same frequency i.e. 17.5 THz. In order to further gauge the role of each mode, it is important to obtain the contribution of each type of mode normalized by the DOS i.e. G/DOS .

Table 4.1 Contribution of different types of modes to partial DOS and G, and the percentage relative contribution of G to DOS

Mode Type	$DOS(\%)$	$G(\%)$	G/DOS
Extended	0.18	0.31	1.72
Partially extended	89.52	91.83	1.02
Interfacial	9.31	7.80	0.84
Isolated	0.90	0.06	0.07

Table 4.1 shows the population of each type of mode in partial DOS , and their contribution towards G . Also given is the normalized contribution of G . The high density of partially extended modes in the region from frequency < 12 THz corresponding to 89.52% of DOS together constitute towards ~92% of TIC . The G/DOS ratio of partially extended modes ~1 suggesting that the role of partially extended modes in G is justified by their presence in the partial DOS . In the remaining 10.5% modes, 9.31% is constituted by interfacial modes and under 1% by isolated modes. The percentage of extended modes in the system is only 0.18%. Prior studies have shown that extended modes occur on regimes with high frequency overlap.[133, 134]. Therefore, it is surprising that, given the great degree of frequency overlap in this regime, the percentage of extended modes is significantly low. This suggests that whether or not the extended modes are likely to exist within a frequency regime is not purely dictated by frequency overlap, but may also require matching structural structures. Since Al and Al_2O_3 have significantly different crystal

structures, it may be difficult for the modes of vibration of each material to extend throughout the interface structure while not only conserving energy (i.e. frequency) but also momentum (i.e. wavelength).

Also considering the G/DOS value of 1.72, it is to be understood that there is a disproportionately high contribution to G from the extended modes for their relatively small presence in DOS . Therefore, we doubt that the presence of high concentration of extended modes is the reason for the apparent high G of cSi-cGe [134] interfacial system reported in a prior work. We believe that for the Al/Al₂O₃ system, a major portion of G is contributed by partially extended modes, subsequently helping us achieve realistic predictions. In summary, ICMA has not only been able to provide an accurate theoretical prediction of interfacial conductance, but also capture the physical picture of modal interactions governing thermal transport.

4.4 Conclusions

The TIC of the aluminum (Al)-aluminum oxide (α -Al₂O₃) interface along the crystal directions (111) Al || (0001) Al₂O₃ has been accurately predicted. Two fundamentally different approaches: interfacial conductance modal analysis (ICMA) and atomistic green function (AGF) method in the temperature range 50-500 K. While AGF over predicts G , predictions of ICMA show great agreement with experimental results both quantitatively and qualitatively. The ICMA formalism seems to do a better job of explaining the experimental data than the PGM based models, which can be ascribed to its more fundamental treatment of the interfacial heat flux, its inclusion of full anharmonicity of vibrational modes, and for its ability to access to phonon mode level details. Using the

benchmarked ICMA framework, the TIC of Al/Al₂O₃ interface was calculated for temperatures up to 1800 K. It was observed that TIC increases monotonously up to the melting point of Al (= 933 K) and drops sharply by an order of magnitude thereafter. Experimental measurement of TIC at higher temperatures is challenging, hence ICMA provides a promising way to achieve this. In a real combustion system, elevated temperatures exist, and in the ignition and combustion zone, Al exists in molten state. In this regime, the significantly low TIC value could be a major resistance to overall heat conduction in the nanosuspension. In summary, we quantified TIC across a wide range of temperatures, which can now be fitted to a mathematical model.

CHAPTER 5. INTERFACIAL NANOLAYER AND BROWNIAN MOTION: THE ISSUE OF ARTIFICIAL CORRELATIONS

In this chapter, we will try to address the third thesis question: *Do Brownian motion and nanolayer actually contribute towards thermal conductivity enhancement in nanosuspensions?* The role of interfacial nanolayers and Brownian motion in the enhanced thermal conductivity of nanosuspensions is a widely debated topic [36, 141-143]. Phenomenological models and corroborating MD simulations indicate that nanolayering is a possible cause of enhanced heat conduction in dilute suspensions of nanoparticles. In this chapter, MD simulations are studied in deeper detail than previous works to evaluate the possibility of thermal conductivity enhancement from nanolayering and Brownian motion.

5.1 Introduction

It has been hypothesized in the seminal work by Koblinski et al. [36] that for a dilute nano-suspension, in addition to the particle and fluid thermal conductivities, there also exist *dynamic* mechanisms that contribute towards thermal conductivity enhancements. These are Brownian motion and nanolayering, respectively. Brownian motion is the random thermal motion of dispersed nanoparticles in fluid. It is hypothesized to aid in ballistic heat exchange between the particles as well as create regions of localized convection called micro-convection. A nanolayer is a structured/ordered fluid layer formed on the surface of the nanoparticle owing to its excess surface energy. Nanolayers have also

been hypothesized to act as a conduit in conducting heat from the particle to the fluid, and thus helping in overcoming the high thermal resistance at the interface.

Numerous studies report thermal conductivity predictions of nanofluids using Green-Kubo (GK) relations [37, 40, 62, 144-149]. Sankar et al. [145] used a platinum-water nanofluid system with volume fractions (ϕ) in the range of 1-7%. Atomic interactions were modeled using Lennard-Jones (LJ) and Spohr-Heinzinger potentials. Results suggested a 70% enhancement in thermal conductivity at $\phi=7\%$. A physical explanation was not given, but one possible reason for the high prediction is that the analysis did not consider the enthalpy correction introduced in Eq. 2.39. Sarkar et al. [62] studied a system of 2 nm copper particles in argon fluid using LJ potential to model interactions. An enhancement of 52% was reported for $\phi=8\%$, which is significantly higher than Maxwell model (26%) [28]; this was attributed to Brownian motion effects. Note that the Maxwell model is based on the effective medium theory (EMT), which assumes a fully dispersed dilute nanofluid with non-interacting suspended nanoparticles. In this idealized case, the thermal conductivity increase associated with the addition of the solid phase, should simply scale with the respective volumes of each phase and their respective thermal conductivities, since their interactions are neglected. In reality, however, particles can interact and undergo Brownian motion resulting in a stirring effect. Consequently, several modified Maxwell models were developed, and these unusually high thermal conductivity enhancements in MD simulations were credited to Brownian motion effects [60, 150]. Although earlier experimental studies [41, 151] also support this theory, Brownian motion may not be of concern owing to the large timescales associated with particle motion [42, 44].

While experimental measurements do not indicate the formation of a liquid layer over the particle surface that has the potential to enhance thermal conductivity, several computational studies using MD simulations report significant thermal conductivity enhancements. Another theory that has been proposed to explain the anomalous enhancement is based on the formation of a nanolayer around the particle [37, 40, 152], which is believed to function as a high thermal conductivity conduit for interfacial heat flow. Interfacial resistance, on the other hand, has an opposite effect. Over the last decade, there have been several attempts to include the effects of nanolayering and interfacial resistance in classical thermal conductivity models. Yu and Choi [52] developed a modified Maxwell model, by treating particle-nanolayer core-shell complexes dispersed in the base-fluid. By judiciously choosing a constant nanolayer thickness of $\sim 2\text{-}3$ nm and nanolayer thermal conductivity of $10\text{-}100 k_f$, reasonable agreement with experimental data was achieved. The core-shell complex particle assumption was also used by several other researchers to develop effective thermal conductivity models [54, 55]. These models only yield qualitative descriptions of the variations of effective thermal conductivity with particle volume fraction and particle size. In the GK calculations by Sachdeva et al. [40] for copper-water nanofluids, an advanced flexible-3-center (F3C) model for water and the finitely extensible nonlinear elastic (FENE) potential for copper were used. Results showed an enhancement as high as 80% for $\phi = 5\%$ and 1 nm particle. This was attributed to hydration layering on the copper surface. This argument relies on earlier [52] and concurrent [153] experimental investigations favoring nanolayer effects. Yu and Choi [52] attributed an enhancement greater than 40% (for $\phi = 3\%$) solely to nanolayering, whereas, Feng et al. [153] suggest contributions from both nanolayering and particle aggregation.

Recent studies, however, have shown that the thermal conductivity of the adsorbed layer is only marginally greater than that of the base fluid [57, 58]. Taking the high interfacial resistance also into consideration, the nanolayer theory may not conclusively explain the results [154].

It is evident that GK relations often give high thermal conductivity values, but the physical origin of this behavior is elusive. It is counterintuitive to obtain thermal conductivity enhancements for fully-dispersed nanoparticle suspensions higher than the EMT models. We hypothesize that the results of prior MD simulations might have been contaminated with numerical errors arising from artificial correlations due to periodic boundary conditions. To test this hypothesis, we conduct a detailed MD analysis that may offer a physical explanation for the underlying mechanisms at play. In the following sections, we conduct systematic EMD simulations using alumina-water nano-suspensions, and calculate the effective thermal conductivity for a range of volume fractions and particle sizes. We also investigate the origin and effects of artificial correlations in thermal conductivity calculations.

5.2 Methodology

EMD simulations are conducted for a system consisting of a single alumina (Al_2O_3) nanoparticle and water molecules. GK relations are used to calculate thermal conductivity at a temperature of 300 K. Partial enthalpy correction is applied. The volume fraction is in the range 1-10%. Particle sizes of 1 and 3 nm are considered. Note that when the particle size is changed, simulation cell size is readjusted to obtain the target volume fraction.

Atomic interactions within Al_2O_3 are modeled using the potential function developed by Vashishta et al. [76]. Interactions in water are captured using the Extended Simple Point Charge [75] (SPC/E) model, with bonds constrained by the SHAKE algorithm [155]. Long-range electrostatic interactions are treated by particle-particle-particle-mesh (pppm) summation [75]. The alumina-water cross-interaction is modeled using Lorentz-Berthelot mixing rules [79]:

$$\begin{aligned}\sigma_{ij} &= \frac{\sigma_{ii} + \sigma_{jj}}{2} \\ \epsilon_{ij} &= \sqrt{\epsilon_{ii}\epsilon_{jj}}\end{aligned}\tag{5.1}$$

where $\epsilon_{\text{Al-Al}} = 1.4383 \times 10^{-8}$ eV, $\sigma_{\text{Al-Al}} = 5.3814$ Å, $\epsilon_{\text{O-O}} = 1.6847 \times 10^{-3}$ eV, and $\sigma_{\text{O-O}} = 3.9883$ Å [156].

The nanoparticle and water systems are independently equilibrated at the target temperature. For the water system, isobaric-isothermal (NPT) ensemble is used and PBC are imposed in all three directions. Temperature and pressure were controlled by Nose-Hoover thermostat and barostat, respectively. For the nanoparticles, the microcanonical (NVE) ensemble is used, and free boundary conditions are imposed on all directions. A Berendsen thermostat [157] is used to maintain the temperature of the nanoparticle at 300 K. The suspension is created by creating a spherical cavity at the center of the water domain and inserting the equilibrated nanoparticle in the cavity. Care was taken to make sure that there is no overlap of atomic positions. The box dimensions were chosen based on the volume fraction, while ensuring that densities of both materials match the experimental counterparts. After the particle and water systems are independently equilibrated, they are combined, as shown in Figure 1 (a). The resulting system is equilibrated at 300 K and 1

bar in Nose-Hoover isobaric-isothermal (NPT) ensemble for 100 ps using a time step of 0.1 fs. The thermal conductivity calculation is then carried out for a time period of 5 ns; heat current correlation times are in the range 2.5-10 ps. All simulations are conducted using the LAMMPS [73] MD code; the Verlet Algorithm is used for time-integration.

5.3 Results and Discussion

5.3.1 Thermal conductivity of water

Figure 5.1 shows thermal conductivity of water as a function of temperature calculated from GK relations using different interatomic potentials. Experimental results are also overlaid for comparison. As can be seen from Figure 5.1, the thermal conductivity of water increases from 0.72 to 0.81 W/m-K, when the temperature increases from 300 to 370 K. Predictions differ from experimental values marginally, suggesting the model is valid and SPC/E potential is effective for calculating the thermal properties of water.

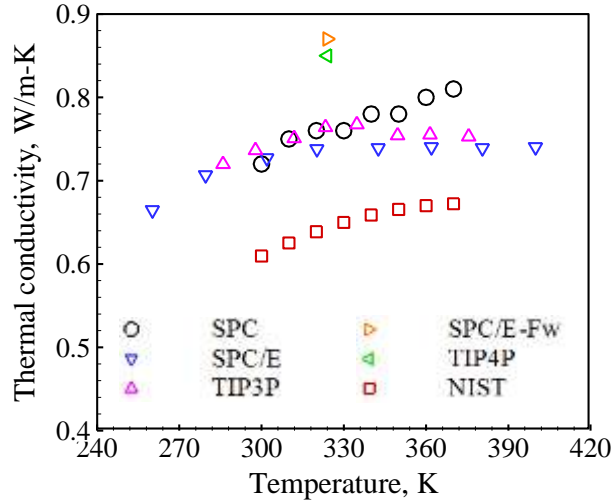


Figure 5.1 Thermal conductivity of water as a function of temperature evaluated by MD simulations using different potential functions, compared with experimental results

5.3.2 Thermal conductivity of nano-suspensions

Figure 5.3 shows the variation of effective thermal conductivity (k_e/k_f) of the mixture with volume fraction (ϕ). Results suggest a near-linear variation of k_e/k_f with ϕ , aligning well with the behavior of nanofluids [158]. For a particle size of 3 nm and $\phi \sim 9\%$, k_e/k_f is $\sim 200\%$, substantially greater than the predictions of the nanofluid thermal conductivity models [28, 52, 53, 159]. As particle size is reduced to 1 nm, the enhancement increases to 235% at $\phi \sim 9\%$. This is similar to the observations of other researchers [40]. In the absence of aggregation or Brownian motion, enhancements may be credited to possible nanolayer effects, but that hypothesis can be tested. In essence, the nanolayer thickness, h , may be estimated using a radial density profile, as shown in Figure 5.2(b), evaluated using 0.5-1 Å thick spherical shells around the particle. The nanolayer can be approximately taken as the region between the particle surface and the shell in which the

density reduces to the bulk density of water. For the cases in Figure 5.2, the estimated nanolayer thickness is $\sim 6.5\text{-}9\text{ \AA}$ or 2-3 atomic layers, and it is independent of the particle size. This is in agreement with the physisorption theory [160] as well as with *ab initio* findings [161]. As a result, smaller particles may be expected to have a higher relative nanolayer thickness, h/D , resulting in a higher thermal conductivity, producing a seemingly convincing validation of the nanolayer hypothesis.

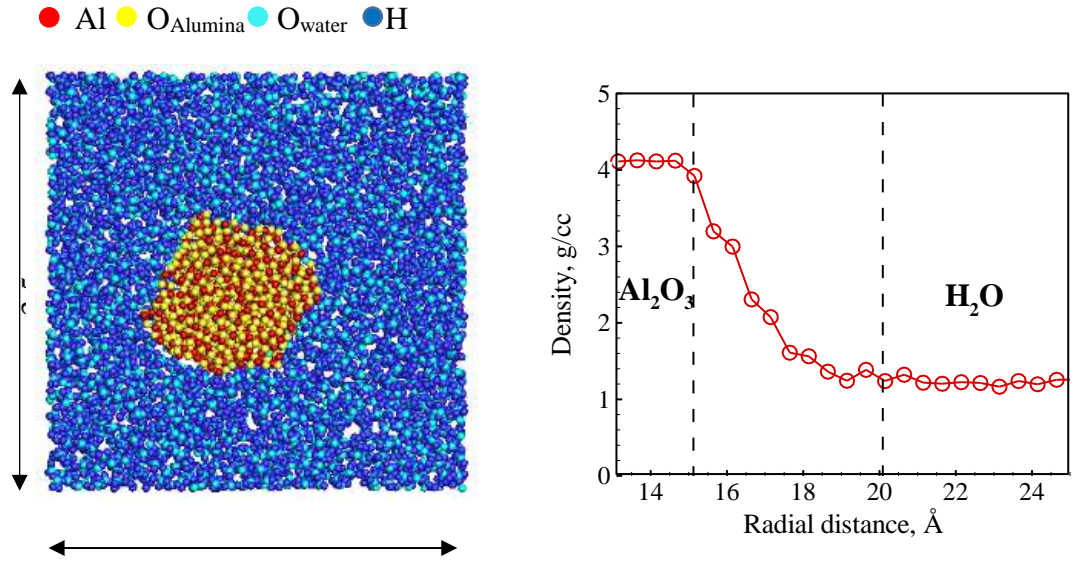


Figure 5.2 (a). Cross-section of single nanoparticle simulation system, and (b) radial density profile for 1 nm particle suspension at $\phi \sim 1\%$

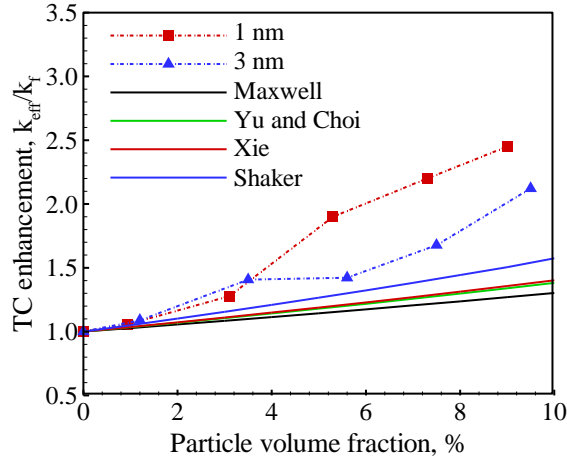


Figure 5.3 Enhancement in effective thermal conductivity (TC) as a function of particle volume fraction compared with various thermal conductivity models

This hypothesis, however, has several issues. Firstly, as seen in Figure 5.2(a), the nanoparticle is not a perfect sphere. Surface roughness, with a characteristic dimension of a few angstroms, could contribute to an increase in mass density near the surface. Furthermore, water layering occurs mainly by hydrogen bonding, which does not cause significant density changes [162], as reported in other works [37, 40]. In addition, the NEMD analysis of Liang et al. [58] suggests that the nanolayer thermal conductivity is only ~1.6 times that of the liquid, suggesting its insignificant role in interfacial conduction.

Figure 5.4 below shows thermal conductivity enhancement as a function of particle thermal conductivity. As shown in Figure 5.4, at lower volume fractions, 3 nm particle suspensions have a higher thermal conductivity than 1 nm particle suspensions, probably because the system sizes are so large that the effect of artificial correlations are not very strong. However, as the volume fraction increases (or system shrinks), these effects intensify, and we observe a shift in the trend.

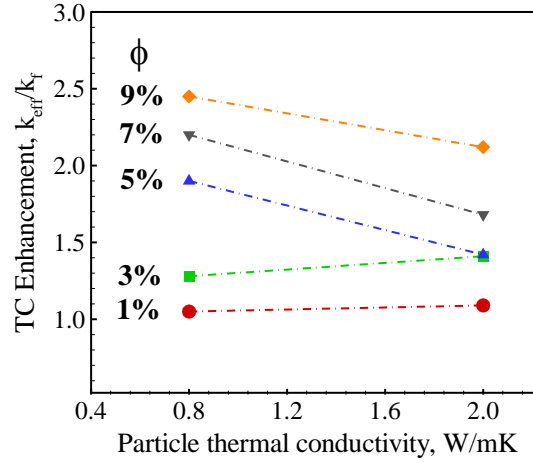


Figure 5.4 Enhancement in effective thermal conductivity (TC) calculated from single particle simulations as a function of particle thermal conductivity for various volume fractions

5.3.3 Artificial correlations

The size effect on thermal conductivity poses concerns. Figure 5.5 shows the effect of particle size on thermal conductivity, k_p , of alumina nanoparticles. For a 1 nm particle, k_p is only about one-fifteenth of the bulk value. This is expected, as the phonon MFP decreases with decreasing particle size due to boundary scattering [46] and accessible phonon modes are limited due to size-restricted phonon wavelengths. This suggests that the effective thermal conductivity of nanofluids may decrease with decreasing particle size, contrary to the trend shown in Figure 5.3.

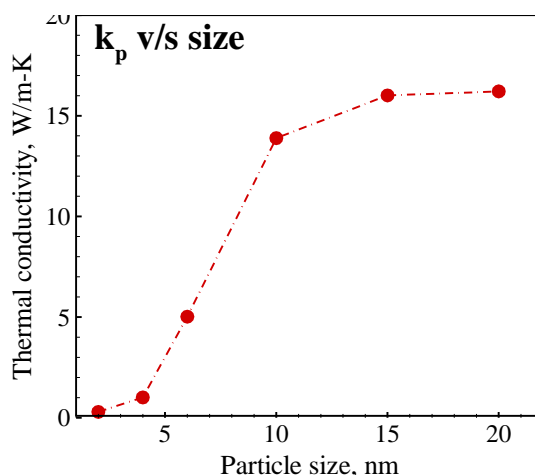


Figure 5.5 Thermal conductivity of alumina nanoparticle as a function of particle size

This contradiction highlights two factors governing the calculated thermal conductivity, namely the magnitude of the HCACF, and the time required for the fluctuations to lose correlation. If the correlations are large and/or remain intact for a long time, greater thermal conductivity may be expected. As periodic boundary conditions are imposed, it is possible that an atom will experience perturbations from its own periodic image. In particular, an atom can thus experience an artificial enhancement in the self-correlated heat current, as its motion perturbs the surrounding atoms, which can then be transmitted through the entire supercell back to itself. The returning and initial perturbations are likely to be well-correlated, as they originate from the same atom. This is unrealistic because every atom is unique, and perturbations to its surrounding environment can never possess a circular resonance with its own motion, in reality. The observed thermal conductivity enhancement could thus simply be a numerical artefact arising from the periodic boundary conditions.

Disparities in vibrational frequencies may also play an important role in exacerbating this problem. Comparison of the vibration spectra of alumina and water [76,

163], as shown in Figure 5.6, reveals that the frequencies associated with water are 3-4 times higher than that of alumina. Consequently, water would experience vibrations of alumina atoms as low frequency waves. As lower frequency waves can be transmitted farther through a medium, since they experience less attenuation[164], alumina vibrations have a greater propensity to establish a circular resonance from the PBC. These perturbations can thus form a feedback loop if they are not sufficiently damped by the surrounding water molecules. Furthermore, this effect would be more pronounced in smaller simulation domains and/or systems with long-range forces, such as those in ionic suspensions.

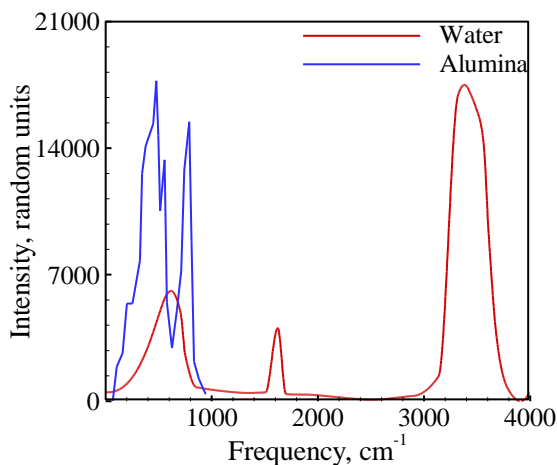


Figure 5.6 Comparison of the vibrational spectra of water and alumina

For the alumina-water system, the electrostatic part of the SPC/E force-field is truncated at 10 Å, whereas the Vashishta et al. [76] potential is truncated at 6 Å. For a 1 nm particle suspension, however, the minimum distance between an alumina atom and its nearest image is only ~4 Å. Therefore, in such a small supercell, an atom can experience self-interactions, which are intrinsically correlated, and consequently lead to a component

in the HCACF associated with fictitious self-correlations. As the particle size and volume fraction decreases, the system gets larger and self-interactions and artificial correlations are suppressed. This is an intrinsic problem associated with PBC and small system sizes, but the problem can be mitigated by choosing a system size large enough to minimize artificial correlations. This, however, imposes constraints on the maximum attainable volume fraction with single-nanoparticle, although only volume fractions as high as 20-30% are of concern for many practical propulsion and energy-conversion systems. Alternatively, we may use multiple nanoparticles in the system, as illustrated in Figure 5.7(inset).

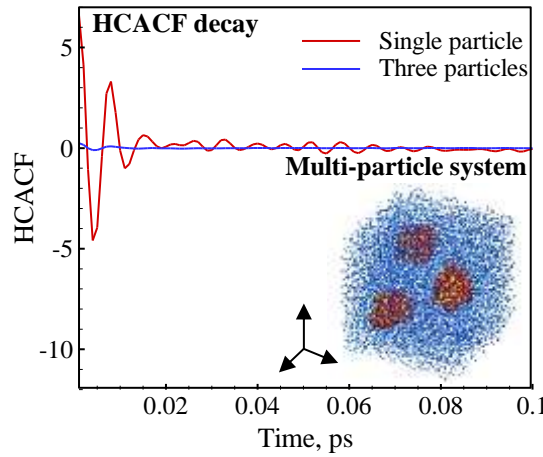


Figure 5.7 Time decay of heat current autocorrelation function 1 nm particle, $\phi = 10\%$; *Inset*: multi-particle simulation system

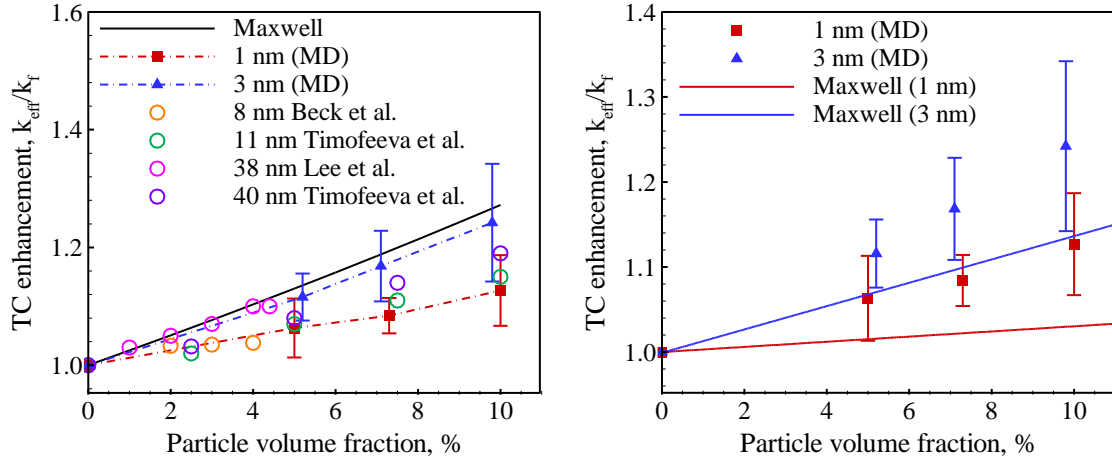


Figure 5.8 Enhancement in effective thermal conductivity (TC) calculated from multi-particle simulations as a function of particle volume fraction compared with (a) Maxwell model[28] with bulk thermal conductivity of alumina and experimental results[1, 2] (b) Maxwell model with thermal conductivity of alumina particles from Fig. 5.5

It is logical to expect that the addition of more nanoparticles is likely to hamper the development of artificial self-correlations due to the presence of unrelated perturbations from other nanoparticles, thereby breaking the symmetry that a single particle tries to establish with its own image. This hypothesis was then tested by comparing the time decay of HCACF for single and three-particle systems, as shown in Figure 5.7. For single-particle systems, HCACF oscillates substantially before decaying to zero. These fluctuations are, however, damped in three-particle systems, resulting in a quicker and smoother decay. Prior studies attributed these oscillations to back-scattering of phonons at the particle-fluid interface [36] or to the relative motion of dissimilar atoms [83]. However, the results of the present study, suggest that the oscillations are merely associated with artificial correlations.

The thermal conductivity was then recalculated for multi-particle supercells. By gradually increasing the particle count and testing for convergence, it was found that a minimum of three alumina particles are required to diminish the artificial correlations.

Multiple initial configurations were used to remove any directional dependencies, and an average of twelve independent runs were used to calculate thermal conductivity. Figure 5.8(a) shows the resulting variation of k_{eff}/k_f with ϕ for different particle sizes and the MD predictions are compared with experimental results [1, 2] and the Maxwell model. In Figure 5.8(a), bulk thermal conductivity is used, while in Figure 5.8(b), nanoparticle thermal conductivity (from Figure 5.5) is used. Experimental data correspond to nanofluids with negligible aggregation. The results do not suggest any anomalous enhancement beyond the Maxwell model. In fact, MD predictions are slightly lower than the Maxwell model, and agree well with the experimental data. Furthermore, the effective thermal conductivity also increases with increasing particle size, which is consistent with the size dependent thermal conductivity behavior of nanoparticles. Figure 5.8(b) shows that MD predictions are marginally greater than Maxwell model predictions, when the nanoparticle thermal conductivity values are used instead of the bulk values. This may be because the Vashishta potential underestimates the thermal conductivity of alumina, as explained earlier.

5.4 Conclusions

To conclude, an alternative explanation to the unusually high thermal conductivity of nano-suspensions obtained using Green-Kubo relations has been investigated. While prior studies credit them to dynamic heat transport mechanisms, our results suggest that these high values are merely an outcome of artificial correlations, arising from single nanoparticle systems and PBC, thereby introducing artificial contributions to the heat current autocorrelation function (HCACF). This problem is expected to be prominent for

systems in which vibration frequencies of the constituents are disparate. In such cases, low frequency perturbations are transmitted through the surrounding high frequency medium and return to the originating particle due to PBC. The resulting circular resonance contaminates the HCACF, which is more pronounced for smaller particles and/or higher volume fractions. In an effort to alleviate this artifact, multi-particle systems were considered. The presence of additional particles impedes the development of artificial self-correlations by breaking the particle-image symmetry. Thermal conductivity predicted from the rectified HCACF is in good agreement with experimental data and the Maxwell model predictions. It is to be noted that the required minimum number of particles depends on the simulation system, which can be determined by devising an appropriate convergence test. In summary, Brownian motion and nanolayering have negligible roles on enhancing the effective thermal conductivity of a nanosuspension and they need not be explicitly included in the effective thermal conductivity model. Therefore, in the following chapter, we will not be including their contributions in the thermal conductivity model, whereas the size and temperature effects on phonon thermal conductivity and the interfacial conductance will be explicitly included following a series resistance circuit model described in Chapter 2.

CHAPTER 6. NUMERICAL MODELING OF FLAME PROPAGATION IN NANO-ALUMINUM-WATER MIXTURES

In this chapter, we try to address the fourth and final thesis question: *How to model flame propagation in realistic nanosuspensions by explicitly modeling particle thermal conductivity (with size effects and interfacial conductance)? What are the nanoscale heat transfer effects on combustion performance of nanoenergetic materials?* This chapter incorporates the nanoscale heat transfer effects introduced in Chapters 3-5 into a revised perspective about flame propagation in nanoenergetic materials. Based on the findings in prior chapters, an effective thermal conductivity model is developed for nano-aluminum/water (nAl-H₂O) mixture by considering the random distribution and viscous interaction of particles as described in Chapter 2. The developed thermal conductivity model is then validated by predicting the burning properties of a nAl-H₂O mixture. A detailed numerical analysis of flame propagation in nAl – water (H₂O) mixture is performed and emphasis is placed on investigating the role of particle thermal conductivity in predicting burning properties of the mixture. Flame structure and burning characteristics are obtained by solving the discretized energy equation using finite the Gauss-Seidel iteration method. The particle thermal conductivity is modeled using temperature-dependent thermal conductivities for both the aluminum core and the oxide layer, as well as considering interface resistance. The effective thermal conductivity of the mixture is modeled as a function of temperature, spatial coordinate, and local mixture composition by means of unified Maxwell-Eucken-Bruggeman model, accounting for random particle distribution and particle interaction.

6.1 Introduction

As discussed earlier, nAl is a promising fuel in energetic material compositions. Oxidizers considered here are oxygen, water, fluorine, nitrous oxide, carbon monoxide, and carbon dioxide. Table 6.1 shows the single-step balanced reactions of Al with various oxidizers and their equilibrium product compositions.

Table 6.1 Some prospective Al oxidation chemistries and equilibrium products

Reactants	Products
$2\text{Al(s)} + 1.5\text{O}_2$	Al, AlO, Al ₂ O, Al ₂ O ₂ , O, O ₂ , Al ₂ O ₃
$2\text{Al(s)} + 1.5(\text{O}_2 + 3.76\text{N}_2)$	Al, AlO, Al ₂ O, NO, N ₂ , O, Al ₂ O ₃ , AlN, AlON
$2\text{Al(s)} + 3\text{N}_2\text{O}$	Al, AlO, Al ₂ O, Al ₂ O ₂ , NO, N ₂ , O, O ₂ , Al ₂ O ₃
$2\text{Al(s)} + 3\text{H}_2\text{O}$	H, H ₂ , H ₂ O, Al(OH) ₃ , Al ₂ O ₃
$2\text{Al(s)} + 3\text{CO}_2$	CO, CO ₂ , Al ₂ O ₃
$2\text{Al(s)} + 3\text{CO}$	Al, Al ₂ O, CO, Al ₄ C ₃ , Al ₂ O ₃ , C
$2\text{Al(s)} + 1.5\text{F}_2$	Al, AlF, AlF ₂ , F

Among the different nAl chemistries, nAl-H₂O chemistry has been particularly attractive, due to several unique advantages. Firstly, it offers much cleaner combustion because of the less hazardous combustion products. Two of the particulate products are aluminum oxide (Al₂O₃) and aluminum hydroxide (Al(OH)₃) which are relatively inert and generally non-hazardous to plant and animal life. Moreover, owing to the high surface tension of nanoparticles, additional polymeric binders like HTPB and PBAN are not required to synthesize propellant mixtures. A lack of binders leads to elimination of a

significant amount of other combustion products that have been shown to be environmentally hazardous. Secondly, the Al–H₂O reaction liberates hydrogen gas from water, which can be used as secondary energy source in multistage propulsion systems, or for reducing less reactive metals from their ores, paving way for carbon-neutral metallurgical applications. Finally, all the constituents can be locally sourced, ensuring scalability and faster response in times of military emergencies. For these reasons, in the first decade of twenty-first century, nAl- H₂O reactions started gaining traction as propellant compositions, particularly nAl- water and nAl-ice (ALICE).

There have been several experimental and associated theoretical studies that investigate flame propagation in nAl suspensions [18, 19, 22]. Experimental studies span a pressure range of 0.1-10 MPa [22] and use particles of sizes 38-130 nm. The measured burning rates were found to be inversely proportional to particle size. This peculiar burning behavior was ascribed to both heat conduction and chemical kinetics, but the key mechanisms were not discussed. To complement their experiments, several theoretical studies were also performed [18]. All these studies adopted a modelling approach suited for micron-sized particle mixtures. They used approximate thermal transport property models that do not take TIR into consideration. In addition, the studies assume mean thermal properties and thermal conductivity in preheat and flame zones, while in reality these properties are temperature dependent and hence spatially varying. As a result, they have severely over predicted the linear burning rate, r_b in these systems.[18, 24] For instance, the mean error in r_b for a 130 nm particle is ~25%, while for a 80 nm particle, the error is 31%. For 38 nm particle suspensions, the predicted quantitative and qualitative trends differ substantially from experimental results. Furthermore, the mean error is > 50%,

with a peak error in r_b of 104% at 3.5 MPa. In these studies the authors attribute this error to the adsorption of water molecules to the nanoparticle surface, and argue that adsorption prevents the diffusion of oxidizer molecules towards the core Al atoms. While this is a plausible claim, recent studies [165] indicate that mass diffusion is not a rate limiting process in the combustion of nAl suspensions. Hence, we hypothesize that this disparity may occur due to an oversimplification of nanoscale heat conduction physics and inadequate modeling of the thermal conductivity of the system.

The primary objective of this chapter is therefore to systematically investigate the role of thermal resistance offered by Al, Al_2O_3 , and the interface in modeling effective thermal conductivity, and subsequently, flame propagation in nAl- H_2O mixture. Here, we use findings from Chapter 4 of TIR of Al/ Al_2O_3 for temperatures ranging from 300-1800 K, and the effective thermal conductivity of the suspension is modeled by accounting for the effect of particle size, temperature, and random dispersion of the mixture, as described in Chapter 2. Finally, the effective thermal conductivity model is applied in combination with the particle burning time scales to simulate a vertically propagating one dimensional flame in a stoichiometric mixture under isobaric conditions. Thermal properties are assumed to be spatially varying, and the nonlinear energy equation is solved iteratively. Linear burning rate, r_b is computed, and the effect of particle size is also assessed. Finally, the sensitivity of r_b to variations in transport properties are also analyzed to provide a heat conduction perspective to combustion of metal-based nano-energetic materials.

6.2 One-dimensional flame model and numerical framework

A one-dimensional, isobaric flame propagating vertically downward through a stoichiometric mixture of nAl particles and liquid water is considered. This model represents the real physical system on which combustion experiments were performed, and the results are available for validation [21]. A multi-zone framework representing the flame and preheat zones is shown in Figure 6.1.

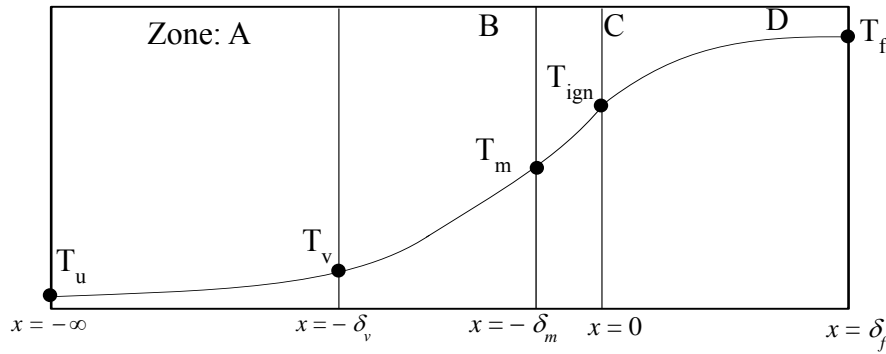


Figure 6.1 Theoretical multizone framework used to represent reaction and preheat zones. Zone A-C represent preheat zones and zone D represents the reaction zone.

As can be seen from Figure 6.1, several distinct zones can be identified within the framework. Zone A represents the nAl-H₂O (l) reactant mixture, which constitutes the propellant pellet originally synthesized for experimental study. The initial temperature of the unburnt propellant, T_u may be assumed to be equal to the ambient temperature i.e. $T_u = 298$ K. In Zone A, the major physical process is preheating of the system from T_u to the vaporization temperature of water, T_v and there are no notable chemical reactions in this zone due to the presence of a stable capping oxide layer. Once the water vaporizes at T_v , resulting vapor acts as an oxidizer in the following zones. The end of Zone B is marked by

the melting of the aluminum core at a temperature T_m . The melting of the aluminum core causes a volume expansion which cracks the oxide layer. Molecules diffuse through these cracks and react with the water vapor. Near the end of Zone B and throughout Zone C, ignition reactions occur. Marking the end of Zone C, at temperature $T_{ign} = 1360$ K, an overall ignition of the system is obtained. Zone D represents the flame zone leading to a flame temperature $T_f = 1800$ K.

The temperature profile, $T(x)$ and zone thicknesses, Δ can be obtained by solving the energy equation in each zone and matching the physical conditions at the boundaries. The general equation of the energy balance can be given as:

$$\frac{\partial}{\partial t}(\rho C_p T) = \frac{\partial}{\partial x} \left(k \frac{\partial T}{\partial x} \right) + \dot{Q}, \quad (6.1)$$

where, ρ is the density, C_p is the specific heat, T is the temperature, k is the effective thermal conductivity of the mixture, and \dot{Q} is the heat release rate. Note that ρ , C_p , and k are functions of temperature and local mixture composition. In a flame coordinate system, assuming constant r_b , the partial time derivative, $\frac{\partial}{\partial t}$ can be written as $r_b \frac{d}{dx}$ and Eq. 7 can be rewritten as:

$$r_b \frac{d}{dx}(\rho C_p T) = \frac{d}{dx} \left(k \frac{dT}{dx} \right) + \dot{Q} \quad (6.2)$$

The linear burning rate, r_b needs to be evaluated via the shooting method.[166] Therefore, the first step is to assume an initial solution for r_b . Neglecting the source term and expanding the right hand side of the eq. (8), the energy equation can be written as:

$$r_b \frac{d}{dx}(\rho C_p T) = \frac{dk}{dx} \cdot \frac{dT}{dx} + k \frac{d^2 T}{dx^2}. \quad (6.3)$$

Eq. (6.3) can be discretized by the one-dimensional finite difference method as:

$$r_b \frac{(\rho C_p T)_{i+1} - (\rho C_p T)_{i-1}}{2\Delta x} = \frac{k_{i+1} - k_{i-1}}{2\Delta x} \cdot \frac{T_{i+1} - T_{i-1}}{2\Delta x} + k_i \frac{T_{i+1} - 2T_i + T_{i-1}}{(\Delta x)^2}, \quad (6.4)$$

and solved using Gauss-Seidel iteration:

$$T_i^{n+1} = \frac{(\Delta x)^2}{2k_i} \left[\frac{k_{i+1}^n - k_{i-1}^n}{2\Delta x} \cdot \frac{T_{i+1}^n - T_{i-1}^n}{2\Delta x} + k_i \frac{T_{i+1}^n + T_{i-1}^n}{(\Delta x)^2} - r_b \frac{(\rho C_p T)_{i+1}^n - (\rho C_p T)_{i-1}^n}{2\Delta x} \right]. \quad (6.5)$$

Here i is the grid point index in the one-dimensional stencil consisting of r grid points, and n denotes the iteration. Note that the number of grid points should be chosen so as to include at the minimum a full nanoparticle and the surrounding fluid medium, so that the model is representative of the average mixture properties of the zone. If the grid size is smaller, then the effective thermal conductivity model fails for the control volume, leading to the failure of convergence of the iterative scheme. With the finite difference grid set up, the next step is to consider energy equations, identify boundary conditions, and perform the same numerical treatment for each zone present in the framework.

6.2.1 Energy balance for liquid water- solid aluminum (Zone A)

The liquid water zone is the region between $x = -\infty$ and $x = -\delta_v$. Here, the energy equation can be written as:

$$r_b \frac{d}{dx} \left[(\rho_{Al} C_{p,Al} \Phi_{Al} + \rho_{ox} C_{p,ox} \Phi_{ox} + \rho_{lw} C_{p,lw} \Phi_{lw}) T \right] = \frac{d}{dx} \left(k_m \frac{dT}{dx} \right), \quad (6.6)$$

where Φ is the volume fraction, subject to boundary conditions:

$T_{x \rightarrow -\infty} = T_u$; $T_{x=-\delta_v} = T_v$. Here, the subscripts *Al*, *ox*, *lw*, and *m*, *W* denote aluminum,

oxide layer, liquid water, and mixture in liquid water zone respectively. Assuming a zone

length of ~ 1000 cm, and an initial linear temperature profile between the boundary

conditions, $T_l = T_u$ and $T_{r+l} = T_{vap}$, Eq. 6.5 is solved iteratively at each grid point until a

steady state solution is obtained with a residual less than 1×10^{-3} . Once the solution is

obtained, the temperature gradient at A-B interface ($x = -\delta_v$), $\left. \frac{dT}{dx} \right|_w$ is calculated using a

second order one-sided backward finite difference scheme. Using $\left. \frac{dT}{dx} \right|_w$, the temperature

gradient on the vapor side, $\left. \frac{dT}{dx} \right|_v$ can be calculated as:

$$k_{m,AB+} \left. \frac{dT}{dx} \right|_v = k_{m,AB-} \left. \frac{dT}{dx} \right|_w + h_{fg} \Phi_{lw} \rho_{lw} r_b \quad (6.7)$$

where h_{fg} is the heat of vaporization of water, ρ_{lw} is the density of liquid water $T = T_{vap}$;

Φ_{vap} is the mass fraction of water in the mixture and $k_{m,AB-}$ and $k_{m,AB+}$ are the thermal

conductivities of the mixture to the left (liquid water) and right (vapor) of the phase

boundaries respectively at $T = T_{vap}$.

6.2.2 Energy balance for water vapor- solid aluminum (Zone B)

A water vapor-solid aluminum mixture exists in the region between $x = -\delta_v$ and $x = -\delta_m$.

The energy equation in this region can be written in following form:

$$r_b \frac{d}{dx} \left[(\rho_{Al} C_{p,Al} \Phi_{Al} + \rho_{ox} C_{p,ox} \Phi_{ox} + \rho_{lw} C_{p,wv} \Phi_{lw}) T \right] = \frac{d}{dx} \left(k_m \frac{dT}{dx} \right), \quad (6.8)$$

subject to the interfacial conditions:

$$\begin{cases} x = -\delta_v : T = T_v; k_{m+} \frac{dT}{dx} \Big|_v = k_{m-} \frac{dT}{dx} \Big|_w + h_{fg} \Phi_{lw} \rho_{lw} r_b, \\ x = -\delta_m : T = T_m, \end{cases} \quad (6.9)$$

where the subscripts - and + represent the right and left side of the boundary respectively.

For Zone B, in addition to solving the temperature profile, we need to simultaneously determine the zone thickness, Δ_{BC} . To do so, we first assume an initial zone thickness Δ_{BC} followed by a two-level iterative procedure – the inner level is to iteratively compute the temperature at each grid point using Eq. 6.5, and the outer level to correct the slope condition at the left boundary using a non-linear least square error minimization solver. The slope of the temperature profile at each outer step is computed from the converged temperature profile obtained from the inner step using a second order one-sided forward finite difference scheme. Once the converged zone thickness and corresponding temperature profile are simultaneously obtained, we can compute the heat flux at the right boundary and thereafter compute the incoming heat flux from zone C as:

$$k_{m,BC+} \frac{dT}{dx} \Big|_{v,BC+} = k_{m,BC-} \frac{dT}{dx} \Big|_{v,BC-} + h_{m-Al} \Phi_{Al} \rho_{Al} r_b \quad (6.10)$$

where h_{m-Al} is the heat of fusion of Al, ρ_{Al} is the density of solid Al at $T=T_m$, Φ_{Al} is the mass fraction of Al in the mixture and $k_{m,BC+}$ and $k_{m,BC-}$ are the thermal conductivities of the mixture corresponding to the left (solid Al) and right (molten Al) of the phase boundary respectively at $T=T_m$.

6.2.3 Energy balance for water vapor- molten aluminum (Zone C)

Similar to Zone B, the energy equation for Zone C can be written as:

$$r_b \frac{d}{dx} \left[\left(\rho_{lAl} C_{p,lAl} \Phi_{lAl} + \rho_{ox} C_{p,ox} \Phi_{ox} + \rho_{lw} C_{p,wv} \Phi_{lw} \right) T \right] = \frac{d}{dx} \left(k_m \frac{dT}{dx} \right), \quad (6.11)$$

subject to the boundary conditions:

$$\begin{cases} x = -\delta_m : T = T_m ; k_{m+} \frac{dT}{dx} \Big|_{V,mAl} = k_{m-} \frac{dT}{dx} \Big|_V + h_{mAl} \Phi_{Al} \rho_{Al} r_b, \\ x = 0 : T = T_{ign}, \end{cases} \quad (6.12)$$

where the subscript lAl represents liquid aluminum and h_{mAl} is the enthalpy of fusion of aluminum.

A similar procedure followed for Zone B is used to compute the temperature profile and zone thickness Δ_{CD} of zone C. The inner level computes the temperature profile for each estimate of zone thickness using Eq. 6.5 with $T_l = T_m$ and $T_{r+l} = T_{ign}$, and the outer level iteratively corrects the zone thickness to match the computed heat flux from the inner step temperature profile, with that obtained. Finally, from the converged zone thickness

and temperature profile, the heat flux at the C-D interface, $k_{m,CD-} \frac{dT}{dx} \Big|_{V,CD-}$ can be computed using a second order one-sided backward finite difference scheme. This heat flux is also equal to the heat flux coming in from the reaction zone D since there is no phase change associated with the C-D interface, i.e.:

$$k_{m,CD-} \frac{dT}{dx} \Big|_{V,CD-} = k_{m,CD+} \frac{dT}{dx} \Big|_{V,CD+} \quad (6.13)$$

6.2.4 Energy balance for reaction zone (Zone D)

The energy equation for Zone D can be expressed as:

$$r_b \frac{d}{dx} \left[\left(\sum_i \rho_i C_{p,i} \Phi_i \right) T \right] = \frac{d}{dx} \left(k \frac{dT}{dx} \right) + \frac{\rho_m Q_r}{\tau_b}, \quad (6.14)$$

where Q_r is the chemical energy release per unit mass of the mixture and τ_b the particle burning time scale. The inputs required to solve these equations are physical properties: ρ and C_p , particle burning time τ_b , and mixture thermal conductivity k_m .

The thermophysical (C_p and ρ) properties of aluminum and its oxide are taken from Refs. [31-33] and that of water and hydrogen are taken from Refs. [167, 168] The energy equation is modified to include the reaction source term and mean particle burning time as:

$$r_b \frac{d}{dx} (\rho C_p T) = \frac{dk_m}{dx} \left(\frac{\partial T}{\partial x} \right) + k_m \frac{d^2 T}{dx^2} + \frac{Q_r \rho_m}{\tau_b}, \quad (6.15)$$

where Q_r is the heat released by combustion per mass of stoichiometric mixture, ρ_m is the density of the mixture and τ_b is a burning time parameter to characterize the rate of reaction. Since a detailed reaction mechanism of Al-H₂O combustion is not well understood, we assume a mean mass burning time scale is justifiable, as long as the experimental mass burning properties can be properly reproduced. Therefore, particle burning time, τ_b , is obtained from experimental measurements [18, 27]. The mean particle burning time scale can be calculated from the following equation:

$$\tau_b = \frac{c[a_1 \exp(b_1 T) + a_2 \exp(b_2 T)]d_p^2}{p^m} \quad (6.16a)$$

$$m = a_3 \exp(b_3 T) + a_4 \exp(b_4 T) \quad (6.16b)$$

The numerical values corresponding to various constants are given in Table 6.2 Constants in eq. 6.16.

Table 6.2 Constants in eq. 6.16

Constant	Value
c	1.736×10^{-3}
a_1	204.650
b_1	-9.848×10^{-3}
a_2	1.842×10^{-4}
b_2	3.461×10^{-5}
a_3	7.075
b_3	-1.905×10^{-3}
a_4	4.023×10^{-1}
b_4	-3.120×10^{-4}

We have already observed the fidelity of the burning time model in reproducing the experimental burning times of nAl in Figure 1.6. Therefore, for solving the temperature profile and thickness of this zone, the boundary conditions are:

$$\begin{aligned} T_1 &= T_{ig} \\ T_{r+1} &= T_f \end{aligned} \quad (6.17)$$

$$\begin{aligned} \left. \frac{dT}{dx} \right|_{r+1} &= 0 \\ \left. \frac{dT}{dx} \right|_1 &= \left. \frac{dT}{dx} \right|_{CD+} . \end{aligned} \quad (6.19)$$

Note however that for solving for temperature profile, only two boundary conditions are required, and for determining the reaction zone thickness, only one additional boundary condition is required. The fourth boundary condition can be used to correct the r_b which was assumed at the very beginning of our calculations. Therefore, for Zone D, we follow a similar procedure as Zone B and C, using an inner step with Eqs. 6.17 and 6.18 to solve Eq. 6.15 to determine the temperature profile for a given zone thickness, and an outer step to correct the zone thickness based on Eq. 6.19. Finally, r_b is estimated by iteratively solving the above steps (zones) until Eq. 6.20 is satisfied.

6.3 Results

6.3.1 Thermal transport

In Chapter 4, we implemented ICMA calculations in an equilibrium molecular dynamics (EMD) framework for an Al/Al₂O₃ system to evaluate TIC, and have achieved

conclusive experimental validation for temperatures ranging from 50-500 K. Using the benchmarked ICMA framework, the TIC calculations was also extended to 1800 K. We considered a (111) Al || (0001) Al₂O₃ crystal direction representing the primary orientation in FCC metal-metal oxide interface for both Al- and O-terminated Al₂O₃ surfaces. Here, the inverse of TIC values is taken to evaluate TIR. Following ICMA calculations, a temperature dependent TIR model was also fitted to the data using a least squares algorithm.

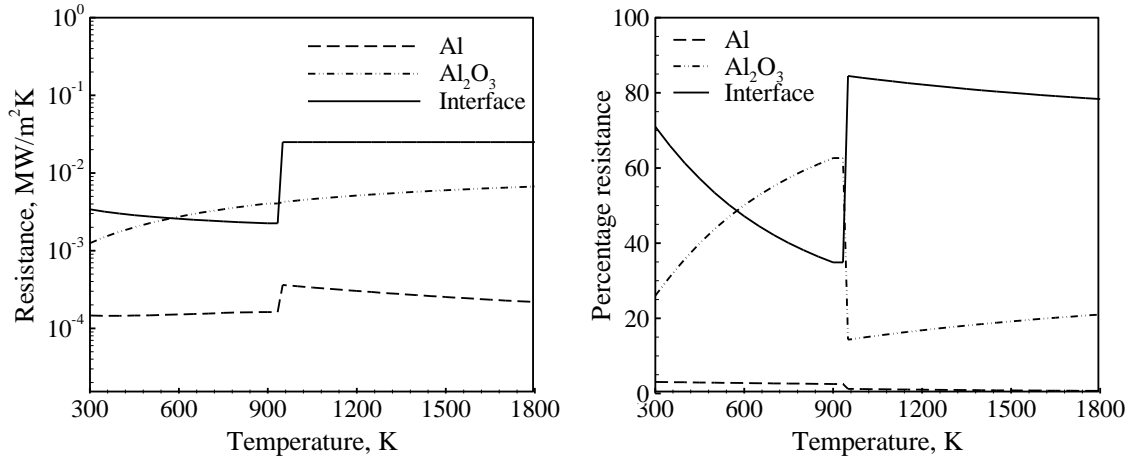


Figure 6.2 (a) Thermal resistance of Al, Al₂O₃, and interface (b) Percentage contribution by each resistance component to the total thermal resistance of the nanoparticle

Figure 6.2(a) shows the thermal resistance due to Al, Al₂O₃, and their interface, and Figure 6.2(b) shows the percentage contribution of each thermal resistance to total thermal resistance of the particle for temperatures ranging from 300-1800 K. The results correspond to a nanoparticle with a diameter of 38 nm coated by an oxide layer of initial thickness 2.7 nm, which increases as the reaction proceeds. As can be seen from Figure 6.2(a), the TIR decreases monotonically with temperature until reaching the melting temperature of Al = 933 K. At the melting temperature, there is a sharp rise in TIR, which remains nearly

constant thereafter. This is due to the loss of crystallinity of core Al lattice as it melts. The thermal resistance of Al_2O_3 , on the other hand, shows a monotonically increasing trend as it remains in solid state throughout the temperature range considered. Its increase is a combined result of the decrease in its thermal conductivity and the increase in oxide layer thickness. Also note that, for most temperatures, the TIR is higher than the Al_2O_3 resistance, indicating that TIR is crucial in accounting for the net thermal resistance of the nanoparticle. Moreover, from Figure 6.2(a), it is quite evident that the contribution to total resistance is the lowest from Al. The thermal resistance of Al is two orders of magnitude lower than that of Al_2O_3 and the interface. In other words, Al offers the highest conductive pathway for energy released at reaction zones to traverse through the unburnt mixture. Were the oxide layer absent on the Al surface, the medium would offer a much lower resistance to heat conduction, and would exhibit a much higher burning rate. In the liquid state, similar to the interface, Al offers significantly higher resistance due to lack of crystallinity. Furthermore from Figure 6.2(b), comparing the contribution of each of the components to total thermal resistance, it is evident that TIR and oxide layer resistance together contribute > 95% of thermal resistance. The same approach can be extended to various particle sizes and used in conjunction with the MEB model to predict thermal conductivity of the mixture.

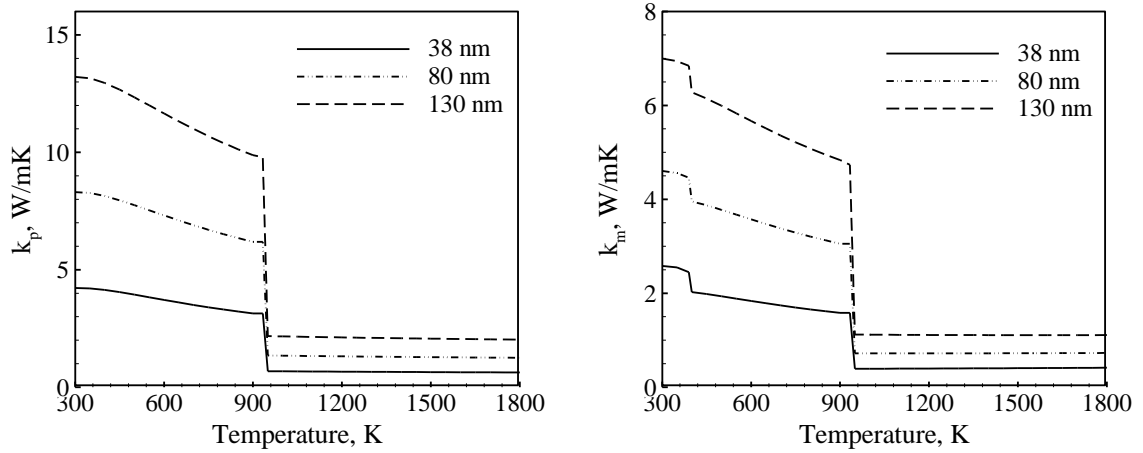


Figure 6.3 (a) Thermal conductivity of nanoparticles of diameters $D_p = 38$ nm, 80 nm, and 138 nm, and (b) Effective thermal conductivity of nAl-H₂O mixture for different particle sizes, as a function of temperature

Utilizing the temperature dependent thermal resistance values depicted in Figure 6.2(a), particle thermal conductivity, k_p for three different particle diameters D_p : 38 nm, 80 nm, and 138 nm are calculated. Figure 6.3(a) shows k_p as a function of temperature. As can be seen from the figure, k_p initially decreases steadily with temperature, drops sharply at the melting temperature of Al, and remains nearly constant thereafter. Using the particle and fluid thermal conductivities, effective thermal conductivity of the mixture, k_m can be evaluated using the MEB model. Results of the temperature dependent k_m for different particle sizes are shown in Fig. 6.3(b). In addition to the decreasing trend in k_m , two sharp drops are also observed corresponding to the vaporization temperature of water at 373 K and the melting point of Al respectively. More importantly, k_m increases with an increase in particle size because the thermal resistance of core Al decreases. Results shown in Fig. 6.3 are straightforward, and need to be validated against experimental measurements by applying the numerical framework to predict burning properties.

6.3.2 Flame propagation

A numerical solution of the flame problem yields the temperature profile across the reaction and preheat zones, as shown in Figure 6.4. Figure 5 represents zones A-D in the multizone framework corresponding to a baseline case of a 38 nm particle suspension at pressure, $P = 1$ bar. Results of r_b and the thicknesses of various zones are given in Table 1. The r_b predicted for the baseline case is 1.79 cm/s, and two distinct experimental measurements [21] give a value of ~ 1.61 cm/s and ~ 1.40 cm/s respectively. The error in predictions of r_b is $< 10\%$ compared with the experimental data, demonstrating the fidelity of the numerical framework. Prior theoretical studies [18] severely overpredict r_b to be 4.4 cm/s because they do not account for interface resistance and spatial variation of thermal transport properties. In addition, thicknesses of zones B, C, and D are also obtained as 4.7 μm , 1.01 μm , and 1.49 μm respectively. Zone thicknesses elucidate finer details of the flame structure that are difficult to measure experimentally. Also note that the slope of temperature profile increases at the A-B interface, accounting for the enthalpy of vaporization of water. A similar increase in slope is observed at B-C to account for enthalpy of fusion of Al. The end of zone D is marked by a slope of zero, corresponding to a constant flame temperature, T_f , as there is no heat transfer between reaction zone and products.

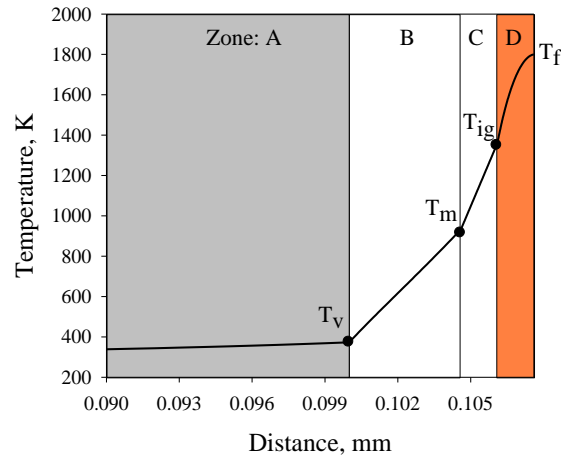


Figure 6.4 Detailed flame structure obtained via numerical solution of the 1D flame propagation problem clearly showing the different zones and their thicknesses

Table 6.3 Summary of results obtained from a numerical solution of flame structure and burning properties for the baseline case ($P = 1$ bar; $D_p = 38$ nm), compared with experimental results [19] and a prior theoretical model [18]

Linear burning rate, r_b	Zone B	Zone C	Zone D
This work = 1.79 cm/s	4.7 μm	1.01 μm	1.49 μm
Expt 1.: 1.61 cm/s [21, 22]			
Expt 2. :1.40 cm/s [21, 22]			
Prior work: 4.4 cm/s [18]			

Having benchmarked the numerical framework with baseline experimental results, a detailed analysis of r_b as a function of k_p modeled with increasing levels of complexity is studied. Figure 6.5 compares r_b predicted using 3 different k_p models at $P = 10$ bar. Model 1 includes only the thermal conductivity of Al, k_{Al} , to represent k_p . This model neglects the presence of oxide layer and, therefore over predicts the thermal conduction in the

nanoparticle. In model 2, the Al core and the oxide layer are considered, but TIR is neglected. Model 3 has the highest complexity wherein TIR is also used to model k_p . Experimentally measured r_b values are also overlaid for comparison [21]. As can be seen from Figure 6.5, predictions of model 3 are closest to the experimental values. Models 1 and 2 over predict r_b because they over predict thermal conductivity. The mean error in model 1 is ~20%, and is ~18% for model 2. The mean error in model 3 is < 5% and the maximum error in prediction is ~12% for $D_p = 38$ nm. A model fit on r_b v/s D_p predicted from model 3 obtained from least squares algorithm gives a relation: $r_b [\text{cm.s}^{-1}] = 144.76(D_p [\text{nm}])^{-1.0}$. Hence r_b is inversely proportional to D_p , which is also in accordance with the experimental measurements.

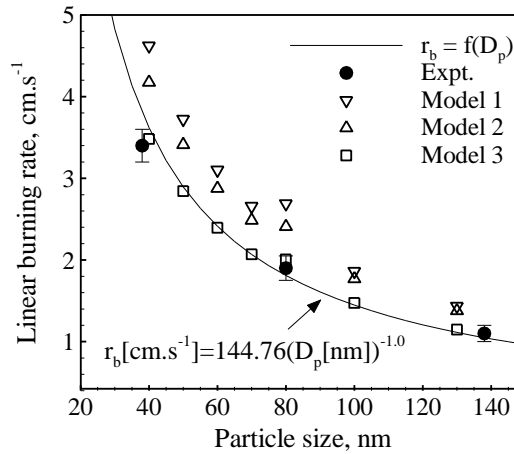


Figure 6.5 Linear burning rate as a function of particle diameter, illustrating how increasing levels of complexity in modeling particle thermal conductivity give better prediction of particle size dependent burning rates

Finally, we study the sensitivity of r_b to changes in thermal conductivity of Al and Al_2O_3 , and G at $P = 10$ bar. This study is motivated by recent advances in nanotechnology whereby thermal conductivity can be tuned by deliberately designing materials i.e. by

engineering features to target certain group of vibrational modes to either inhibit or enhance their role in heat conduction [169-171]. Tuning thermal conductivity provides a means to precisely control burning rates of energetic materials in propulsive missions. Here, the individual thermal conductivity components k_{Al} , G , and $k_{Al_2O_3}$ are arbitrarily varied with respect to their actual values and the effects on r_b are analyzed. Figure 6.6 depicts the sensitivity of r_b to changes in k_{Al} , G , and $k_{Al_2O_3}$ respectively.

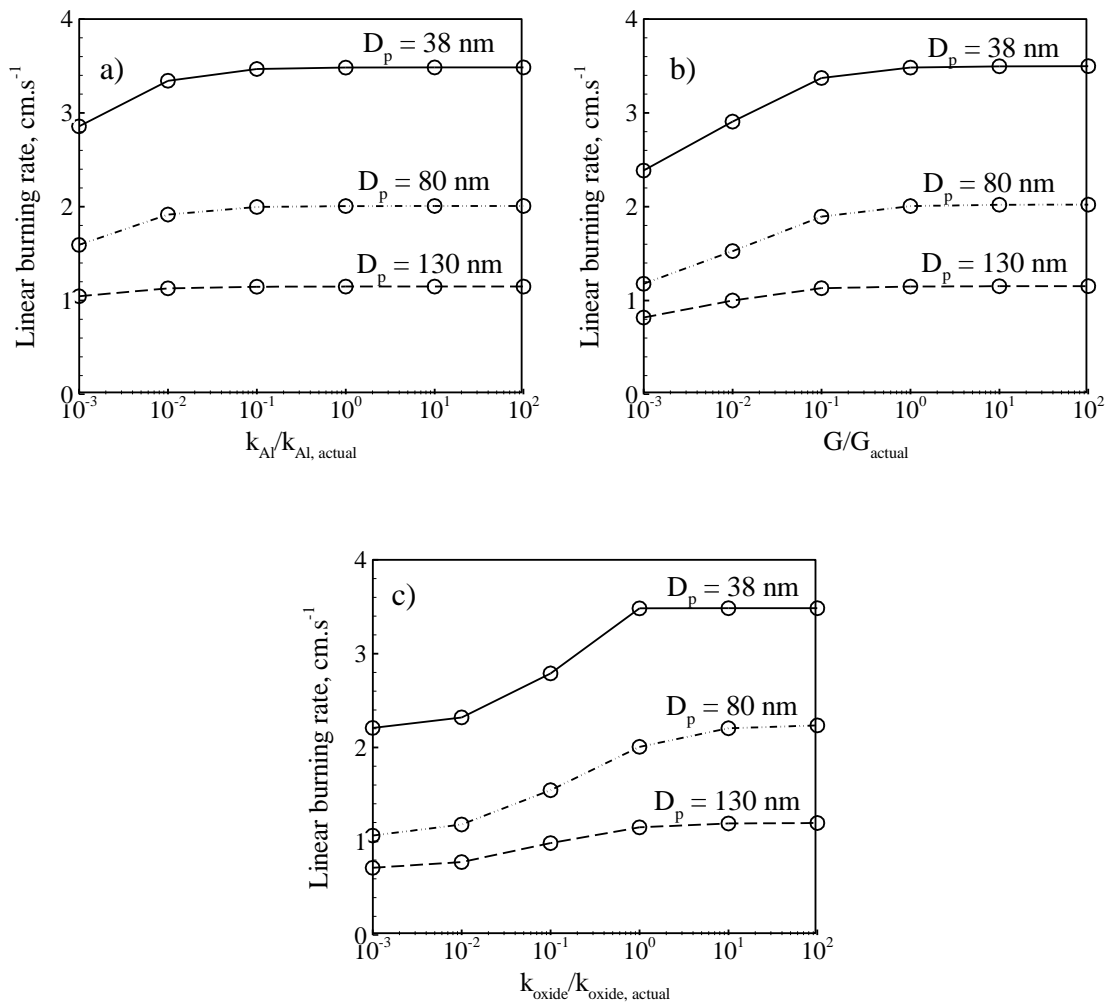


Figure 6.6 Sensitivity of linear burning rate to changes in thermal conductivity of a) Al and b) Al₂O₃, and c) thermal interfacial conductance, G for three different particle sizes

From Figure 6.6, it is evident that in general, r_b sensitivity is highest for 38 nm particle suspensions. From Figure 6.6 (a), it can be seen that for $D_p = 38$ nm, a reduction of k_{Al} by two orders of magnitude results in reduction in r_b by only $\sim 15\%$. Whereas Figure 6.6(b) indicates that for the same reduction in G , reduction in r_b is nearly $\sim 30\%$. Figure 6.6(c) shows that r_b drops by $\sim 34\%$ when $k_{Al_2O_3}$ decreases two orders of magnitude. It is therefore quite evident that thermal conductivity of oxide layer and interface conductance dictate r_b sensitivity. While $k_{Al_2O_3}$ seems to have the highest influence on r_b , it is also important to note that the oxide layer forms on particle surface *in situ* during the combustion process, and its thermal conductivity is practically uncontrollable. TIC, on the other hand, can be tuned to user requirements if certain vibrational modes in Al core are preferentially altered by means of nanoengineered defects, doping, and/or alloying. In other words, precise tuning of burning rate in nanoenergetic materials is theoretically achievable by careful consideration of interfacial conductance. However, as particles becomes larger, sensitivity of r_b to changes in k appears to diminish. Note also that for all particle sizes, even with several-fold enhancement in k and G , the effect on r_b is minimal. Therefore, to increase burning rates in nanoenergetic materials, one must also adopt conventional strategies like high pressure combustion, active metal coating, or catalysis to further improve reaction rates.

6.4 Conclusions

A detailed numerical analysis of flame propagation in nAl- H₂O mixtures was performed. Considering a multi-zone framework, the nonlinear energy equation is solved

iteratively using the Gauss-Seidel method. The thermal conductivity of nanoparticles is modeled by considering the thermal conductivities of both the aluminum and oxide layers, as well as TIR. Effective thermal conductivity of the mixture is modeled using the Maxwell-Eucken-Bruggeman model as a function of temperature, spatial coordinate, and local mixture composition. Results indicate that the oxide layer and the interface together constitute ~95% of the net thermal resistance of the nanoparticle. The effect of complexity in modeling particle thermal conductivity, k_p was studied by predicting the particle size dependent linear burning rate, r_b . Error in r_b prediction is lowest (< 5%) when TIR is taken into account. When interface resistance is neglected, error in r_b increases to 20%. Furthermore, r_b varies as the inverse of particle diameter, as observed in experimental measurements. Sensitivity of r_b to changes in thermal conductivities of aluminum (k_{Al}) and aluminum oxide ($k_{Al_2O_3}$), and interface conductance (G) is also studied for three particle sizes: 38 nm, 80 nm, and 138 nm. r_b sensitivity is the highest for 38 nm particles and decreases with increasing particle size. r_b drops by 15%, 30%, and 34% for a two orders of magnitude reduction in k_{Al} , G , and $k_{Al_2O_3}$ respectively. No notable enhancement in r_b is achieved by an enhancement in thermal conductivity or interface conductance.

CHAPTER 7. CONCLUSIONS AND FUTURE DIRECTIONS

7.1 Conclusions

This dissertation summarizes the nanoscale heat transfer effects on the combustion of metal-based nano-energetic materials. The investigation is carried out via a fundamental treatment of heat transport in nanoparticles and interfaces. First, *ab initio* and atomistic scale simulations were performed to investigate the nanoscopic nature of heat transport in bulk and nanosized aluminum and aluminum oxide, as well as at the interface of these materials. Atomistically informed macroscale modeling techniques were then employed to treat heat transport in mixtures of nanoparticles in liquid oxidizer to study combustion wave propagation. The key findings of this research are now summarized.

Firstly, a detailed analysis of phonon transport properties in aluminum (Al) and aluminum oxide (Al_2O_3) has been performed via lattice dynamics (LD) using input from density functional theory (DFT) calculations. The phonon dispersion relations and phonon density of states (DOS) are evaluated and compared with experimental data. DFT-LD methods accurately reproduce the transverse and longitudinal phonon branches in Al and Al_2O_3 along the edges of Brillouin zone. When compared with experimental data, the error in LD predictions is comparatively low. Predictions in phonon DOS via lattice dynamics is also exceptional. Two peaks in phonon density are observed in Al at ~ 3 and ~ 8.5 THz. When compared with neutron scattering experimental data, the lower frequency peak differs by ~ 1 THz whereas the higher frequency peak is reproduced accurately. For Al_2O_3 , however, the DFT-LD predictions of phonon DOS compares well with the neutron scattering data confirming that the phonon properties are well accounted for. Furthermore,

the temperature dependent phonon thermal conductivity (TC) of Al and Al₂O₃ are evaluated by solving the Boltzmann transport equation (BTE) under the relaxation time approximation (RTA). The phonon TC of Al calculated here is comparable to prior lattice dynamics calculations. Experimental data on phonon TC of Al is unavailable. Similarly, phonon TC of Al₂O₃ evaluated by LD is in accordance with experimental results. Furthermore, the thermal conductivity accumulation function was evaluated. Results suggest that for Al, phonon TC accumulates at a mean free path (MFP) of ~ 30 nm. This result suggests that if the system size is below 30 nm, phonon TC can be reduced as larger MFP phonons become inaccessible. For Al₂O₃, TC accumulates at a MFP of ~ 50 nm. Hence the system is more severely affected by size. Therefore, while modeling the thermal conductivity of a nanoparticle, the effect of particle size should be considered. Spectral distribution of TC was also analyzed. For Al, more than 80% of phonon thermal conductivity was due to phonons with frequencies in the range of 5-8 THz; for Al₂O₃, more than 92% of TC was due to phonons with frequencies in the range of 4-9 THz. Finally, the phonon lifetimes and mean free paths as a function of phonon frequencies were studied. Complementing the results of spectral distribution, highest phonon lifetimes and mean free paths were observed for phonons with frequencies 5-8 THz for Al and 4-8 THz for Al₂O₃. These studies provide a fundamental understanding of phonon frequencies and their contribution in pristine bulk Al and Al₂O₃ crystals.

Building on this understanding of thermal transport in bulk Al and Al₂O₃, the study was extended to understand heat transport across Al/Al₂O₃ interfaces. The thermal interfacial conductance (G) of the aluminum (Al)-aluminum oxide (α -Al₂O₃) interface along the crystal directions (111) Al || (0001) Al₂O₃ was accurately predicted. Two

fundamentally different formalisms were used to make these predictions in the temperature range 50-1800 K: interfacial conductance modal analysis (ICMA) and the atomistic green function (AGF) method. While AGF overpredicts G , predictions of ICMA show excellent agreement with experimental results both quantitatively and qualitatively. The ICMA formalism is clearly superior to PGM-based models due to its more fundamental treatment of the interfacial heat flux, its inclusion of full anharmonicity of vibrational modes, and for its ability to access to phonon mode level details.

Subsequently, to assess the role of dynamic heat transport mechanisms in nano-suspensions, a rigorous study of the effect of dynamic mechanisms of thermal conductivity enhancement was conducted. An alternative explanation to the unusually high thermal conductivity of nano-suspensions obtained using Green-Kubo relations is provided. While prior studies credit these enhancements to dynamic heat transport mechanisms, our results suggest that these high values are merely an outcome of artificial correlations, arising from single nanoparticle systems and periodic boundary conditions, thereby contaminating the heat current autocorrelation function (HCACF). This problem is expected to be prominent for systems in which vibration frequencies of the constituents are disparate. In such cases, low frequency perturbations are transmitted through the surrounding high frequency medium and return to the originating particle due to periodic boundary conditions. The resulting circular resonance contaminates the HCACF, which is more pronounced for smaller particles and/or higher volume fractions. To alleviate this artifact, multi-particle systems are considered. The presence of additional particles impedes the development of artificial self-correlations by breaking the particle-image symmetry. Thermal conductivity predicted from the rectified HCACF is in good agreement with experimental data and the

Maxwell model predictions. In other words, the role of nanolayer in thermal conductivity enhancement is found to be insignificant as there is no thermal conductivity enhancement beyond the Maxwell model.

Finally, building on the knowledge of nanoscale heat transport properties, a heat conduction perspective to flame propagation in nanoenergetic materials is developed. A detailed numerical analysis of flame propagation in nano-aluminum (nAl) - water (H_2O) mixtures is performed. Considering a multi-zone framework, the nonlinear energy equation is solved iteratively using the Gauss-Seidel method. Thermal conductivity of nanoparticles is modeled using thermal conductivities of aluminum and oxide layer, as well as TIR. The effective thermal conductivity of the mixture is modeled using the Maxwell-Eucken-Bruggeman model as a function of temperature, spatial coordinate, and local mixture composition. Results indicate that the oxide layer and the interface together constitute 95% of the net thermal resistance of the nanoparticle. The effect of complexity in modeling particle thermal conductivity, k_p was studied by predicting the particle size dependent linear burning rate, r_b . Error in r_b is lowest ($< 5\%$) when interface resistance is included in modeling k_p . When interface resistance is neglected, the error in r_b increases to 20%. Furthermore, r_b varies as the inverse of particle diameter, as observed in experimental measurements. Sensitivity of r_b to changes in thermal conductivities of aluminum (k_{Al}) and aluminum oxide ($k_{Al_2O_3}$), and interface conductance (G) is also studied for three particle sizes: 38 nm, 80 nm, and 138 nm. r_b sensitivity is the highest for 38 nm particles and decreases with increasing particle size. r_b decreases by 15%, 30%, and 34% for a two orders of magnitude reduction in k_{Al} , G , and $k_{Al_2O_3}$ respectively. No notable enhancement in r_b is achieved by an enhancement in thermal conductivity or interface conductance.

In summary, we have investigated the nanoscale heat transfer effects in the combustion of nanoenergetic materials in depth, from the first principles. The numerical simulation techniques developed, and the insights gained as a part of this research can be applied to a broader class of nanoenergetic materials to study their combustion performance following a similar treatment. Understanding the origin of heat conduction in such materials can suggest methods to tune their thermal conductivity. Tuning thermal conductivity provides means to precisely control burning rates of nanoenergetic materials in propulsive missions.

7.2 Recommendations for future work

Investigation of heat conduction in engineered surfaces and interfaces is an interesting topic for future research. Engineered surfaces are deliberately grafted with molecules used to precisely control interfacial heat conduction. For instance, it is known that aluminum when coated with active metals such as nickel (Ni) and palladium (Pd) reduces oxide layer formation, and also facilitates inter-metallic reactions thereby improving the overall energetic value of the mixture. Heat conduction across Al-Ni and Al-Pd interfaces, however, is not understood well. In addition, grafting functional groups like $-OH$, $-F$, $-N$, and $-COOH$ to aluminum surface can also alter the interfacial conductance. These cases are to be investigated thoroughly in future.

Leveraging on the knowledge gained from heat transport in engineered surfaces and interfaces, smart functional nanoenergetic materials can be designed from the first principles. Smart functional nanoenergetic materials can be used in futuristic space and

underwater propulsion systems, standalone power source for deep sea and forest explorations, etc. Moreover, exploiting heat conduction pathways to switch on/off combustion: stress/strain regulated thermal conductivity, interfacial heat conduction, structural considerations, porosity, dimensionality, etc. are exciting areas of future research.

The current dissertation introduces a robust one dimensional finite difference solver for flame propagation. In future, better computational models incorporated with detailed chemistry, transient flame models in two and three dimensions to simulate realistic flames may be developed. These models may also be incorporated with molecular dynamics codes to facilitate on-the-fly thermal transport property evaluations.

APPENDIX A. FREE PARAMETERS OF EMPIRICAL POTENTIAL FUNCTIONS

Table A.1 Interatomic potential parameters for Vashishta potential for Al₂O₃ [76]

	Al	O					
Z_i (e)	1.5237	-1.0158					
$\lambda = 5.0 \text{ \AA}$	$\xi = 3.75 \text{ \AA}$	$r_c = 6.0 \text{ \AA}$				$e = 1.602 \times 10^{-19} \text{ C}$	
Two-body term							
	Al-Al	Al-O	O-O				
η_{ij}	7	9	7				
$H_{ij} (\text{eV}\text{\AA}^\eta)$	12.7506	249.3108	564.7334				
$D_{ij} (\text{eV}\text{\AA}^4)$	0	50.1522	44.5797				
$W_{ij} (\text{eV}\text{\AA}^6)$	0	0	79.2884				
Three-body term							
	$B_{jik} (\text{eV})$	$\bar{\theta}_{jik}$	C_{jik}	$\gamma (\text{\AA})$	$r_o (\text{\AA})$		
Al-O-Al	8.1149	109.47	10	1.0	2.90		
O-Al-O	12.4844	90.00	10	1.0	2.90		

Table A.2 Interatomic potential parameters for Streitz-Mintmire potential for Al and Al₂O₃ [78]

Atomic parameters						
	λ (eV)	J (eV)	ζ (\AA^{-1})	Z	A (eV)	ξ
Al	0.000	10.328	0.968	0.746	0.763	0.147
O	5.484	14.035	2.143	0.000	2.116	1.000
Pair parameters						
	$r^*(\text{\AA})$	α (\AA^{-1})	β (\AA^{-1})	B (eV)	C (eV)	
Al-Al	3.365	1.767	2.017	0.075	0.159	
O-O	2.005	8.389	6.871	1.693	1.865	
Al-O	2.358	4.233	4.507	0.154	0.094	

APPENDIX B. COMPARISON OF PHONON PROPERTIES
CALCULATED FROM LD CALCULATION USING STREITZ-
MINTMIRE (SM) POTENTIAL AND DFT

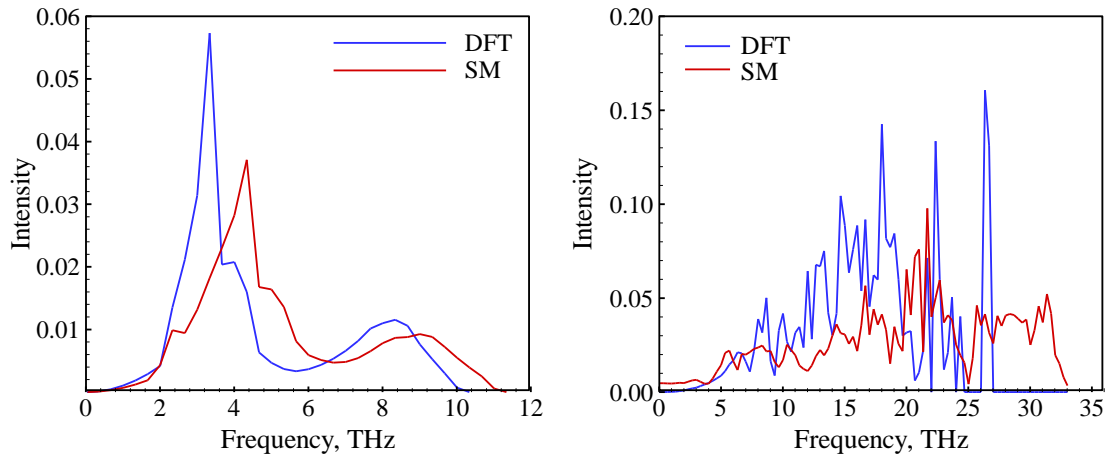


Figure B.1 Comparison of phonon DOS evaluated using SM potential and DFT for a) Al and b) Al₂O₃

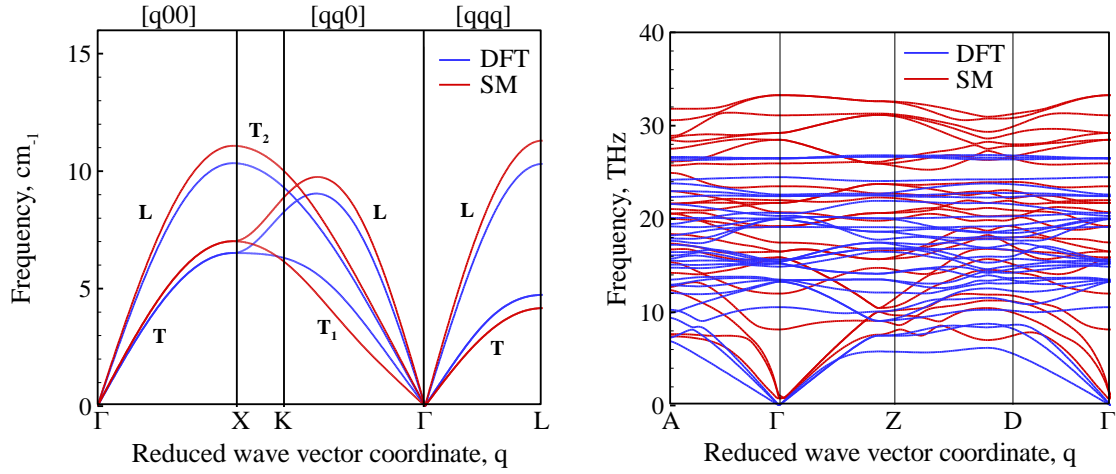


Figure B.2 Comparison of dispersion relations evaluated using SM potential and DFT for a) Al and b) Al_2O_3

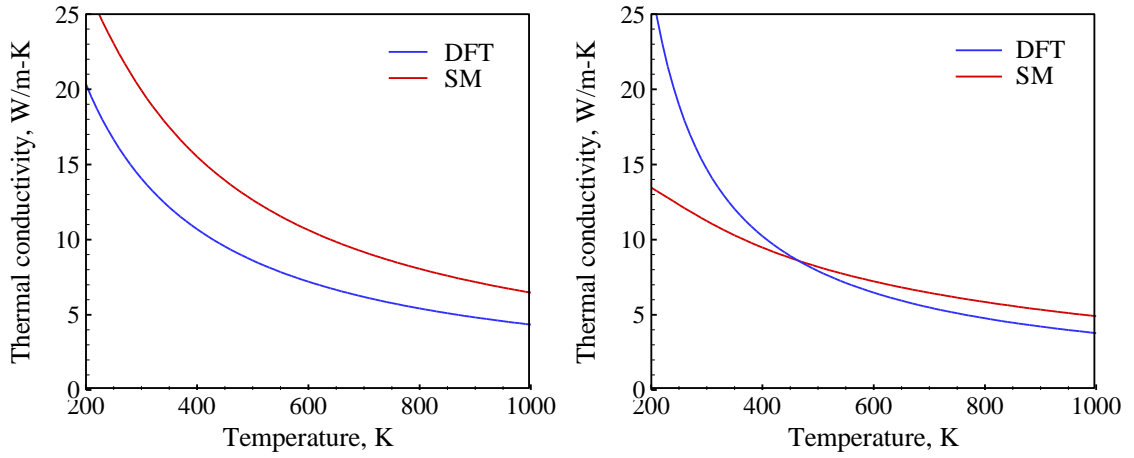


Figure B.3 Comparison of phonon thermal conductivity evaluated using SM potential and DFT for a) Al and b) Al_2O_3

REFERENCES

1. Beck, M.P., et al., *The effect of particle size on the thermal conductivity of alumina nanofluids*. Journal of Nanoparticle Research, 2009. **11**(5): p. 1129-1136.
2. Timofeeva, E.V., et al., *Thermal conductivity and particle agglomeration in alumina nanofluids: experiment and theory*. Physical Review E, 2007. **76**(6): p. 061203.
3. Tillotson, T., et al., *Nanostructured energetic materials using sol-gel methodologies*. Journal of Non-Crystalline Solids, 2001. **285**(1): p. 338-345.
4. Son, S.F., R. Yetter, and V. Yang, *Introduction: nanoscale composite energetic materials*. Journal of Propulsion and Power, 2007. **23**(4): p. 643-644.
5. Yang, V., *Solid Propellant Chemistry Combustion and Motor Interior Ballistics 1999*. Vol. 185. 2000: Aiaa.
6. Dreizin, E.L., *Metal-based reactive nanomaterials*. Progress in Energy and Combustion Science, 2009. **35**(2): p. 141-167.
7. Dokhan, A., et al., *The effects of bimodal aluminum with ultrafine aluminum on the burning rates of solid propellants*. Proceedings of the Combustion Institute, 2002. **29**(2): p. 2939-2946.
8. Price, E., et al., *Combustion of ammonium perchlorate-polymer sandwiches*. AIAA Journal, 1981. **19**(3): p. 380-386.
9. Starkovich, J., S. Adams, and B. Palaszewski, *Nanoparticulate gellants for metallized gelled liquid hydrogen with aluminum*. NASA Tech. Memo, 1996. **107280**: p. 1-3.
10. Gan, Y., Y.S. Lim, and L. Qiao, *Combustion of nanofluid fuels with the addition of boron and iron particles at dilute and dense concentrations*. Combustion and Flame, 2012. **159**(4): p. 1732-1740.
11. Sundaram, D., V. Yang, and R.A. Yetter, *Metal-based nanoenergetic materials: Synthesis, properties, and applications*. Progress in Energy and Combustion Science, 2017. **61**: p. 293-365.
12. Yetter, R.A., G.A. Risha, and S.F. Son, *Metal particle combustion and nanotechnology*. Proceedings of the Combustion Institute, 2009. **32**(2): p. 1819-1838.
13. Puri, P. and V. Yang, *Effect of particle size on melting of aluminum at nano scales*. The Journal of Physical Chemistry C, 2007. **111**(32): p. 11776-11783.

14. Park, K., et al., *Size-resolved kinetic measurements of aluminum nanoparticle oxidation with single particle mass spectrometry*. The journal of physical chemistry B, 2005. **109**(15): p. 7290-7299.
15. Sundaram, D.S., P. Puri, and V. Yang, *Pyrophoricity of nascent and passivated aluminum particles at nano-scales*. Combustion and Flame, 2013. **160**(9): p. 1870-1875.
16. Sabourin, J.L., R.A. Yetter, and V.S. Parimi, *Exploring the effects of nanostructured particles on liquid nitromethane combustion*. Journal of Propulsion and Power, 2010. **26**(5): p. 1006-1015.
17. Sabourin, J.L., et al., *Functionalized graphene sheet colloids for enhanced fuel/propellant combustion*. ACS nano, 2009. **3**(12): p. 3945-3954.
18. Sundaram, D.S., et al., *Effects of particle size and pressure on combustion of nano-aluminum particles and liquid water*. Combustion and Flame, 2013. **160**(10): p. 2251-2259.
19. Risha, G.A., et al., *Combustion of frozen nanoaluminum and water mixtures*. Journal of Propulsion and Power, 2013. **30**(1): p. 133-142.
20. Huang, Y., et al., *Effect of particle size on combustion of aluminum particle dust in air*. Combustion and Flame, 2009. **156**(1): p. 5-13.
21. Risha, G.A., et al., *Combustion and conversion efficiency of nanoaluminum-water mixtures*. Combustion Science and Technology, 2008. **180**(12): p. 2127-2142.
22. Risha, G.A., et al., *Combustion of nano-aluminum and liquid water*. Proceedings of the Combustion Institute, 2007. **31**(2): p. 2029-2036.
23. Sundaram, D., V. Yang, and V. Zarko, *Combustion of nano aluminum particles*. Combustion, Explosion, and Shock Waves, 2015. **51**(2): p. 173-196.
24. Sundaram, D.S. and V. Yang, *Effect of packing density on flame propagation of nickel-coated aluminum particles*. Combustion and Flame, 2014. **161**(11): p. 2916-2923.
25. Sundaram, D.S., P. Puri, and V. Yang, *A general theory of ignition and combustion of nano-and micron-sized aluminum particles*. Combustion and Flame, 2016. **169**: p. 94-109.
26. Tyagi, H., et al., *Increased hot-plate ignition probability for nanoparticle-laden diesel fuel*. Nano letters, 2008. **8**(5): p. 1410-1416.
27. Bazyn, T., H. Krier, and N. Glumac, *Combustion of nanoaluminum at elevated pressure and temperature behind reflected shock waves*. Combustion and Flame, 2006. **145**(4): p. 703-713.

28. Maxwell, J.C., *A treatise on electricity and magnetism*. Vol. 1. 1881: Clarendon press.
29. Eucken, A., *Allgemeine gesetzmäßigkeiten für das wärmeleitvermögen verschiedener stoffarten und aggregatzustände*. Forschung auf dem Gebiet des Ingenieurwesens A, 1940. **11**(1): p. 6-20.
30. Bruggeman, V.D., *Berechnung verschiedener physikalischer Konstanten von heterogenen Substanzen. I. Dielektrizitätskonstanten und Leitfähigkeiten der Mischkörper aus isotropen Substanzen*. Annalen der physik, 1935. **416**(8): p. 665-679.
31. Gale, W. and T. Totemeier, *Smithells Metals Reference Book" eight edition*, Amsterdam, Boston, Heidelberg, London, New York. 2004, Oxford, Paris, San Diego, San Francisco, Singapore, Sydney, Tokyo.
32. Buyco, E.H. and F.E. Davis, *Specific heat of aluminum from zero to its melting temperature and beyond. Equation for representation of the specific heat of solids*. Journal of Chemical and engineering data, 1970. **15**(4): p. 518-523.
33. MUNRO, M., *Evaluated Material Properties for a Sintered alpha-Alumina*. Journal of the American Ceramic Society, 1997. **80**(8): p. 1919-1928.
34. Hopkins, P.E., et al., *Influence of anisotropy on thermal boundary conductance at solid interfaces*. Physical Review B, 2011. **84**(12): p. 125408.
35. Stoner, R. and H. Maris, *Kapitza conductance and heat flow between solids at temperatures from 50 to 300 K*. Physical Review B, 1993. **48**(22): p. 16373.
36. Koblinski, P., et al., *Mechanisms of heat flow in suspensions of nano-sized particles (nanofluids)*. International journal of heat and mass transfer, 2002. **45**(4): p. 855-863.
37. Lee, S., et al., *Molecular dynamic simulation: Studying the effects of Brownian motion and induced micro-convection in nanofluids*. Numerical Heat Transfer, Part A: Applications, 2016. **69**(6): p. 643-658.
38. Li, L., et al., *Molecular dynamics simulation of effect of liquid layering around the nanoparticle on the enhanced thermal conductivity of nanofluids*. Journal of nanoparticle research, 2010. **12**(3): p. 811-821.
39. Özerinç, S., S. Kakaç, and A.G. Yazıcıoğlu, *Enhanced thermal conductivity of nanofluids: a state-of-the-art review*. Microfluidics and Nanofluidics, 2010. **8**(2): p. 145-170.
40. Sachdeva, P. and R. Kumar, *Effect of hydration layer and surface wettability in enhancing thermal conductivity of nanofluids*. Applied Physics Letters, 2009. **95**(22): p. 223105.

41. Das, S.K., et al., *Temperature dependence of thermal conductivity enhancement for nanofluids*. Journal of Heat Transfer, 2003. **125**(4): p. 567-574.
42. Babaei, H., P. Keblinski, and J. Khodadadi, *A proof for insignificant effect of Brownian motion-induced micro-convection on thermal conductivity of nanofluids by utilizing molecular dynamics simulations*. Journal of Applied Physics, 2013. **113**(8): p. 084302.
43. Babaei, H., P. Keblinski, and J.M. Khodadadi, *Equilibrium molecular dynamics determination of thermal conductivity for multi-component systems*. Journal of Applied Physics, 2012. **112**(5): p. 054310.
44. Keblinski, P., R. Prasher, and J. Eapen, *Thermal conductance of nanofluids: is the controversy over?* Journal of Nanoparticle research, 2008. **10**(7): p. 1089-1097.
45. Chen, G., *Nanoscale Energy Transport and Conversion: A Parallel Treatment of Electrons, Molecules, Phonons, and Photons*. 2005: Oxford University Press.
46. Zhang, Z.M., *Nano/microscale heat transfer*. 2007: McGraw-Hill New York.
47. Chen, G., *Phonon heat conduction in nanostructures I*. International journal of thermal sciences, 2000. **39**(4): p. 471-480.
48. Chen, G., *Particularities of heat conduction in nanostructures*. Journal of Nanoparticle Research, 2000. **2**(2): p. 199-204.
49. Kittel, C., *Introduction to solid state physics*. Vol. 8. 1976: Wiley New York.
50. Jain, A. and A.J. McGaughey, *Thermal transport by phonons and electrons in aluminum, silver, and gold from first principles*. Physical Review B, 2016. **93**(8): p. 081206.
51. Hopkins, P.E., et al., *Temperature-Dependent Thermal Boundary Conductance at Al/Al₂O₃ and Pt/Al₂O₃ Interfaces*. International Journal of Thermophysics, 2007. **28**(3): p. 947-957.
52. Yu, W. and S. Choi, *The role of interfacial layers in the enhanced thermal conductivity of nanofluids: a renovated Maxwell model*. Journal of Nanoparticle Research, 2003. **5**(1-2): p. 167-171.
53. Shaker, M., E. Birgersson, and A. Mujumdar, *Extended Maxwell model for the thermal conductivity of nanofluids that accounts for nonlocal heat transfer*. International Journal of Thermal Sciences, 2014. **84**: p. 260-266.
54. Leong, K., C. Yang, and S. Murshed, *A model for the thermal conductivity of nanofluids—the effect of interfacial layer*. Journal of nanoparticle research, 2006. **8**(2): p. 245-254.

55. Xie, H., et al., *Nanofluids containing multiwalled carbon nanotubes and their enhanced thermal conductivities*. Journal of Applied Physics, 2003. **94**(8): p. 4967-4971.
56. Eapen, J., J. Li, and S. Yip, *Mechanism of thermal transport in dilute nanocolloids*. Physical review letters, 2007. **98**(2): p. 028302.
57. Xue, L., et al., *Effect of liquid layering at the liquid–solid interface on thermal transport*. International Journal of Heat and Mass Transfer, 2004. **47**(19): p. 4277-4284.
58. Liang, Z. and H.-L. Tsai, *Thermal conductivity of interfacial layers in nanofluids*. Phys Rev E, 2011. **83**: p. 41602.
59. Einstein, A., *Investigations on the Theory of the Brownian Movement*. 1956: Courier Corporation.
60. Prasher, R., P. Bhattacharya, and P.E. Phelan, *Thermal conductivity of nanoscale colloidal solutions (nanofluids)*. Physical review letters, 2005. **94**(2): p. 025901.
61. Bhattacharya, P., et al., *Brownian dynamics simulation to determine the effective thermal conductivity of nanofluids*. Journal of Applied Physics, 2004. **95**(11): p. 6492-6494.
62. Sarkar, S. and R.P. Selvam, *Molecular dynamics simulation of effective thermal conductivity and study of enhanced thermal transport mechanism in nanofluids*. Journal of applied physics, 2007. **102**(7): p. 074302.
63. Evans, W., J. Fish, and P. Keblinski, *Role of Brownian motion hydrodynamics on nanofluid thermal conductivity*. Applied Physics Letters, 2006. **88**(9): p. 093116.
64. Pilania, G., et al., *Revisiting the Al/Al₂O₃ interface: coherent interfaces and misfit accommodation*. Scientific reports, 2014. **4**: p. 4485.
65. Yang, W. and P.W. Ayers, *Density-functional theory*, in *Computational Medicinal Chemistry for Drug Discovery*. 2003, CRC Press. p. 103-132.
66. Dove, M.T., *Introduction to Lattice Dynamics*. 1993: Cambridge University Press.
67. Allen, M.P. and D.J. Tildesley, *Computer simulation of liquids*. 2017: Oxford university press.
68. Ercolessi, F., *A molecular dynamics primer*. Spring college in computational physics, ICTP, Trieste, 1997. **19**.
69. Born, M. and R. Oppenheimer, *Zur quantentheorie der molekeln*. Annalen der Physik, 1927. **389**(20): p. 457-484.

70. Kohn, W. and L.J. Sham, *Self-consistent equations including exchange and correlation effects*. Physical review, 1965. **140**(4A): p. A1133.
71. Giannozzi, P., et al., *QUANTUM ESPRESSO: a modular and open-source software project for quantum simulations of materials*. Journal of physics: Condensed matter, 2009. **21**(39): p. 395502.
72. Perdew, J.P. and Y. Wang, *Accurate and simple analytic representation of the electron-gas correlation energy*. Physical Review B, 1992. **45**(23): p. 13244.
73. Plimpton, S., *Fast parallel algorithms for short-range molecular dynamics*. Journal of computational physics, 1995. **117**(1): p. 1-19.
74. Rohskopf, A., et al., *Empirical interatomic potentials optimized for phonon properties*. NPJ Computational Materials, 2017. **3**: p. 1.
75. Mark, P. and L. Nilsson, *Structure and dynamics of the TIP3P, SPC, and SPC/E water models at 298 K*. The Journal of Physical Chemistry A, 2001. **105**(43): p. 9954-9960.
76. Vashishta, P., et al., *Interaction potentials for alumina and molecular dynamics simulations of amorphous and liquid alumina*. Journal of Applied Physics, 2008. **103**(8): p. 083504.
77. Zope, R.R. and Y. Mishin, *Interatomic potentials for atomistic simulations of the Ti-Al system*. Physical Review B, 2003. **68**(2): p. 024102.
78. Streitz, F. and J. Mintmire, *Electrostatic potentials for metal-oxide surfaces and interfaces*. Physical Review B, 1994. **50**(16): p. 11996.
79. Allen, M.P. and D.J. Tildesley, *Computer simulation of liquids*. 1989: Oxford university press.
80. Kubo, R., *The fluctuation-dissipation theorem*. Reports on progress in physics, 1966. **29**(1): p. 255.
81. Hardy, R.J., *Energy-flux operator for a lattice*. Physical Review, 1963. **132**(1): p. 168.
82. McGaughey, A. and M. Kaviani, *Thermal conductivity decomposition and analysis using molecular dynamics simulations. Part I. Lennard-Jones argon*. International Journal of Heat and Mass Transfer, 2004. **47**(8): p. 1783-1798.
83. McGaughey, A. and M. Kaviani, *Thermal conductivity decomposition and analysis using molecular dynamics simulations: Part II. Complex silica structures*. International Journal of Heat and Mass Transfer, 2004. **47**(8): p. 1799-1816.

84. Evans, W., J. Fish, and P. Keblinski, *Thermal conductivity of ordered molecular water*. The Journal of chemical physics, 2007. **126**(15): p. 154504.
85. Lv, W. and A. Henry, *Phonon transport in amorphous carbon using Green–Kubo modal analysis*. Applied Physics Letters, 2016. **108**(18): p. 181905.
86. Larkin, J., et al., *Comparison and evaluation of spectral energy methods for predicting phonon properties*. Journal of Computational and Theoretical Nanoscience, 2014. **11**(1): p. 249-256.
87. Tadano, T. and S. Tsuneyuki, *Self-consistent phonon calculations of lattice dynamical properties in cubic SrTiO₃ with first-principles anharmonic force constants*. Physical Review B, 2015. **92**(5): p. 054301.
88. Tadano, T., Y. Gohda, and S. Tsuneyuki, *Anharmonic force constants extracted from first-principles molecular dynamics: applications to heat transfer simulations*. Journal of Physics: Condensed Matter, 2014. **26**(22): p. 225402.
89. Jain, A., *Thermal Transport in Semiconductors and Metals from First-Principles*. 2015.
90. McGaughey, A.J.H. and M. Kaviani, *Quantitative validation of the Boltzmann transport equation phonon thermal conductivity model under the single-mode relaxation time approximation*. Physical Review B, 2004. **69**(9): p. 094303.
91. Barrat, J.-L. and F. Chiaruttini, *Kapitza resistance at the liquid—solid interface*. Molecular Physics, 2003. **101**(11): p. 1605-1610.
92. Domingues, G., et al., *Heat transfer between two nanoparticles through near field interaction*. Physical review letters, 2005. **94**(8): p. 085901.
93. Zhou, X.F. and L. Gao, *Effective thermal conductivity in nanofluids of nonspherical particles with interfacial thermal resistance: differential effective medium theory*. Journal of applied physics, 2006. **100**(2): p. 024913.
94. Nan, C.-W., et al., *Effective thermal conductivity of particulate composites with interfacial thermal resistance*. Journal of Applied Physics, 1997. **81**(10): p. 6692-6699.
95. Muraleedharan, M.G., et al., *Thermal conductivity calculation of nano-suspensions using Green–Kubo relations with reduced artificial correlations*. Journal of Physics: Condensed Matter, 2017. **29**(15): p. 155302.
96. Wang, J., et al., *A new approach to modelling the effective thermal conductivity of heterogeneous materials*. International journal of heat and mass transfer, 2006. **49**(17-18): p. 3075-3083.

97. Wang, Y., Z. Lu, and X. Ruan, *First principles calculation of lattice thermal conductivity of metals considering phonon-phonon and phonon-electron scattering*. Journal of Applied Physics, 2016. **119**(22): p. 225109.
98. Perdew, J.P. and A. Zunger, *Self-interaction correction to density-functional approximations for many-electron systems*. Physical Review B, 1981. **23**(10): p. 5048.
99. Stedman, R.t. and G. Nilsson, *Dispersion relations for phonons in aluminum at 80 and 300 K*. Physical Review, 1966. **145**(2): p. 492.
100. Schober, H., D. Strauch, and B. Dorner, *Lattice dynamics of sapphire (Al₂O₃)*. Zeitschrift für Physik B Condensed Matter, 1993. **92**(3): p. 273-283.
101. Powell, R., C.Y. Ho, and P.E. Liley, *Thermal conductivity of selected materials*. 1966, DTIC Document.
102. Ramires, M.L., et al., *Standard reference data for the thermal conductivity of water*. Journal of Physical and Chemical Reference Data, 1995. **24**(3): p. 1377-1381.
103. Nemoto, T., S. Sasaki, and Y. Hakuraku, *Thermal conductivity of alumina and silicon carbide ceramics at low temperatures*. Cryogenics, 1985. **25**(9): p. 531-532.
104. Ju, Y. and K. Goodson, *Phonon scattering in silicon films with thickness of order 100 nm*. Applied Physics Letters, 1999. **74**(20): p. 3005-3007.
105. Hohensee, G.T., R. Wilson, and D.G. Cahill, *Thermal conductance of metal–diamond interfaces at high pressure*. Nature communications, 2015. **6**: p. 6578.
106. Lyeo, H.-K. and D.G. Cahill, *Thermal conductance of interfaces between highly dissimilar materials*. Physical Review B, 2006. **73**(14): p. 144301.
107. Cahill, D.G., et al., *Thermal conductivity of epitaxial layers of dilute SiGe alloys*. Physical Review B, 2005. **71**(23): p. 235202.
108. Khalatnikov, I., * *Teploobmen Mezhdru Tverdym Telom I Geliem-Ii*. Zhurnal Eksperimentalnoi I Teoreticheskoi Fiziki, 1952. **22**(6): p. 687-704.
109. Little, W., *The transport of heat between dissimilar solids at low temperatures*. Canadian Journal of Physics, 1959. **37**(3): p. 334-349.
110. Swartz, E. and R. Pohl, *Thermal resistance at interfaces*. Applied Physics Letters, 1987. **51**(26): p. 2200-2202.
111. Hopkins, P.E., J.C. Duda, and P.M. Norris, *Anharmonic phonon interactions at interfaces and contributions to thermal boundary conductance*. Journal of Heat Transfer, 2011. **133**(6): p. 062401.

112. Swartz, E.T. and R.O. Pohl, *Thermal boundary resistance*. Reviews of modern physics, 1989. **61**(3): p. 605.
113. Mingo, N. and L. Yang, *Phonon transport in nanowires coated with an amorphous material: An atomistic Green's function approach*. Physical Review B, 2003. **68**(24): p. 245406.
114. Zhang, W., T. Fisher, and N. Mingo, *The atomistic Green's function method: An efficient simulation approach for nanoscale phonon transport*. Numerical Heat Transfer, Part B: Fundamentals, 2007. **51**(4): p. 333-349.
115. Tian, Z., K. Esfarjani, and G. Chen, *Enhancing phonon transmission across a Si/Ge interface by atomic roughness: First-principles study with the Green's function method*. Physical Review B, 2012. **86**(23): p. 235304.
116. Baker, C.H., D.A. Jordan, and P.M. Norris, *Application of the wavelet transform to nanoscale thermal transport*. Physical Review B, 2012. **86**(10): p. 104306.
117. Schelling, P., S. Phillpot, and P. Keblinski, *Kapitza conductance and phonon scattering at grain boundaries by simulation*. Journal of Applied Physics, 2004. **95**(11): p. 6082-6091.
118. Schelling, P., S. Phillpot, and P. Keblinski, *Phonon wave-packet dynamics at semiconductor interfaces by molecular-dynamics simulation*. Applied Physics Letters, 2002. **80**(14): p. 2484-2486.
119. Roberts, N.A. and D. Walker, *Phonon wave-packet simulations of Ar/Kr interfaces for thermal rectification*. Journal of Applied Physics, 2010. **108**(12): p. 123515.
120. Young, D. and H. Maris, *Lattice-dynamical calculation of the Kapitza resistance between fcc lattices*. Physical review B, 1989. **40**(6): p. 3685.
121. Sun, H. and K.P. Pipe, *Perturbation analysis of acoustic wave scattering at rough solid-solid interfaces*. Journal of Applied Physics, 2012. **111**(2): p. 023510.
122. Kakodkar, R.R. and J.P. Feser, *Probing the validity of the diffuse mismatch model for phonons using atomistic simulations*. Physical Review B, 2017. **95**(12): p. 125434.
123. Kakodkar, R.R. and J.P. Feser, *A framework for solving atomistic phonon-structure scattering problems in the frequency domain using perfectly matched layer boundaries*. Journal of Applied Physics, 2015. **118**(9): p. 094301.
124. Peierls, R., *On the kinetic theory of thermal conduction in crystals*, in *Selected Scientific Papers Of Sir Rudolf Peierls: (With Commentary)*. 1997, World Scientific. p. 15-48.

125. Landauer, R., *Spatial variation of currents and fields due to localized scatterers in metallic conduction*. IBM Journal of Research and Development, 1957. **1**(3): p. 223-231.
126. Costescu, R.M., M.A. Wall, and D.G. Cahill, *Thermal conductance of epitaxial interfaces*. Physical Review B, 2003. **67**(5): p. 054302.
127. Hopkins, P.E., et al. *Effects of surface roughness and oxide layer on the thermal boundary conductance at aluminum/silicon interfaces*. in *2010 14th International Heat Transfer Conference*. 2010. American Society of Mechanical Engineers.
128. Hopkins, P.E., et al., *Effect of dislocation density on thermal boundary conductance across GaSb/GaAs interfaces*. Applied Physics Letters, 2011. **98**(16): p. 161913.
129. Beechem, T., et al., *Role of interface disorder on thermal boundary conductance using a virtual crystal approach*. Applied Physics Letters, 2007. **90**(5): p. 054104.
130. Hopkins, P.E. and T.E. Beechem, *Phonon scattering and velocity considerations in the minimum phonon thermal conductivity of layered solids above the plateau*. Nanoscale and Microscale Thermophysical Engineering, 2010. **14**(1): p. 51-61.
131. Hopkins, P.E. and P.M. Norris, *Effects of joint vibrational states on thermal boundary conductance*. Nanoscale and Microscale Thermophysical Engineering, 2007. **11**(3-4): p. 247-257.
132. Gordiz, K., *Modal decomposition of thermal conductance*. 2017, Georgia Institute of Technology.
133. Gordiz, K. and A. Henry, *Phonon transport at interfaces: Determining the correct modes of vibration*. Journal of Applied Physics, 2016. **119**(1): p. 015101.
134. Gordiz, K. and A. Henry, *Phonon transport at crystalline Si/Ge interfaces: the role of interfacial modes of vibration*. Scientific reports, 2016. **6**: p. 23139.
135. Seyf, H.R., et al., *Rethinking phonons: The issue of disorder*. npj Computational Materials, 2017. **3**(1): p. 49.
136. Lv, W. and A. Henry, *Examining the validity of the phonon gas model in amorphous materials*. Scientific reports, 2016. **6**: p. 37675.
137. Wei, L. and H. Asegun, *Non-negligible Contributions to Thermal Conductivity From Localized Modes in Amorphous Silicon Dioxide*. Scientific Reports, 2016. **6**: p. 35720.
138. Gordiz, K. and A. Henry, *A formalism for calculating the modal contributions to thermal interface conductance*. New Journal of Physics, 2015. **17**(10): p. 103002.

139. Siegel, D.J., L.G. Hector Jr, and J.B. Adams, *Adhesion, atomic structure, and bonding at the Al (111)/ α -Al₂O₃ (0001) interface: a first principles study*. Physical Review B, 2002. **65**(8): p. 085415.
140. Gale, J.D., *GULP: A computer program for the symmetry-adapted simulation of solids*. Journal of the Chemical Society, Faraday Transactions, 1997. **93**(4): p. 629-637.
141. Eastman, J., et al., *Anomalous increase in effective thermal conductivities of ethylene glycol-based nanofluids containing copper nanoparticles*. Applied physics letters, 2001. **78**(6): p. 718-720.
142. Lee, S., et al., *Measuring thermal conductivity of fluids containing oxide nanoparticles*. Journal of Heat Transfer, 1999. **121**(2): p. 280-289.
143. Wang, X., X. Xu, and S.U. S. Choi, *Thermal conductivity of nanoparticle-fluid mixture*. Journal of thermophysics and heat transfer, 1999. **13**(4): p. 474-480.
144. Wu, X., R. Kumar, and P. Sachdeva. *Calculation of thermal conductivity in nanofluids from atomic-scale simulations*. in *ASME 2005 International Mechanical Engineering Congress and Exposition*. 2005. American Society of Mechanical Engineers.
145. Sankar, N., N. Mathew, and C. Sobhan, *Molecular dynamics modeling of thermal conductivity enhancement in metal nanoparticle suspensions*. International Communications in Heat and Mass Transfer, 2008. **35**(7): p. 867-872.
146. Kang, H., Y. Zhang, and M. Yang, *Molecular dynamics simulation of thermal conductivity of Cu-Ar nanofluid using EAM potential for Cu-Cu interactions*. Applied Physics A, 2011. **103**(4): p. 1001-1008.
147. Mohebbi, A., *Prediction of specific heat and thermal conductivity of nanofluids by a combined equilibrium and non-equilibrium molecular dynamics simulation*. Journal of Molecular Liquids, 2012. **175**: p. 51-58.
148. Lin, Y.-S., P.-Y. Hsiao, and C.-C. Chieng, *Thermophysical characteristics of ethylene glycol-based copper nanofluids using nonequilibrium and equilibrium methods*. International Journal of Thermal Sciences, 2012. **62**: p. 56-60.
149. Loulijat, H., et al., *Effect of Morse potential as model of solid-solid inter-atomic interaction on the thermal conductivity of nanofluids*. Advanced Powder Technology, 2015. **26**(1): p. 180-187.
150. Chon, C.H., et al., *Empirical correlation finding the role of temperature and particle size for nanofluid (Al₂O₃) thermal conductivity enhancement*. Applied Physics Letters, 2005. **87**(15): p. 3107.

151. Li, C.H. and G. Peterson, *Experimental investigation of temperature and volume fraction variations on the effective thermal conductivity of nanoparticle suspensions (nanofluids)*. Journal of Applied Physics, 2006. **99**(8): p. 084314.
152. Muraleedharan, M.G., D.S. Sundaram, and V. Yang. *Heat Transport in Aqueous Suspensions of Alumina Nanoparticles*. in *54th AIAA Aerospace Sciences Meeting*. 2016.
153. Feng, Y., et al., *The effective thermal conductivity of nanofluids based on the nanolayer and the aggregation of nanoparticles*. Journal of Physics D: Applied Physics, 2007. **40**(10): p. 3164.
154. Xue, L., et al., *Two regimes of thermal resistance at a liquid–solid interface*. The Journal of chemical physics, 2003. **118**(1): p. 337-339.
155. Miyamoto, S. and P.A. Kollman, *SETTLE: an analytical version of the SHAKE and RATTLE algorithm for rigid water models*. Journal of computational chemistry, 1992. **13**(8): p. 952-962.
156. Cygan, R.T., J.-J. Liang, and A.G. Kalinichev, *Molecular models of hydroxide, oxyhydroxide, and clay phases and the development of a general force field*. The Journal of Physical Chemistry B, 2004. **108**(4): p. 1255-1266.
157. Hünenberger, P.H., *Thermostat algorithms for molecular dynamics simulations*, in *Advanced computer simulation*. 2005, Springer. p. 105-149.
158. Das, S.K., et al., *Nanofluids: science and technology*. 2007: John Wiley & Sons.
159. Xie, H., et al., *Thermal conductivity enhancement of suspensions containing nanosized alumina particles*. Journal of Applied Physics, 2002. **91**(7): p. 4568-4572.
160. Ross, S. and W. Winkler, *On physical adsorption: IX. Sub-critical and subpractical adsorption isotherms for krypton monolayers on graphitized carbon black*. Journal of Colloid Science, 1955. **10**(4): p. 330-337.
161. Shapovalov, V. and T.N. Truong, *Ab initio study of water adsorption on α -Al₂O₃ (0001) crystal surface*. The Journal of Physical Chemistry B, 2000. **104**(42): p. 9859-9863.
162. Argyris, D., et al., *Molecular dynamics studies of interfacial water at the alumina surface*. The Journal of Physical Chemistry C, 2011. **115**(5): p. 2038-2046.
163. Bernath, P.F., *The spectroscopy of water vapour: experiment, theory and applications*. Physical Chemistry Chemical Physics, 2002. **4**(9): p. 1501-1509.
164. Rayleigh, J.W.S.B., *The theory of sound*. Vol. 2. 1896: Macmillan.

165. Sundaram, D., V. Yang, and V. Zarko, *Combustion of nano aluminum particles (Review)*. Combustion, Explosion, and Shock Waves, 2014. **51**(2): p. 173-196.
166. Keller, H.B., *Numerical methods for two-point boundary-value problems*. 2018: Courier Dover Publications.
167. Sengers, J. and J.T.R. Watson, *Improved international formulations for the viscosity and thermal conductivity of water substance*. Journal of physical and chemical reference data, 1986. **15**(4): p. 1291-1314.
168. Lemmon, E., M. Huber, and M. McLinden, *REFPROP: Reference fluid thermodynamic and transport properties*. NIST standard reference database, 2007. **23**(8.0).
169. Kodama, T., et al., *Modulation of thermal and thermoelectric transport in individual carbon nanotubes by fullerene encapsulation*. Nature materials, 2017. **16**(9): p. 892.
170. Feng, L., et al., *Phonon-interference resonance effects by nanoparticles embedded in a matrix*. Physical Review B, 2017. **96**(22): p. 220301.
171. Ju, S., et al., *Designing nanostructures for phonon transport via Bayesian optimization*. Physical Review X, 2017. **7**(2): p. 021024.